UNIVERSITY OF CALIFORNIA,
IRVINE

Ion Flow Measurements and Plasma Current Analysis in the Irvine Field Reversed Configuration

DISSERTATION

submitted in partial satisfaction of the requirements
for the degree of

DOCTOR OF PHILOSOPHY

in Physics

by

Wayne Sutton Harris III

Dissertation Committee:
Professor William Heidbrink, Chair
Professor Norman Rostoker
Professor Roger McWilliams
Doctor Eusebio Garate

2009

The dissertation of Wayne Sutton Harris III
is approved and is acceptable in quality and form for
publication on microfilm and in digital formats:

Committee Chair

University of California, Irvine
2009

DEDICATION

To Amber, Sutton, and Wyatt- your unconditional love and support throughout these years has immeasurably helped me get through this.

TABLE OF CONTENTS

LIST OF FIGURES

LIST OF TABLES

LIST OF SYMBOLS

A_i	Einstein transition probability
a_0	Bohr radius
B_r	Radial magnetic field
B_θ	Toroidal magnetic field
B_z	Axial magnetic field
c	Speed of light
c_s	Ion sound speed
t_o	Time-of-flight diagnostic slot width
e_i	Charge of electron
e_i	Charge of ion
E_r	Radial electric field
E_θ	Toroidal electric field
f	Time-of-flight diagnostic rotation frequency
f_e	Electron distribution function
f_i	Ion distribution function
G	Etendue
$\hbar$	Planck's constant
H_α	Hydrogen's Balmer alpha transition
H_β	Hydrogen's Balmer beta transition
I	Current (plasma or coil)
I_{sat}	Ion saturation current
J_e	Electron current density
J_i	Ion current density
k	Boltzmann's constant
m_e	Electron mass
m_i	Ion mass
n_0	Peak density
n_e	Electron Density
n_i	Ion density
$n_{1,2}$	Parabolic quantum numbers
q	Electronic charge
R	Time-of-flight diagnostic chopper wheel radius
r_{lim}	Limiter coil radius
r_{flux}	Flux coil radius
T_e	Electron temperature
T_i	Ion temperature
t_{LF}	Time delay between Limiter and Flux Coil
t_o	Time-of-flight diagnostic "open" time
t_s	Time-of-flight diagnostic sampling period
v	Particle velocity
Z	Ion charge state

ϵ_0	permittivity of free space
ε	Emissivity
$\mathcal{E}$	Induced EMF
η	Detection efficiency
λ	Wavelength
λ_0	Wavelength at zero Doppler shift
$\Delta\lambda$	Wavelength spread
μ_0	Permeability of free space
σ	Cross-section (charge-exchange, ionization, or excitation)
Φ	Magnetic flux
ω_e	Electron rotation frequency
ω_i	Ion rotation frequency

ACKNOWLEDGMENTS

First and foremost, I would like to thank my advisor Bill Heidbrink. I have always felt welcome to come to his office for assistance, and am continually impressed by his breadth of knowledge in plasma physics. He has provided me with guidance to keep me on track, and freedom to pursue ideas relevant to my research.

Eusebio Garate also played a very influential role in my growth as an experimentalist. I've learned a lot from him about the importance of testing individual components of a new system, as well as varying relevant parameters on the IFRC device in order to see their effects on new diagnostics. In addition, his overall breadth of knowledge about plasma diagnostics has been an invaluable resource and never ceases to amaze me.

Roger McWilliams has been very good at making sure my ideas are communicated to others properly. While I generally know what it is I am trying to say, there have been many instances where he points out one or more assumptions I've made but have not communicated properly. I have learned a great deal from him about writing with the exactness necessary to communicate ideas effectively. In addition, his interest, concern, and guidance regarding my future career as a physicist has been greatly appreciated.

I would also like to thank my fellow graduate students Erik Trask and Thomas Roche, also working on IFRC. Erik's involvement with virtually every aspect of the IFRC device has proved to be extremely beneficial. Through his excitement in learning new things he has been eager to take on any task presented to the group. Although Tommy came to the group years after Erik and I, he has been a valuable asset to the team. He is extremely well versed in computers, and in a short time took the IDL software I started for data analysis and improved it in ways that I may never understand.

Other graduate students have that have helped contribute to my work are Yang Zhang, Yadong Luo, and Deyong Liu. I have had many talks between each of them covering areas from plasma physics to optics to computational support. In particular, Yang helped a great deal using his ion source for calibrating the time-of-flight diagnostic. Yadong's input from what he learned in his spectroscopic diagnostic was also very helpful.

Our data acquisition system was made possible by the work contributed by Alan Van Drie. I am very grateful for his efforts in writing the LAB2000 software. Even when our hard drive crashed and we lost all of the IFRC data (as well as the LAB200 software), he re-wrote what was necessary to get it running again. For this I am very thankful.

In addition, we have had a few undergraduate researchers who did some work on various plasma diagnostics. In 2004, Jason's work on the triple probe furthered my understanding of these types of probes. Tyson Cook worked on an optical diagnostic in 2005. The electron temperature measurements made with my spectrometer rely on the same principle as the one from his diagnostic. In 2006, Justin Little did a great deal of work on the spectrometer system. Although most of what he did has been modified, his work helped us understand what modifications needed to be made.

CURRICULUM VITAE

Wayne Sutton Harris III

EDUCATION

Doctor of Philosophy in Plasma Physics **2009**
University of California, Irvine *Irvine, California*

Master of Science in Physics **2005**
University of California, Irvine *Irvine, California*

Bachelor of Science in Physics **2003**
University of Texas, Austin *Austin, Texas*

SELECTED HONORS AND AWARDS

Graduate Assistance in Areas of National Need Fellowship **2007**

PUBLICATIONS

- W.S. Harris, E. Trask, T. Roche, E.P. Garate, W.W. Heidbrink, R. McWilliams. "Ion Flow Measurements and Plasma Current Analysis in the Irvine Field Reversed Configuration." Submitted to Physics of Plasmas (2009).
- W.S. Harris, E.P. Garate, W.W. Heidbrink, R. McWilliams, T. Roche, E. Trask, Y. Zhang. "Time-of-Flight Neutral Particle Analyzer and Calibration", Review of Scientific Instruments **79**, 10F313 (2008).

PRESENTATIONS

- "Ion Current Estimations in the Irvine FRC." W.S. Harris, E. Trask, T. Roche, E.P. Garate, W.W. Heidbrink, R. McWilliams. University of California - Irvine. January 20, 2009.

- “Ion Current Estimations in the Irvine FRC.” W.S. Harris, E. Trask, T. Roche, E.P. Garate, W.W. Heidbrink, R. McWilliams. University of Wisconsin - Madison. February 5, 2009.

POSTERS

- W.S. Harris, E.P. Garate, W.W. Heidbrink, R. McWilliams, T. Roche, E. Trask. “Ion Energy Distribution Functions in the Irvine FRC”, poster presented at the 2008 American Physical Society Division of Plasma Physics Meeting, Dallas, TX.
- W.S. Harris, E.P. Garate, W.W. Heidbrink, R. McWilliams, T. Roche, E. Trask, Y. Zhang. “ Time-of-Flight Neutral Particle Analyzer and Calibration”, poster presented at the 2008 High Temperature Plasma Diagnostics Conference, Albuquerque, NM.
- W.S. Harris, E.P. Garate, W.W. Heidbrink, R. McWilliams, T. Roche, E. Trask, Y. Zhang. “Ion Energy Distribution Function Measurements in the Irvine FRC”, poster presented at the 2007 American Physical Society Division of Plasma Physics Meeting, Orlando, FL.
- W.S. Harris, E.P. Garate, W.W. Heidbrink, E. Trask. “A Time-of-Flight Neutral Particle Detector for the Irvine FRC”, poster presented at the 2006 American Physical Society Division of Plasma Physics Meeting, Philadelphia, PA.
- W.S. Harris, E.P. Garate, W.W. Heidbrink, E. Trask, A. Van Drie. “Current Diagnostics in an FRC with a Toroidal Electric Field”,poster presented at the 2005 American Physical Society Division of Plasma Physics Meeting, Denver, CO.

ABSTRACT OF THE DISSERTATION

Ion Flow Measurements and Plasma Current Analysis
in the Irvine Field Reversed Configuration

By

Wayne Sutton Harris III

Doctor of Philosophy in Physics

University of California, Irvine, 2009

Professor William Heidbrink, Chair

The contribution of ions current in the lab frame to the total plasma current is studied in the Irvine Field Reversed Configuration (IFRC). Two diagnostics have been developed to measure the ion velocity distribution function. A charge-exchange neutral particle analyzer uses a 13 cm radius slotted disk rotating at 165 Hz in vacuum to chop the emitted neutrals at a rate of 13 kHz. The chopped neutrals are detected using a channel electron multiplier and the particle velocity is measured using time of flight, with an average energy uncertainty, $\Delta E/E$, of 0.11. A modified monochromator is used to measure Doppler shifts and broadening of several spectral lines emitted from the plasma with a wavelength resolution of 0.42 Å and instrumental broadening of 0.3 Å. Measurements of the Doppler shift of impurity lines indicate that there is a flow in the range of 5-7km/s in IFRC. The charge-exchange neutral particle analyzer shows the peak energy is below the 20eV minimum detectable energy threshold, which is in agreement with the spectroscopic data. By evaluating the collision times between the impurities and hydrogen, the dominant plasma ion species, it is concluded that the ions rotate with an angular frequency of $\sim 4 \times 10^4$ rad/s. Estimates of the ion current in the lab frame are accomplished by determining the ion density distribution

using two methods. One method is a solution of the pressure balance relation, and the other fits the measured magnetic probe data to a theoretical equilibrium. The results from these estimates indicate that the ion current is 1-2 orders of magnitude larger than the measured plasma current of 15kA. Calculations of electron drifts from the equilibrium fields show that the electrons cancel most of the ion current.

Chapter 1

Introduction

In 1946 the first patent for a fusion reactor was filed in the United Kingdom by Sir George Paget Thomson and Moses Blackman[1]. The goal for that idea, like most other concepts today, was to confine a plasma using magnetic fields and heat it with radio frequency electromagnetic waves in an attempt to produce energy in the form of thermonuclear fusion. Magnetic fields are necessary to protect the vacuum vessel from the high temperatures reached in fusion devices. Today's experiments have come a long way with diagnostics measuring plasma temperature, density, magnetic fields, and many other measurable quantities. Although the goal is still to produce fusion, plasma physicists have come to realize the difficulties associated with plasma confinement (instabilities, particle and energy transport, etc.) and the primary focus is to understand and control them to reach that goal.

The confinement of plasmas with magnetic fields on the most basic level can be understood by considering single particle trajectories. A charged particle will gyrate in the presence of a uniform magnetic field, and if it has a velocity component in the direction of this field, it will follow the field lines. If the field lines are closed, meaning they terminate on themselves forming a closed loop, then the particles will follow these closed loops until acted upon by another force. Plasma confinement, however, is not as simple as creating closed field lines. Guiding center drifts such as the $E \times B$ and ∇B drifts cause particles to move perpendicular to the confining field lines. Coulomb collisions cause particles to scatter into different orbits, possibly from confinement to an unconfined orbit. When interpreting the plasma as a fluid, its density and temperature create a pressure that must be in balance with the confining magnetic field. There are many things other than this to consider when designing a magnetic confinement scheme, all of which are very important.

Present magnetic confinement concepts are distinguished by their magnetic field profiles. Such concepts include, but are not limited to, the tokamak, stellarator, reversed field pinch (RFP), spheromak, and field reversed configuration (FRC). While the tokamak, stellarator, RFP, and spheromak are all characterized by having a large magnetic field in the core where the plasma density is highest, the core of the FRC has no magnetic field. This experiment has been performed on an FRC called the Irvine Field Reversed Configuration (IFRC), so further discussion will focus on FRCs.

The FRC has been around since the late 1950's in theta pinch experiments with a reversed background magnetic field[2]. Some of the notable features of the FRC which make it attractive as a magnetic confinement device include[3]:

1. A simplified geometry compared to others, which typically require a toroidal shaped vacuum vessel.

2. High plasma beta, meaning higher plasma densities and temperatures for less magnetic fields (which translates into lower cost).

3. The ability to translate down the gradient of a magnetic field, allowing for compression heating.

4. Exhaust plasma occurs at the ends of the system, allowing for direct energy conversion.

As discussed in Chapter 2, the understanding of FRCs has come a long way over the past few decades.

The IFRC experiment has come a long way in the past five years. During its initial stages, the vacuum system had its fair share of leaks and the high voltage trigger system was not operational.

This thesis is organized into eight chapters. Chapter 1 is a brief introduction to magnetic confinement of plasmas. A detailed description of FRCs is provided in Chapter 2 along with a motivation for the research done by the experimenter. Chapter 3 covers a detailed description of IFRC. A charge-exchange neutral particle analyzer is described in Chapter 4 and a spectrometer used for the study of emission lines is in Chapter 5. Data from IFRC are shown in Chapter 6. An analysis of the ion flow along with the expected electron contribution is presented in Chapter 7. Conclusions and future work are discussed in Chapter 8.

Chapter 2

Field Reversed Configurations

The FRC is a self-organized plasma, meaning the confining fields are generated by the plasma current (although in laboratory experiments, magnetic fields are required to form an FRC). While the net current density is what determines the magnetic field structure through the Biot-Savart Law, the individual electron and ion components of the current density are of great interest. Stability of the FRC is thought to be attributed to a plasma current that is dominated by large orbit ions[4]. It has also been demonstrated through theoretical analysis that penetration of the electrostatic potential for current drive is most effective when the plasma current is dominated by ions rather than electrons[5]. These findings provide the motivation behind assessing whether the current is primarily composed of ions or not.

This chapter covers a broad range of topics that are fundamental to understanding the plasma current in an FRC. Section 2.1 contains basic FRC information including: structure, an equilibrium model, particle orbits, instabilities, and formation methods. The acceleration of ions in an FRC is discussed in Sec. 2.2. Section 2.3 covers some of the diagnostics used in plasma physics experiments for measuring ion flow. Past

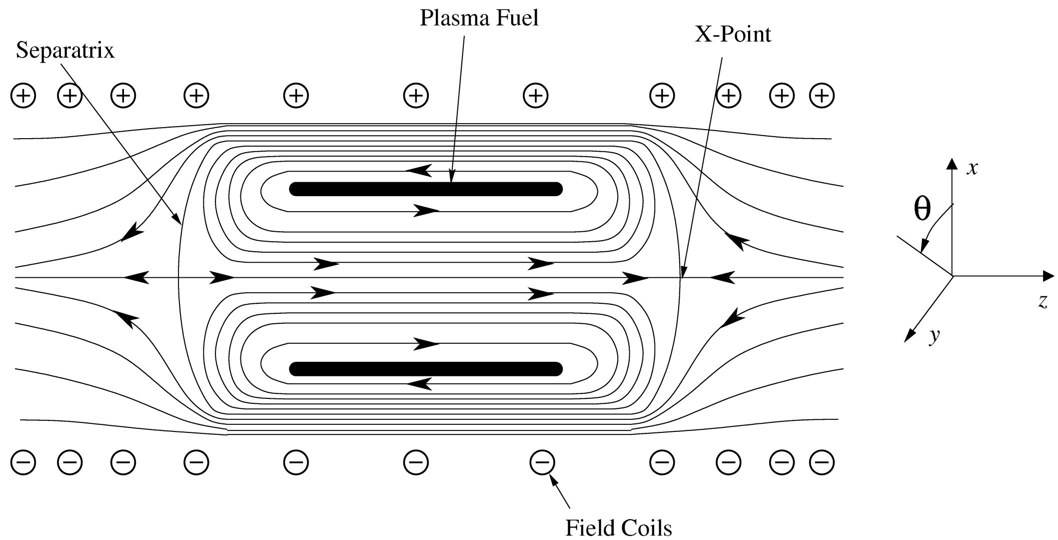

Figure 2.1: Magnetic field structure of an FRC[6]

measurements of ion flow are discussed in Sec. 2.4. Section 2.5 contains a summary of the considerations relevant to the work presented in this thesis.

2.1 FRC Fundamentals

2.1.1 Equilibrium

The FRC has a magnetic field structure shown in the Fig. 2.1. The plasma current ring, whose cross section is shown as the thick black line, is centered around the location where the magnetic field along the z-axis is zero (called the null surface). As mentioned in Chapter 1, the null surface is a unique feature of FRCs, and its presence accommodates the large ion orbits mentioned in Sec. 2.1.2. A region of closed field lines surrounds the current ring such that each surface of constant magnetic flux has a toroidal shape. The closed field lines are surrounded by open field lines generated by an external coil, and the boundary between the two regions is called the separatrix.

Analytical expressions for the equilibrium fields are obtained by solving the Vlasov-Maxwell equations:

$$(\vec{v} \cdot \nabla) f_j + \frac{e_j}{m_j} \vec{E} \cdot \nabla_v f_j + \frac{e_j}{m_j} [\vec{v} \times \vec{B}] \cdot \nabla_v f_j = 0 \tag{2.1}$$

$$\nabla \times \mathbf{E} = 0 \tag{2.2}$$

$$\nabla \times \mathbf{B} = \mu_0 \sum_j e_j \int \vec{v} f_j d\vec{v} \tag{2.3}$$

$$\sum_j n_j e_j \simeq 0. \tag{2.4}$$

where the following assumptions have been made:

- The time derivatives are zero
- Azimuthal symmetry ($d/d\theta = 0$)
- Uniformity along the axis ($d/dz = 0$)
- The plasma is quasi-neutral (Eq. 2.4)

It has been shown that the rigid-rotor distribution function provides a self-consistent solution to these equations[7]. The rigid rotor equilibrium is given by

$$f_j(r, \vec{v}) = \left(\frac{m_j}{2\pi T_j} \right)^{3/2} n_j(r) \exp \left\{ -\frac{m_j}{2T_j} |\vec{v} - \vec{\omega_j} \times \vec{r}|^2 \right\} \tag{2.5}$$

where the subscript j is for the electron (or ion) species, m is the mass, T is the temperature, n is the density, and ω is the rotation velocity. The physical interpretation of this distribution function is that for a given density distribution $n(r, z)$, the particles rotate uniformly with an angular velocity ω.

A one-dimensional solution of the Vlasov-Maxwell equations gives[7]

$$B_z(r) = -B_0 \left[1 + \sqrt{\beta} \tanh \left(\frac{r^2 - r_0^2}{r_0 \Delta r} \right) \right] \tag{2.6}$$

$$E_r(r) = -r\omega_e B_z(r) - \frac{T_e}{e} \frac{d \ln n_e(r)}{dr} + \frac{m}{e} r\omega_e^2 \tag{2.7}$$

$$n_i(r) = \frac{n_{i0}}{\cosh^2 \left(\frac{r^2 - r_0^2}{r_0 \Delta r} \right)} \tag{2.8}$$

where

$$\beta \equiv \frac{2\mu_0 \sum_j n_{0j} T_j}{B_0^2}, \tag{2.9}$$

ω_e is the electron rotation frequency, r_0 is the location of the peak density, Δr is the characteristic radial thickness, n_{i0} is the peak density, and B_0 is the external magnetic field. In this model, the electric field only has an $\hat{r}$ component while the magnetic field only has a $\hat{z}$ component and they both vary only along the r-axis. Although the electric field points away from the null surface, this radial acceleration is balanced by the $q\vec{v} \times \vec{B}$ term of the Lorentz force. The density profile is a function of r, and rotation is about the z-axis. The axial extent of the plasma is assumed to be long enough that the ends can be ignored. The equilibrium for a typical shot in IFRC is shown in Fig. 2.2. Details of the calculation appear in Chapter 6.

2.1.2 Particle Orbits

The orbits that arise from Eqs. 2.6-2.7 are calculated by solving the Lorentz force equation

$$\vec{F} = m\vec{a} = q(\vec{E} + \vec{v} \times \vec{B}). \tag{2.10}$$

The two types of orbits that arise are drift and betatron orbits. Distinguishing characteristics of the betatron orbit are that it crosses the null surface and the toroidal

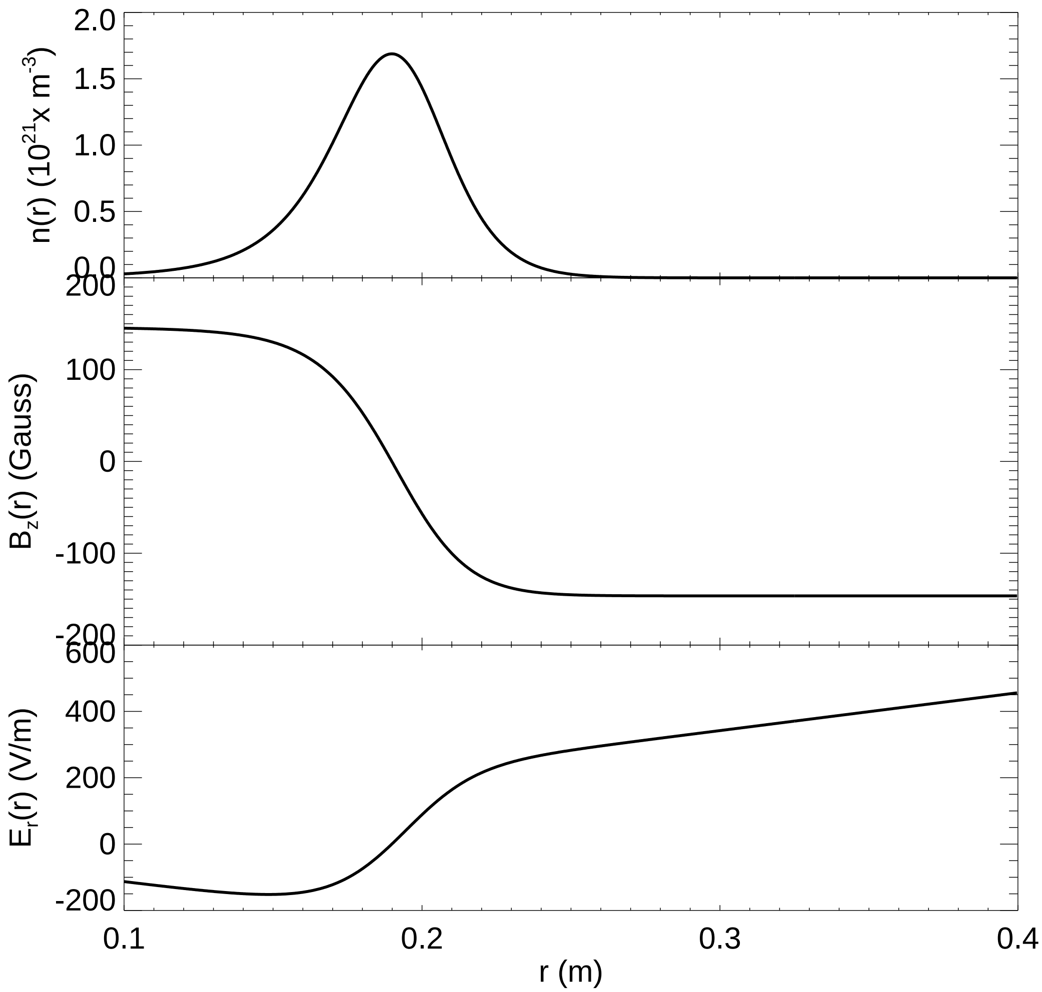

Figure 2.2: Typical field structure calculated from the equilibrium model.

component of the velocity vector does not change sign throughout the orbit. Drift orbits, on the other hand, do not cross the null surface (aside from a small sub-class of orbits called figure-eight orbits) and their toroidal velocity vector does change sign during the orbit. These two orbits are shown for ions in Fig. 2.3 for typical fields expected in IFRC. The inner and outer circles are the coil boundaries, and

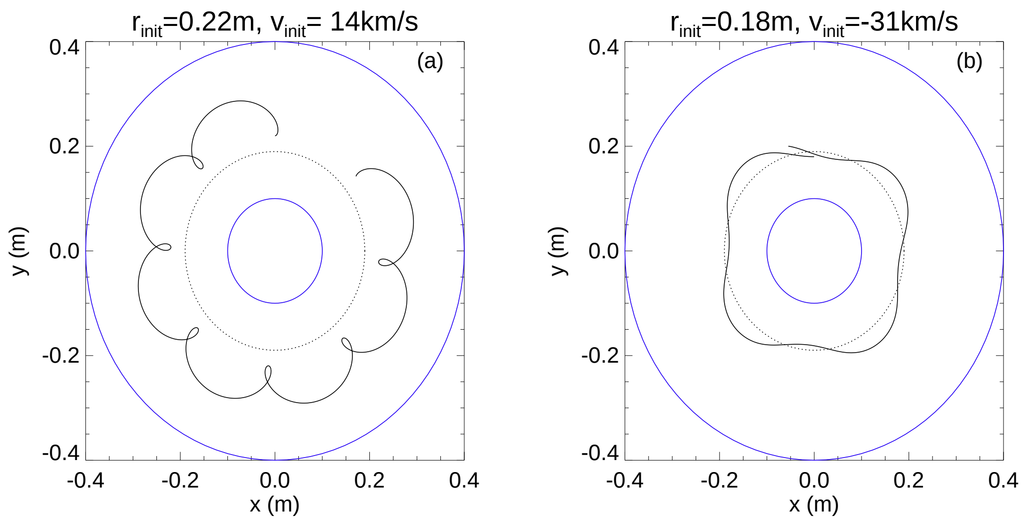

Figure 2.3: Two classes of orbits: (a) drift and (b) betatron orbits.

the dashed line is where the null surface is located. For these particular fields and initial conditions, ions in both betatron and drift orbits travel in the same direction (counter-clockwise).

An interesting consequence of the fields in Eqs. 2.6-2.7 is that the $E \times B$ and the ∇B guiding center drifts:

$$\mathbf{v}_{E\times B} = \frac{\mathbf{E}\times\mathbf{B}}{B^2} \tag{2.11}$$

and

$$\mathbf{v}_{\nabla B} = \frac{mv_\perp^2}{2}\frac{\mathbf{B}\times\nabla B}{B^3} \tag{2.12}$$

point in opposite directions for positive ions. The direction of the total drift is governed by the stronger of the two drifts. Figure 2.4 shows both possible orbits. In

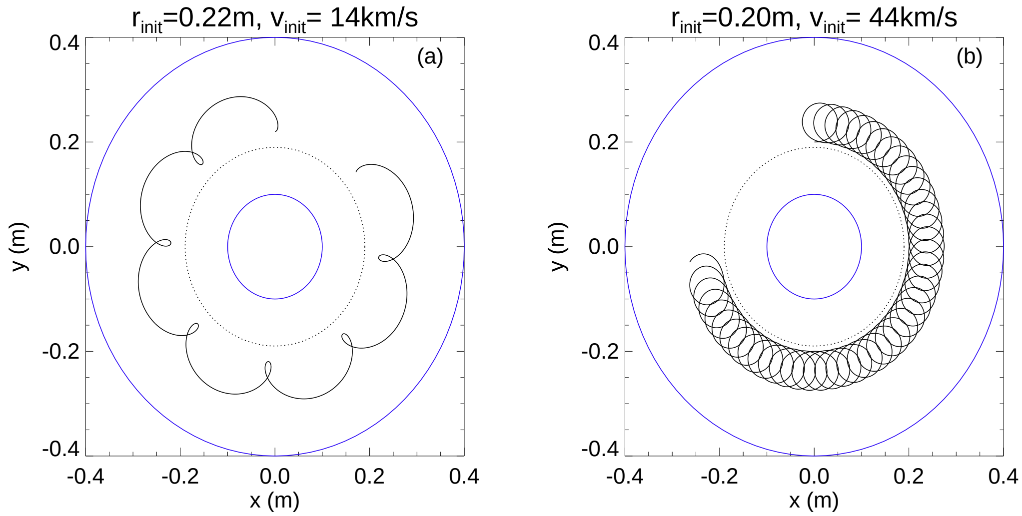

Figure 2.4: Drift orbits arising from (a) $E \times B$ and (b) ∇B drifts.

Fig. 2.4a, the equilibrium fields from Fig. 2.2 are used for calculating the orbit, which is dominated by the $E \times B$ drift. The electric field is reduced by a factor of 10 in order to obtain the ∇B drifts in Fig. 2.4b. For electrons, the ∇B drift is in the opposite direction of the ions while the $E \times B$ drift is in the same direction.

The various orbits either contribute to or subtract from the total plasma current. Electron drift orbits are all in the direction of the plasma current, so they effectively reduce the total current. For ions whose drifts are dominated by the ∇B drift, they also subtract from the total current, while those that are dominated by $E \times B$ drifts add to the current. Ion betatron orbits are in the direction of positive current, and electron betatron orbits are in the opposite direction. From this, it is clear that the relative populations of these orbits plays an important role in the total current.

2.1.3 FRC Instabilities

There are several instabilities that have been observed in FRCs[8]. The two that have been studied the most are the tilt mode[9] and the $n = 2$ rotational instability[3]. The tilt mode is essentially the tilting of the FRC at an angle relative to the axis, and is recognized by axial gradients in the axial magnetic field. For some theta pinch FRC devices, there is experimental evidence that the tilt mode affects the confinement time more than the other instabilities[8]. The same research shows that elongating the FRC and injecting a fast ion component have stabilizing influences.

The $n = 2$ rotational instability can be understood by imagining the circular shape of an $r - \theta$ slice of the FRC compressed to form an ellipse, which rotates with the plasma. The instability has been observed in many experiments throughout the years, and can be seen by looking axially with a camera[10] or it can present itself as oscillations in line integrated density[11]. It is also observed using emission spectroscopy, as described later in the chapter. Suppression of the instability has been very successful using multipole magnetic fields[11].

2.1.4 FRC Formation Methods

There are several FRC formation methods used in present experiments. The first FRCs used a method that is still used today, which is to set up a plasma in a background magnetic field and then quickly reverse the current in the magnetic field coil[2]. This formation technique, called a field reversed theta pinch (FRTP), is formed in a device similar to Fig. 2.5. It is reported that in FRTPs the plasma current is dominated by electrons, except when the initial field is zero[3].

Another approach to FRC formation is the use of a rotating magnetic field (RMF)[13]. This technique, shown in Fig.2.6, employs several coils that create a RMF strong enough to drag along magnetized electrons. In doing so, the current (composed of electrons) reverses the background magnetic field and the FRC is formed.

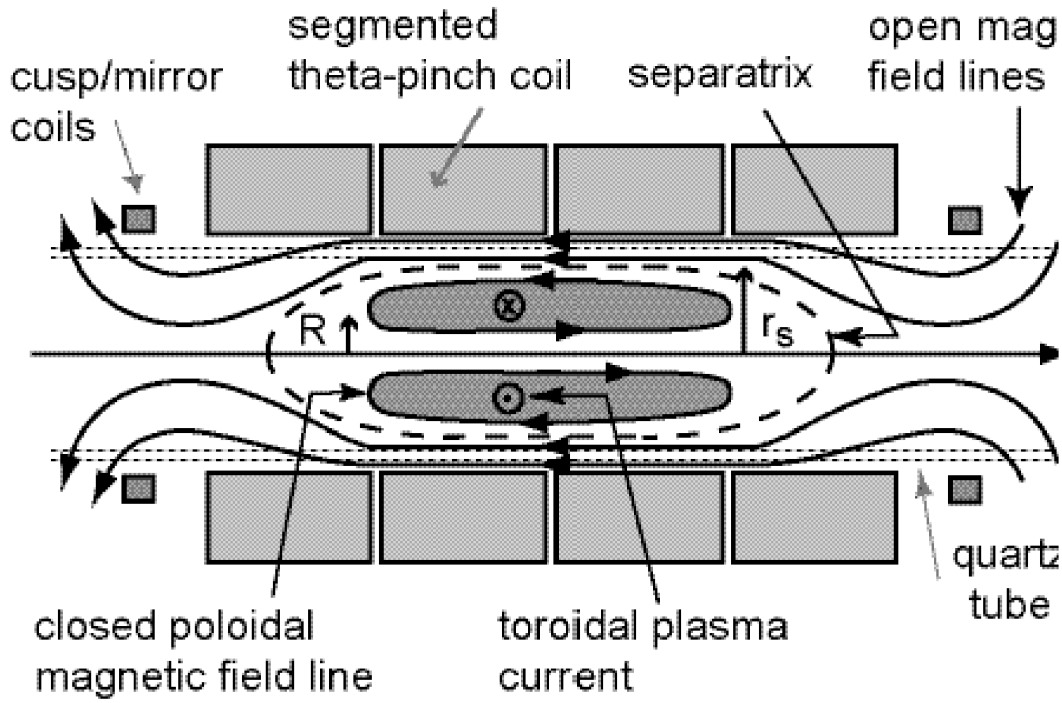

Figure 2.5: FRC produced by theta pinch[12]

The merging of two spheromaks with counter-helicity is a relatively new idea, being around for only a little more than a decade. The helicity of a spheromak refers to the direction of the toroidal magnetic field. The first experiments conducted using this method were on the Tokyo University Spherical Torus No. 3 (TS-3) device[15]. By merging spheromaks with oppositely directed toroidal magnetic fields, the net toroidal field cancels to zero and the resulting configuration is an FRC, as demonstrated in Fig. 2.7.

The formation of an FRC by means of an inductive center solenoid (also called a flux coil), has been around for over two decades now. This method uses the EMF from the flux coil to drive the plasma current, as in Fig. 2.8, and is the formation scheme used in IFRC. In past experiments [17], the initial background fields were created so that a null surface was present before injecting the plasma. This was accomplished

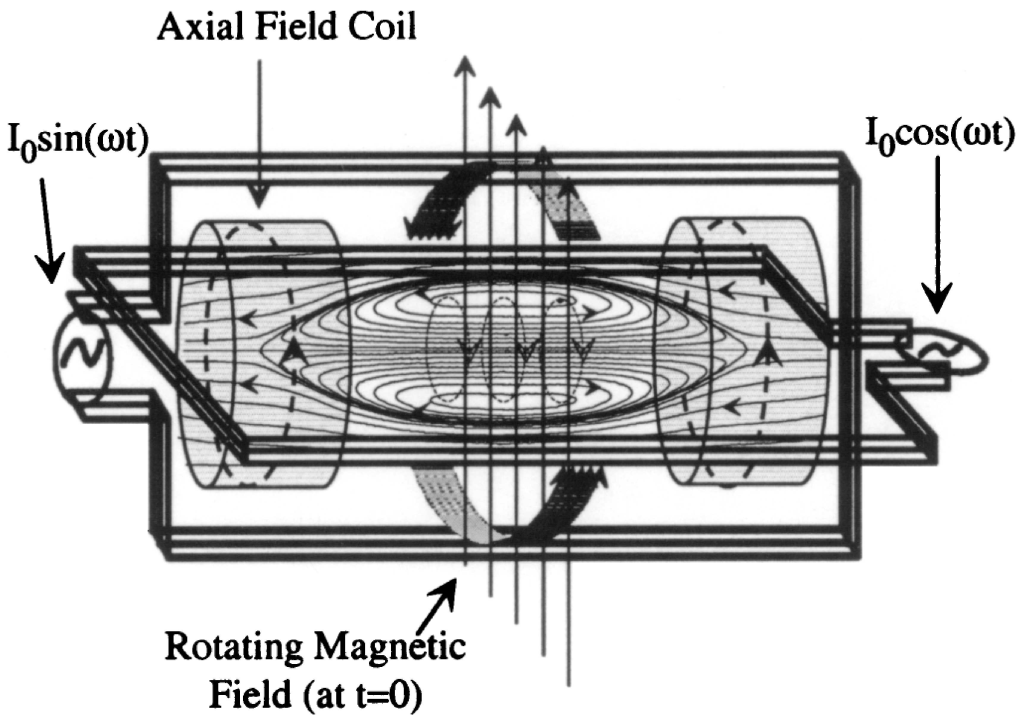

Figure 2.6: FRC produced by a rotating magnetic field[14]

by requiring the magnetic field from the outer coil to be comparable to the return flux from the inner coil. In IFRC, the goal is to accelerate ions (described in Sec. 2.2) and is made possible by having an initial magnetic field that does not have a null surface. As presented in this thesis, the plasma current has a substantial ion flow with electrons cancelling most of their contribution to the current. This is different from the other formation schemes where electrons dominate the plasma current. The mechanism by which ion acceleration is accomplished is discussed in the following section.

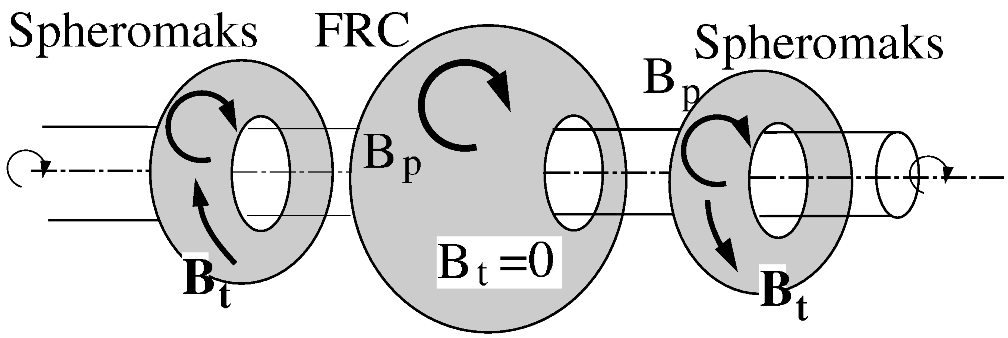

Figure 2.7: FRC produced by the merging of spheromaks[16]

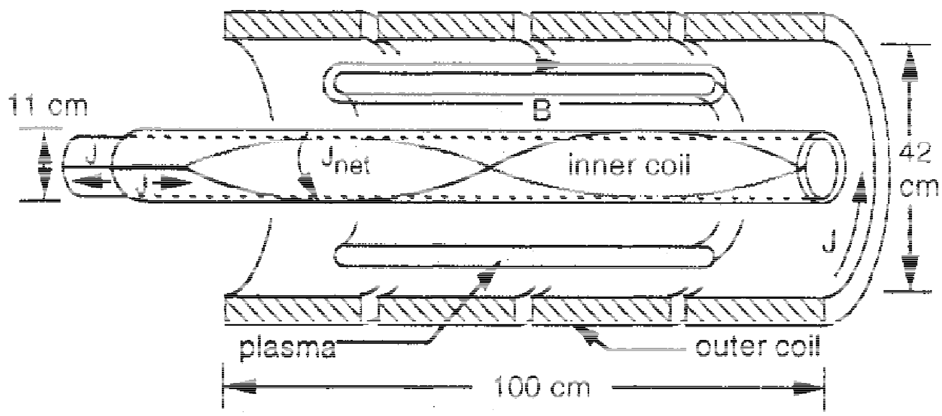

Figure 2.8: FRC produced by an inductive solenoid[17]

2.2 Ion Acceleration in an FRC

Ion acceleration during the formation of a flux coil induced FRC is discussed in this section. The main requirements for accelerating ions (rather than electrons) during FRC formation are:

- The electron gyroradius is small compared to the system size.
- The ion gyroradius is comparable to the system size.

These requirements ensure that[18]

- The magnetized electrons are tied to the magnetic field lines.
- The unmagnetized ions can readily cross the magnetic field lines.

To understand how these requirements are satisfied, the process by which the magnetic fields are created must be considered.

As explained in Chapter 3, the magnetic fields in IFRC (a flux coil induced FRC) are created by a pulsed $L-C$ circuit. The current through a magnetic field coil during FRC formation is

$$I(t) = I_{max}\sin(\omega t) \tag{2.13}$$

where I_{max} is the peak current and ω is the angular frequency. A coil with n turns per unit length with this current will produce an axial magnetic field

$$B_z(t) = \mu_0 n I(t) = \mu_0 n I_{max}\sin(\omega t). \tag{2.14}$$

As described in the previous section, a flux coil induced FRC requires at least two coils- a background magnetic field coil and a flux coil, each of which can be described by Eq. 2.14. For the flux coil, an additional variable is required to accommodate a delay t_{LF} between when the two coils fire

$$B_{z-flux}(t) = \begin{cases} 0 & t \leq t_{LF}, \\ \mu_0 n I_{max}\sin(\omega t) & t > t_{LF}. \end{cases} \tag{2.15}$$

The formation phase for this type of FRC essentially begins when the flux coil fires and the plasma current starts to ramp up.

For a given coil geometry, the ion gyroradius is ensured to be sufficiently large by satisfying one or more of the following:

- I_{max} for the background field coil is small so that B_z is small.
- t_{LF} is small relative to the rise time of the background field coil $\pi/2\omega$.

This means that the free parameters are the background coil charging voltage (which controls I_{max}), and the delay between the two coils. Using parameters similar to those in IFRC (plasma temperature ∼10 eV, background field ∼50 Gauss) results in a ion gyroradius of 9 cm and an electron gyroradius of 2 mm.The radius of the null surface is in the range of 10-20 cm, so these parameters should accommodate ion acceleration.

When the flux coil fires, a toroidal electric field is generated through induction. The EMF induced in the plasma is

$$\mathcal{E} = -\frac{\partial \Phi}{\partial t} = -A\frac{\partial B_z}{\partial t} = -\pi r_{flux}^2 \mu_0 n I_{max} \omega \cos(\omega t) \tag{2.16}$$

where r_{flux} is the flux coil radius. Integrating Faraday's Law

$$\nabla \times \mathbf{E} = -\frac{\partial \mathbf{B}}{\partial t} \tag{2.17}$$

over the open surface S, defined by the contour C, which is a circle at radius r

$$\int_S d\mathbf{S} \cdot \nabla \times \mathbf{E} = -\int_S d\mathbf{S} \cdot \frac{\partial \mathbf{B}}{\partial t} \tag{2.18}$$

where

$$\int_S d\mathbf{S} \cdot \nabla \times \mathbf{E} = \oint_C d\mathbf{l} \cdot \mathbf{E} = 2\pi r E_\theta \tag{2.19}$$

from Stoke's Theorem and axial symmetry of $\mathbf{E}$. Also, since S is time-independent

$$-\int_S d\mathbf{S}\cdot\frac{\partial\mathbf{B}}{\partial t} = -\frac{\partial}{\partial t}\int_S d\mathbf{S}\cdot\mathbf{B} = -\frac{\partial\Phi}{\partial t} \tag{2.20}$$

giving

$$-\frac{\partial\Phi}{\partial t} = 2\pi r E_\theta. \tag{2.21}$$

Combining this with the EMF, gives

$$E_\theta(r,t) = -\frac{r_{flux}^2\mu_0 n\omega I_{max}}{2r}\cos(\omega t). \tag{2.22}$$

The unmagnetized ions are accelerated by the electric field in the toroidal direction, resulting in an acceleration

$$a_\theta(t) = \frac{q}{m_i}E_\theta(t) = -\frac{r_{flux}^2\mu_0 n\omega q I_{max}}{2rm_i}\cos(\omega t). \tag{2.23}$$

Integrating the acceleration over the field reversal time T_r, the estimated ion velocity is

$$v_\theta = v_{0\theta} + \int_0^{T_r} a_\theta(t)dt = v_{0\theta} - \frac{r_{flux}^2\mu_0 n q I_{max}}{2rm_i}\sin(\omega T_r) \tag{2.24}$$

For $r_{flux} = 10.5$ cm, $r = 25$ cm, $T_r = 10$ μs, $I_{max} = 11$ kA, $n = 22$ turns/m, and $\omega = 1.4\times10^4$ rad/s, $v_\theta = 9.0\times10^4$ m/s, or 35 eV. This estimate provides an upper bound of the ion energy for ions accelerated by the flux coil; however, collisional drag between ions and electrons/neutrals has been ignored.

Since the electrons are magnetized, their motion is expressed in terms of guiding center drifts. In the presence of a uniform magnetic field and electric field, the associated drift is the $E\times B$ drift from Eq. 2.11. These drifts (relating to the electron flow) are discussed in more detail in Chapter 7. It should be noted that although the magnetic field is time-dependent, the electron gyrofrequency (40-300 MHz) is much larger than the characteristic frequency of the coils (2.3 kHz). Accordingly, the electrons only see an adiabatically changing field, and their dynamics are such that the perpendicular particle energy increases with the magnetic field in order to conserve the magnetic moment[18].

2.3 Ion Flow Diagnostics

There are several techniques for performing flow measurements in plasmas. Invasive diagnostics include Mach probes (described below), gridded energy analyzers[19], and optical probes[20]. Although invasive probes can generally achieve higher spatial resolution, their perturbative nature is not desirable. Non-invasive diagnostics avoid perturbations of the plasma, however they typically achieve lower spatial resolution. Methods of measuring ion flow non-invasively include charge-exchange neutral particle analyzers (described below) and visible emission spectroscopy (described below).

2.3.1 Mach Probes

Mach probes require a fairly simple construction and they work by measuring the ion saturation current upstream and downstream of the plasma flow[21]. The physical interpretation of the data is well understood for magnetized plasmas (plasmas with magnetic fields large enough that the ion gyroradius is small compared to the probe tip)[21][22][23]. The FRC, however, is considered unmagnetized since the density is highest where the magnetic field is zero. Although mach probes are used in unmagnetized plasmas, the assumptions upon which the theoretical models are based are no longer valid. While the magnetized mach probe theory is often applied to unmagnetized plasmas, it is argued that any consistency with other measurements are coincidental[24].

2.3.2 Charge-Exchange Neutral Particle Analysis

Charge-exchange (C-X) is the process by which an electron is transferred from an atom to an ion [25]. After a C-X event occurs, the neutralized ion is no longer affected by the magnetic and electric fields within the plasma, so they continue in their original trajectory before the event occurred. By measuring the velocity and velocity spread of the C-X neutrals emitted from the plasma, the ion velocity distribution function can be obtained. The IFRC plasma is composed of hydrogen and carbon, so charge exchange reactions involving H^+ and C^+ should both be considered. Also, only charge exchange reactions that result in a neutral product need to be considered, since ions will interact with the magnetic field and will not reach the detector.

Charge-exchange neutral particle analysis (NPA) relies on:

1. Sufficiently many charge-exchange reactions take place.
2. The charge-exchanged neutrals can escape the plasma.
3. The neutrals can be detected.

The number of C-X reactions is often expressed in terms of the *emissivity*

$$\varepsilon = n_i n_0 < \sigma v_i > \tag{2.25}$$

which has the units of number of reactions per unit time per unit volume. From (1) it is clear that for a given $< \sigma v_i >$, having a large ε involves maximizing either n_i or n_0. Having a large n_0 however, decreases the mean free path outside of the plasma (in addition to degrading plasma performance) so the optimum application is one where $n_i \gg n_0$. Additional mechanisms that affect (2) include: re-ionization due to electron-impact ionization and neutrals undergoing multiple C-X reactions. These mechanisms are evaluated as they relate to IFRC in Chapter 4.

There are several methods for detecting neutrals. Stripping foils[26] and gas stripping cells[25] in conjunction with an energy analyzer[27] are usually used for energies higher than expected in IFRC. Other methods involve using a scintillating material from which secondary electrons are ejected upon impact by the incident neutrals. As discussed in Chapter 4, the IFRC charge-exchange neutral particle analyzer employs a detector that relies on secondary electron emission.

The implementation of a charge-exchange neutral particle analyzer with magnetic confinement devices is used in many plasma experiments[28]. At the time of this writing, aside from the author's work, there are no publications in which this type of diagnostic is used in an FRC.

2.3.3 Visible Emission Spectroscopy

Visible emission spectroscopy involves the analysis of radiation from atomic transition within a plasma. Typically, a single transition is desired and the observed spectral region is narrow around that particular line. For a plasma in thermal equilibrium, the emission line intensity is best described by a Gaussian

$$I(\lambda) \propto \exp -\frac{(\lambda - \lambda_0)^2}{(2\Delta\lambda)^2} \qquad (2.26)$$

where λ_0 is the average wavelength, and $\Delta\lambda$ is the standard deviation. For an atomic transition from a species whose average velocity is zero, the peak of the emission line is located at the wavelength λ_0. If there is an average drift v, the peak is Doppler shifted to a new wavelength

$$\lambda_{new} = \frac{\lambda_0}{1 - \frac{v}{c}}. \tag{2.27}$$

Measuring the Doppler shift of emission lines is a method of determining the mean ion drift velocity. The temperature of the observed species is related to the line width by

$$\Delta\lambda = \lambda_0 \sqrt{\frac{kT}{mc^2}} \tag{2.28}$$

for Doppler broadened profiles. Spectroscopy has been performed on many FRC experiments and is described in more detail in Chapter 5.

2.4 Ion Flow Measurements

Ion flow measurements using emission spectroscopy have been performed on various field reversed configurations. The FRX-C device was a theta pinch FRC in which the $n = 2$ rotational instability was observed. Emission spectroscopy was performed on the carbon-V impurity line to correlate the rotation with the instability. The primary focus of this work[29] was to show how quadrupole fields can be used to stabilize this instability.

A spheromak merging experiment SSX has measured ion flow using a carbon-III emission line[30]. The measured flow in this experiment was typically in the range of 5 km/s and was relatively uniform as a function of radius. These data are comparable to those measured in IFRC, however further analysis is not presented in the publication.

TS-3 is another spheromak merging experiment that has observed ion flow using a carbon-II impurity[16]. They observed flows in the range of 10 km/s before and after the merging of spheromaks, and used Langmuir probes to get the density profile. From this, the ion current density was obtained. Analysis of magnetic probe data was used to calculate the total current from Ampere's Law, resulting in a total current density approximately three times the ion current. This indicates that the electron flow is in the opposite direction, so it adds to the total current.

2.5 Summary

An equilibrium model has been discussed that describes the electric and magnetic fields, as well as the density profile, within an FRC. The net ion flow in an FRC arises from a combination of betatron and drift orbits. An analysis of the different types of orbits shows that for a net current in the $\hat{\theta}$ direction, the orbits contributing positively to the plasma current are the electron and ion drift orbits (provided that they are dominated by the $E \times B$ drift), and the ion betatron orbits. Orbits that reduce the total current are the electron drift orbits (possibly ion orbits if they are dominated by the ∇B drift). Most FRC formation schemes result in electron dominated currents. Ion flow measurements have been performed in past experiments; however, there is little analysis regarding a comparison with the total plasma current.

Chapter 3

The Irvine Field Reversed Configuration

The Irvine FRC is a relatively new experiment, whose campaign started in 2004. Most of the effort has gone into basic diagnostic development and building critical hardware required to run the experiment and acquire data.

A physical description of the machine including magnetic coil and vacuum vessel dimensions is given in Sec. 3.1. The power supplies and trigger system is outlined in Sec. 3.2. The plasma source is covered in Sec. 3.3. Section 3.4 discusses the data acquisition system. The diagnostics (aside from those covered in the following two chapters) are described in Sec. 3.5.

3.1 Physical Description

The Irvine FRC is a coaxial setup (Figure 3.2) similar to the Coaxial Slow Source[31]. The large (40 cm radius) outer coil, known as the flux limiter coil (also referred to

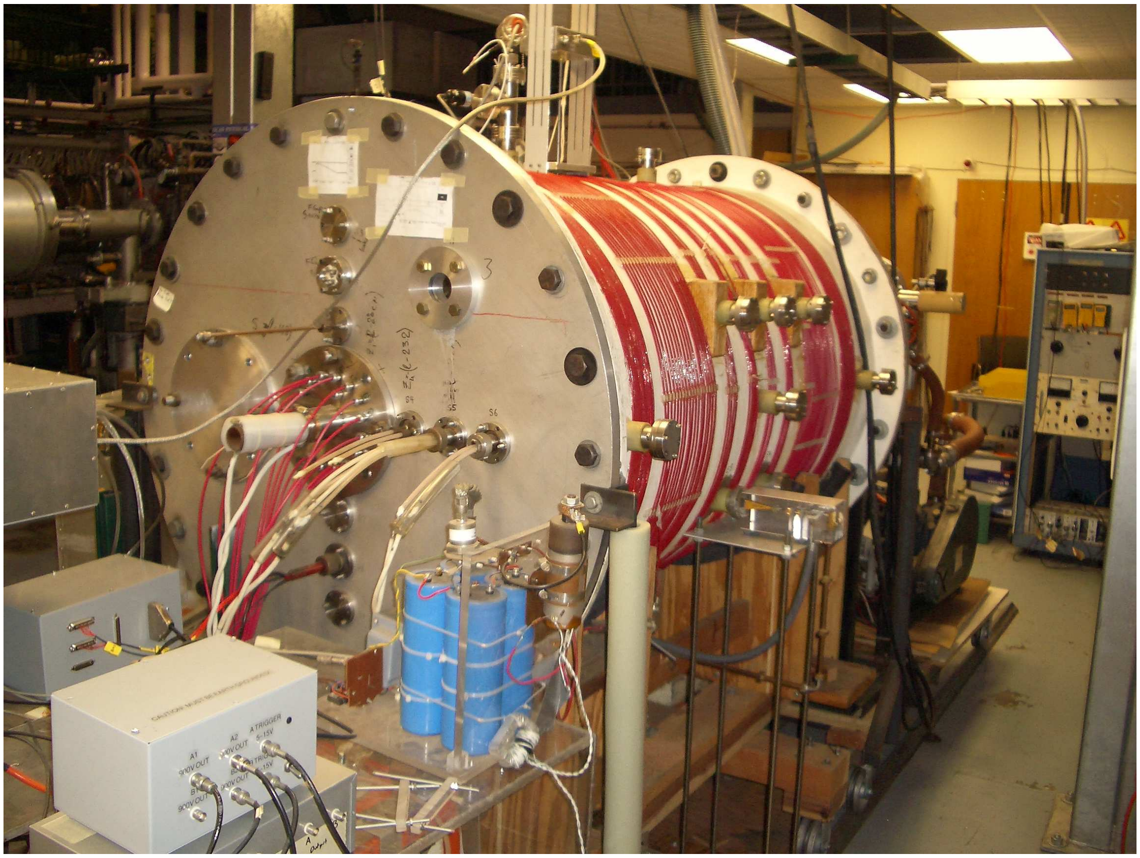

Figure 3.1: Photograph of the Irvine Field Reversed Configuration.

as a limiter coil or container coil), is used to setup the background magnetic field. It is composed of six aluminum straps 5 cm wide and ∼3 mm thick, evenly spaced over the 60 cm distance between the north and south plasma guns (described below). Typical currents through the entire coil are around 14,000 A (or 2.3 kA per strap) which results in a peak field of around 250 Gauss.

The inner coil, called the flux coil, is what drives the plasma current into field reversal. It consists of four parallel windings, each one with a pitch of 22 turns/m with a 10 cm radius and 1.3 m long. The length of the flux coil was chosen to be much longer than the plasma confinement region in order to reduce the amount of return flux that cancels the background magnetic field. Typical currents are around 15 kA producing an internal field of around 5000 Gauss. The current flows in such a

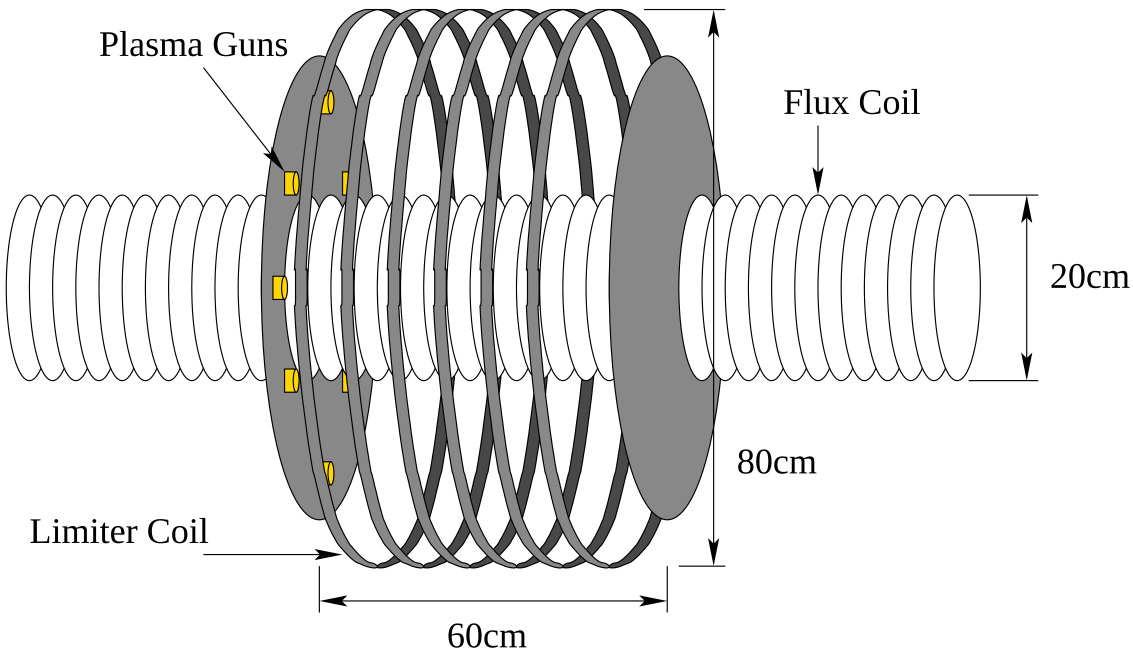

Figure 3.2: IFRC coil geometry.

Coil	Radius (cm)	Length (cm)	Inductance (μH)
Flux	10	150	19
Limiter	40	60	3.1

Table 3.1: IFRC coil characteristics.

way that the field inside the flux coil is in the same direction as the field inside the container coil. The physical properties of the two coils are summarized in Table 3.1.

The coils are both enclosed in a 1.5 m long, 1 m diameter fiberglass vessel that is presently pumped by two diffusion and mechanical pumps to a base pressure of 3×10^{-6} Torr as measured by an ion gauge connected to the main vessel. The pressure is monitored at four other locations, two on the main chamber, and one at each of the foregates of the diffusion pumps by ConvecTorr gauge tubes from Varian, Inc. The ConvecTorr gauges controller is connected to an interlock which closes the diffusion pump gates in the event that any of the gauges read a pressure higher than a specified set point (typically 5 mTorr). The interlock prevents damage to the diffusion pump caused by running it at high pressure in the event of a sudden vacuum leak.

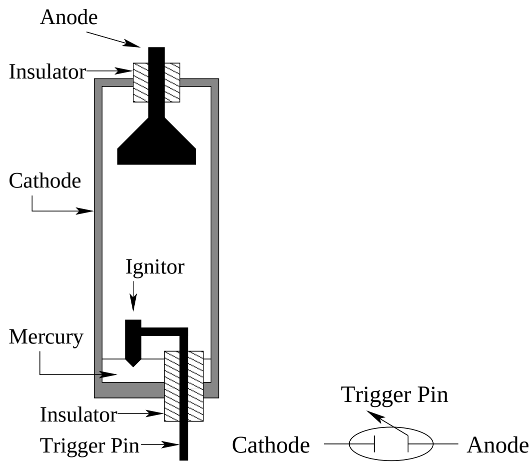

Figure 3.3: Ignitron schematic.

3.2 Power Delivery System

All of the power supplied to the FRC (magnetic field coils and plasma guns) is delivered by a capacitive discharge through a three terminal device called an ignitron, shown in Fig. 3.3. An ignitron contains a pool of mercury in the bottom that must be ionized in order to conduct across the anode and cathode. Conduction is made possible when a high voltage ($> 1\ kV$) pulse lasting for a few ($\leq$3) microseconds is applied across the trigger pin and the cathode, while there is a positive voltage between the anode and cathode (minimum value typically $\sim$50 V). It is also possible, as in the case of the crowbar circuitry, for the ignitron to conduct with a smaller voltage (i.e., a few hundred volts) on the trigger pin provided that it is for a longer period of time (tens of microseconds).

The charging and dumping of the high voltage capacitor banks is illustrated in Fig. 3.4. When the dump switch, D, is opened, the capacitor banks are connected to the high voltage power supply through a large charging resistor, R1, typically around 100 kΩ. This resistor limits the current drawn from the high voltage power supply to a few tens of milliamps. After firing the system, or in the event that the capacitor

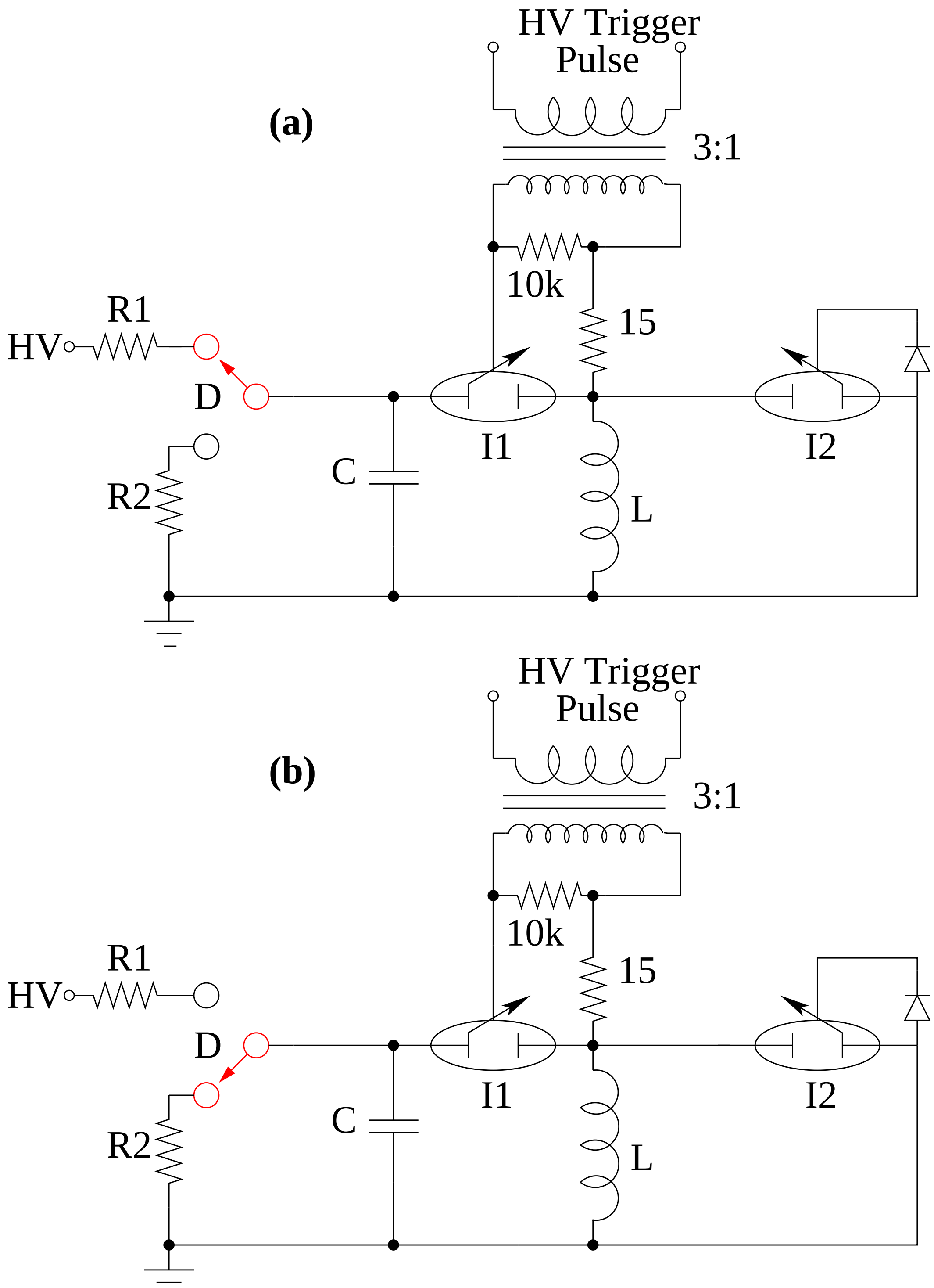

Figure 3.4: Dump switch conditions for charging capacitor banks. (a) Dump switch is open and capacitors can be charged through R1. (b) Dump switch is closed and the capacitor is shorted through R2.

banks need to be discharged, the dump switch can be closed to provide a current path through resistor R2. This resistor value is chosen so that the RC time constant is only a few seconds to prevent the capacitor discharge from taking a very long time.

Discharging the capacitors through the magnetic field coils requires triggering the ignitron, as explained above. The ignitron trigger pulse originates from a high voltage pulsing circuit, shown in Fig. 3.5. This 600 V pulse is stepped up by a 3:1 iron-core transformer and is applied across the trigger pin and cathode. The purpose of the transformer is to step up the voltage and isolate the pulsing circuit (which contains sensitive electronic components) from the high voltage capacitor banks.

When the system fires, a high voltage ($\sim$1500 V) trigger pulse drives an ignitron into conduction, shown as I1 in Fig. 3.6a. Initially, I2 is still open so no current flows through that part of the circuit. The capacitor bank C is connected directly across one of the coils, which is an inductor with inductance L. This LC circuit now begins to oscillate (though a quarter of a complete cycle) with frequency $1/\sqrt{LC}$ until the crowbar triggers.

The crowbar, shown switched in Fig. 3.6b, is used to prevent the capacitor bank from reversing its polarity. After the LC circuit has oscillated a quarter of a cycle, the voltage on the capacitor is decreasing through zero and goes negative. Since the anode of the ignitron is connected to ground, it is now positive relative to the negative cathode. Similarly, the trigger pin is positive relative to the cathode and when the capacitor voltage goes low enough (typically a few hundred volts), the Ignitron conducts causing a short across the inductor (magnetic field coil). At this point in the LC circuit, the current through L has reached it maximum and when I2 conducts, the current decays as L/R, which is very large since R is just the resistance of the coil and wires (a few Ohms).

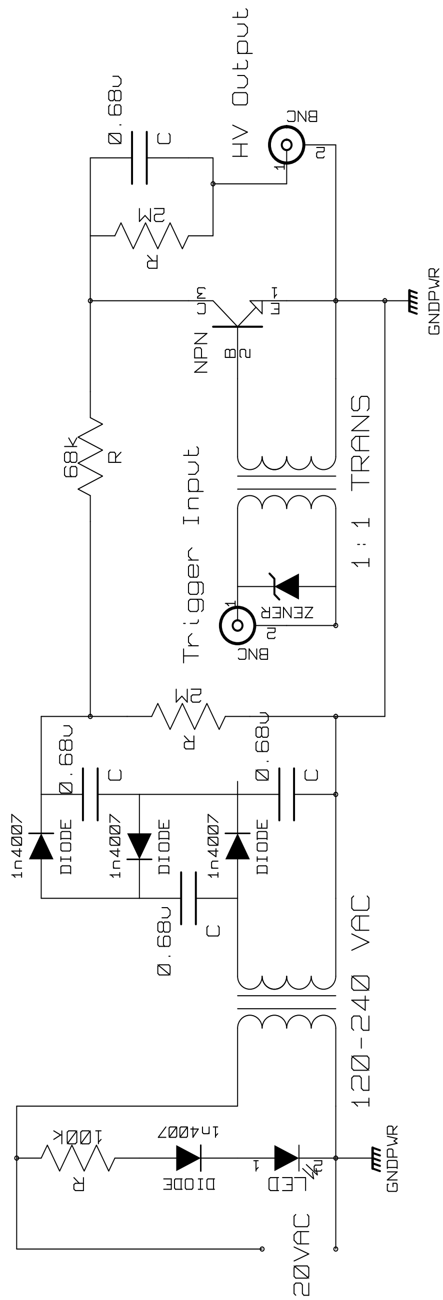

Figure 3.5: Ignitron pulser

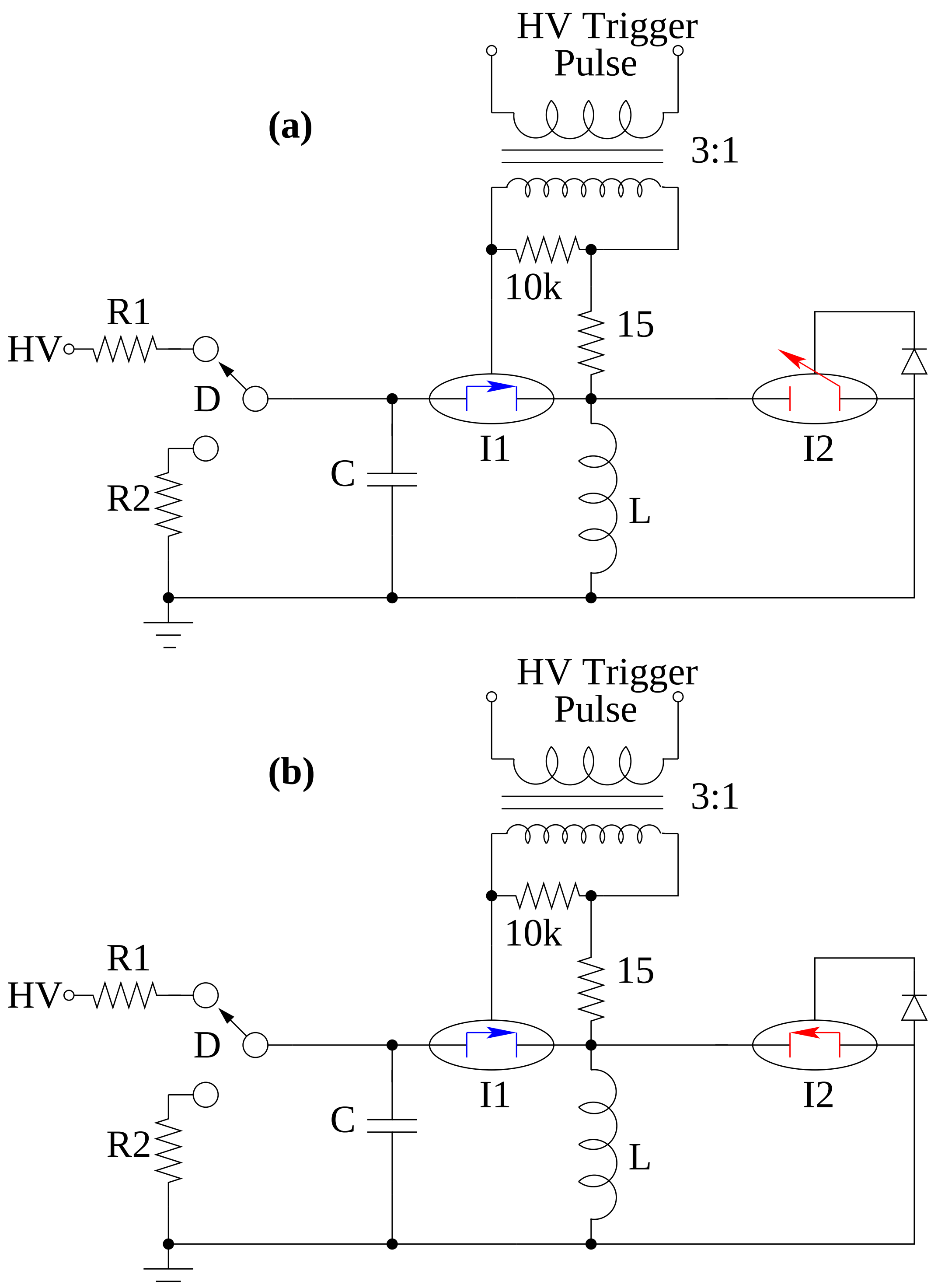

Figure 3.6: Ignitron triggering while firing capacitor banks. (a) Initial firing of capacitor banks. (b) Ignitron crowbar is switched.

3.3 Plasma Source

The plasma source consists of 16 cable guns, 8 on each side of the vacuum vessel. Each cable gun consists of a length of RG-8 coaxial cable with the tip bored out creating a 45° cone. The dielectric is polyethylene which is a long chain of the ethene molecule C_2H_4. When the plasma guns are fired, high voltage (typically ∼16 kV) is applied across each cable gun causing an arc to form across the polyethylene insulator. The arc, which consists of electrons, ionized hydrogen and carbon, has a radial current component J_r and a toroidal magnetic field component B_θ and consequently is ejected from the gun as a result of the $J_r \times B_\theta$ force. It should be noted that evidence of metal from the plasma gun conductors has not been observed, as determined by spectroscopy performed on radiated light from the plasma. Since all of the cable guns are in parallel, a ∼4 Ω ballast resistor is connected in series between each gun and the high voltage capacitor. The ballast resistors, consisting of a water and copper sulfate solution, prevent excessive current from being drawn through a single gun if it happens to arc before any other.

3.4 Data Acquisition

Data from the diagnostics are primarily stored in a custom built Faraday cage containing 26 BitScope digital storage oscilloscopes[32]. Each BitScope has four 8-bit channels, can store up to 128 kSamples, and a variable sampling rate up to 40 MSamples/s. The BitScopes are networked using an ethernet switch, which is connected to a fiber optic converted prior to exiting the Faraday cage. The optical signal is converted back and downloaded to a personal computer running Lab2000 data acquisition software[33]. Tektronix TDS 2014 digital storage oscilloscopes are also used

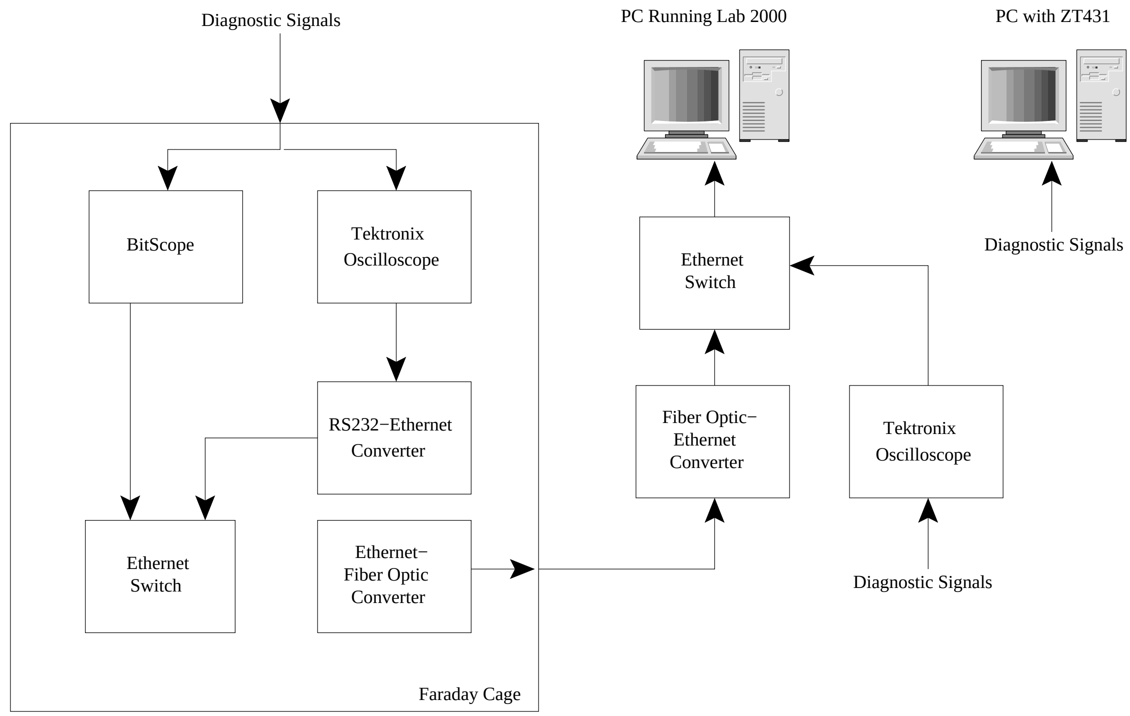

Figure 3.7: Data acquisition system.

for data acquisition, however they use a SitePlayer (RS232 to ethernet protocol converter) in order to network with the BitScopes. An ethernet switch is also located outside of the Faraday cage for signals that are acquired far away from the pulsed capacitor banks that are less influenced by the switching noise. An additional computer has a ZT431 digitizer which has two 12-bit channels, can store up to 8 MSamples, and has a sampling rate up to 200 MSamples/s (for 1 channel only). Data from this card are viewed and stored using ZScope C-Class software, from ZTEC Instruments. A schematic for the data acquisition system is shown in Fig. 3.7.

3.5 Diagnostics

The diagnostic suite at IFRC consists of several magnetic probe arrays to measure all components of the magnetic field throughout the plasma, a Rogowki coil to measure the total plasma current, a Langmuir probe for density measurements, a charge-exchange neutral particle analyzer, and a spectrometer for optical measurements. For a brief period in early 2008, a second harmonic interferometer was used to measure the line-integrated plasma density[34]. This chapter will discuss the magnetic, Rogowski, and Langmuir probes. The charge-exchange analyzer and spectrometer are discussed in the following chapters since they are covered in more detail.

3.5.1 Magnetic Coils

All of the magnetic probes used in this experiment are loops of wire whose measurements are based on Faraday's Law of Induction. For a single current loop, as shown in Fig. 3.8, the induced EMF $\mathcal{E}$ is

$$\mathcal{E} = -\frac{\partial \Phi}{\partial t} \tag{3.1}$$

where

$$\Phi = \int_A \mathbf{B} \cdot d\mathbf{A}. \tag{3.2}$$

For typical charging parameters, and a probe cross-section of $\sim$50 mm^2, $\mathcal{E}$ <20 mV for a single loop. Since typical noise levels when the capacitors switch can be over 100 mV so it is desirable to increase the signal to noise ratio by adding more loops to the magnetic probe.

There are three magnetic probe arrays presently in use in IFRC. Two axial arrays measure the $\hat{z}$-component at the innermost and outermost radii. The outer array (located at r = 37 cm) has 8 probes uniformly spaced 7 cm between probes. The inner array (located at r = 11 cm) has 15 probes with variable spacing between 3 cm (at the midplane) and 7 cm (at the ends). A radial probe array has three probes at

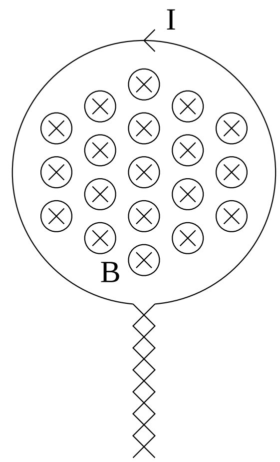

Figure 3.8: Single turn magnetic loop.

each radial coordinate to measure all three magnetic field components (B_r,B_θ,B_z). The radial spacing between each set of probes varies between 1 cm (at $r = 23$ cm the null surface) and 3 cm (at the outermost radius). For magnetic field mapping, the radial array can be placed at any of 12 positions between the limiter coil straps.

Since the outputs from magnetic probes such as these are proportional to dB/dt, they must be integrated to get $B(t)$. Passive (RC) integrators were used in the past, however they reduce the signal by a factor of $1 + \omega RC$ which can be greater than 40 for a reasonable choice of RC. By integrating numerically, a larger signal is measured and the probes are made with few turns and smaller area.

3.5.2 Rogowski Coil

A Rogowski coil is a solenoidal coil in the shape of a torus (in most cases). Like magnetic probes, its signal is generated through magnetic induction. Consider the coil in Figure 3.9, with n turns per unit length and a loop cross-section A. The induced EMF, $\mathcal{E}$, and flux Φ is the same as before. For N loops along the line l, and for a spatially uniform magnetic field, we can sum the contributions to each loop

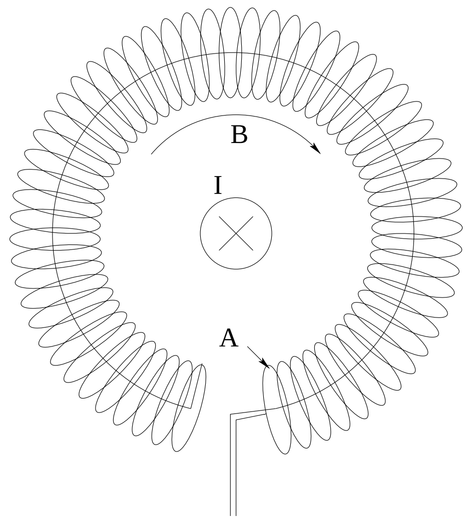

Figure 3.9: Typical Rogowski coil.

simply by:

$$\Phi = N \int_A \mathbf{B} \cdot d\mathbf{A} \tag{3.3}$$

since the integral is the same for all loops. Realistically, there is some spatial variation that must be taken into account. So N is replaced by $n \sum_{dl} dl$, where n is the number of turns per unit length and the sum is over the entire length of the coil. For a tightly wound coil, the sum can be written as an integral:

$$\Phi = n \oint_l \int_A \mathbf{B} \cdot d\mathbf{A} dl = n \oint_l \int_A dA \mathbf{B} \cdot d\mathbf{l} \tag{3.4}$$

where we have used the fact that the line element $d\mathbf{l}$ points in the same direction of $d\mathbf{A}$. Rearranging the integral, we have

$$\Phi = n \int_A \oint_l \mathbf{B} \cdot d\mathbf{l} dA \tag{3.5}$$

and from Ampere's Law

$$\oint_l \mathbf{B} \cdot d\mathbf{l} = \mu I \tag{3.6}$$

we have

$$\Phi = nA\mu I. \tag{3.7}$$

So the induced voltage is therefore

$$V = \mathcal{E} = -nA\mu\dot{I}. \tag{3.8}$$

Since the output of the Rogowski coil is proportional to the derivative of the current, the signal must be integrated to obtain the actual current. A simple circuit model for the Rogowski coil L with integrator $R1$-C and oscilloscope with impedance $R2$ is in Fig. 3.10. The equivalent (real) impedance for R_2 and C in parallel is

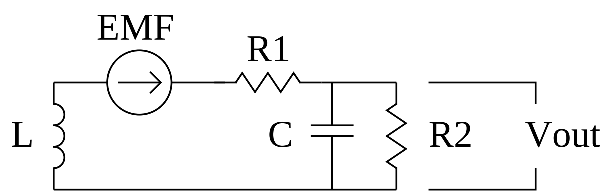

Figure 3.10: Rogowski coil with integrator circuit model.

$R_\parallel = R_2^2/(R_2^2/\omega^2 C^2 + 1)$. Adding the resistance of the integrator gives $R_{eq} = R_\parallel + R_1$ and the circuit is shown in Fig. 3.11. For a current I flowing through the loop, the

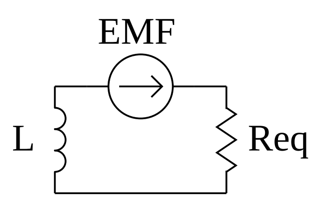

Figure 3.11: Simplified Rogowski circuit.

current loop is expressed as

$$\frac{EMF}{R_{eq}} = \frac{L}{R_{eq}}\frac{dI}{dt} + I. \tag{3.9}$$

Considering the frequency components of $I \to I\exp(i\omega t)$ this becomes

$$\frac{EMF}{R_{eq}} = I\left(i\omega\frac{L}{R_{eq}} + 1\right). \tag{3.10}$$

For $\omega L/R_{eq} \ll 1$, the current is approximated by

$$I \approx \frac{EMF}{R} \tag{3.11}$$

which is referred to as B-dot mode because the current is proportional to the EMF, which is proportional to the time derivative of B. For the coil used in IFRC L =351 μH, $R_1 = 3.3$ kΩ, $C = 3.46$ μF, and $R_2 = 1$ MΩ. These parameters result in $\omega L/R_{eq} \ll 1$ for $\omega < 1$ Mrad/s as shown in Fig. 3.12. From this it is clear that from time scales

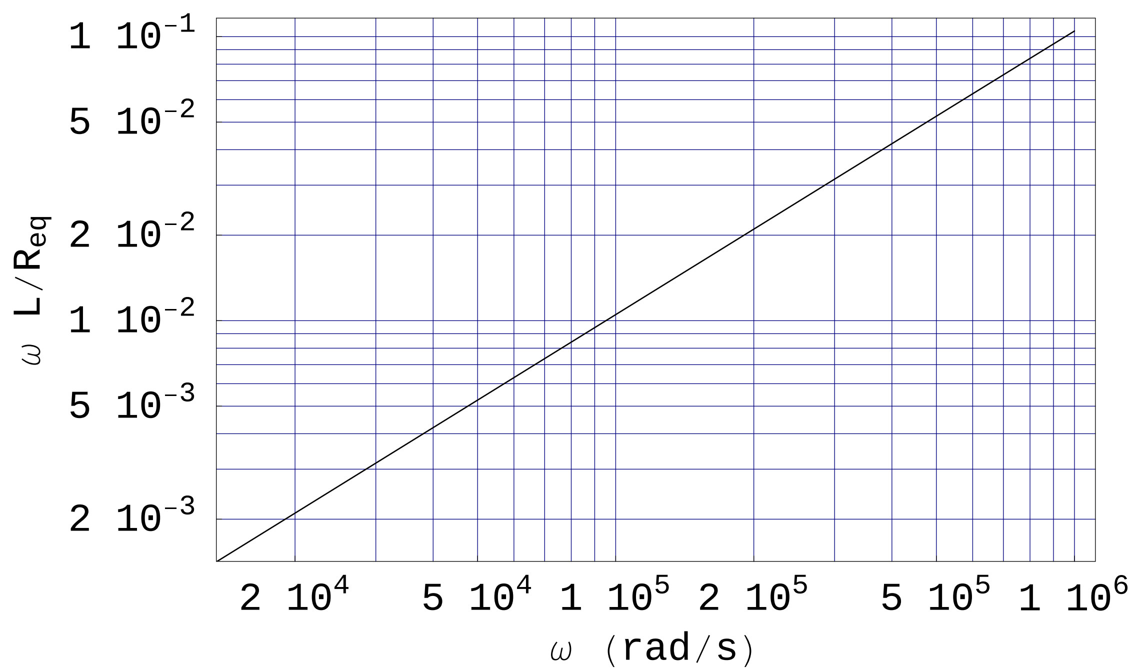

Figure 3.12: Frequency dependence of $\omega L/R$.

longer than 1 μs the induced current is proportional to $\dot{B}$. A similar analysis places a constraint on the integrator components C and R_1 which is $\omega RC \gg 1$. The lifetime of IFRC is typically around 80 μs so R_1C is chosen to be ~10 ms.

The plasma current is measured by a Rogowski coil which sits in the r-z plane. This coil was constructed using 29 AWG magnet wire wrapped on a 1/4" Delrin rod. The wire was wrapped so that there was no space between adjacent coils. The coil spacing is, therefore, equal to the wire spacing which is 0.009". A 0.005" walled stainless steel tube is placed over the coils to shield from electro-static fields along the axis of the coil. To ensure that the time-dependent magnetic field produced from the plasma current could penetrate through the metal tube without being cancelled by eddy currents, the wall thickness was chosen so that is much smaller than the skin depth, δ:

$$\delta = \sqrt{\frac{\sigma}{\omega \mu_0}} \tag{3.12}$$

where σ is the conductivity and ω is the frequency of the time-dependent field. For 304 Stainless Steel, the conductivity is 1.5×10^6 siemens/m giving a skin depth of ~400 m at 1 MHz, much larger than the 0.1 mm thick tube.

To prevent the metal shield from shorting out any electric fields in the plasma, each part of the coil was inserted into a glass tube, whose outer diameter was 10 mm. The coil was assembled by forming a rectangle using two 55 cm lengths and two 25 cm lengths of each section.

Calibration of the coil was accomplished by passing a known current through it and measuring the output voltage. The present coil in use has a calibration constant of 1.06×10^4 A/Vms. The units reflect the fact that to arrive at the current flowing through the coil, one must multiply the measured voltage by the calibration constant and the integration time. The induced voltage from magnetic fields alone (no current present) was tested by firing the magnetic field coils with no plasma in the system. This results in no measureable voltage when firing at the maximum charging voltages on the coils.

Rogowski coils are also used to measure the current in the applied magnetic field coils (Flux and Limiter Coils). The coil currents are measured using probes constructed similar to Figure 3.9 and the cable passes through the center. Calibration is performed using the same method described above.

3.5.3 Langmuir Probe

Langmuir probes have a single conducting tip inserted into a plasma with a voltage applied relative to the plasma potential[25]. For an applied voltage sufficiently low compared to the plasma potential, all electrons are reflected and the measured current is the ion-saturation current. The ion-saturation current I_{sat} is used to measure the electron density n_e by

$$I_{sat} = \exp\left(-\frac{1}{2}\right) A_s n_e \left(\sqrt{\frac{T_e}{m_i}}\right) \tag{3.13}$$

where A_s is the area of the sheath surface around the probe (usually approximated by the area of the probe).

The probe used in IFRC is actually a modified Langmuir probe, called a Mach probe, that has two probe tips that measure I_{sat} upstream and downstream of a flowing plasma. The plasma drift velocity is found from the relative I_{sat} measurements, and is given by

$$\frac{I_U}{I_D} = \exp\left(4\sqrt{\frac{T_i}{T_e}} u_m\right) \tag{3.14}$$

where I_U and I_D are the upstream and downstream I_{sat}'s, and the Mach number u_m

is defined as

$$u_m \equiv \frac{v_d}{\sqrt{T_e/m_i}} \tag{3.15}$$

with v_d being the plasma drift velocity[35]. This model[21], however, is based on the plasma being magnetized (small gyro-radius compared to probe tip size), collisionless, and $T_i \ll T_e$, all three of which are not satisfied in IFRC. In addition, the model requires $u_m \ll 1$ which contradicts the initial expectations of IFRC ($c_s \sim 22$ km/s and $v_d \sim 90$ km/s from Chapter 2). The inapplicability of this model to unmagnetized plasmas results in an incorrect "calibration factor," which is term multiplied by the Mach number in Eq. 3.14[24]. Not knowing what this factor should be in an FRC makes the probe useful only for qualitative flow measurements.

Actual probe data gives a ratio of I_{sat} measurements between 0.4 and 1.2, which covers a range not allowed in the Mach probe model ($u_m > 1$). In addition, the relative amplitudes of the I_{sat} measurements were not consistent when changing probe orientations; relative amplitudes indicating flow in one direction did not indicate flow in the opposite direction when reversed. As a Langmuir probe, the probe works quite well and gives densities within an order of magnitude of those measured by the interferometer.

Chapter 4

Time-of-Flight Neutral Particle Analyzer

Time-of-flight (TOF) has proven to be successful in experiments where low energy (<1 keV) neutrals are of interest[36, 37, 38, 39]. The diagnostic used in IFRC is primarily based on the low energy neutral spectrometer (LENS) implemented in the PLT Tokamak in the 1980's [36]. The primary goal of this is to obtain the time-resolved ion velocity distribution, which is accomplished through the following processes shown in Fig. 4.1:

1. Hydrogen ions in the plasma undergo charge-exchange reactions with background neutral Hydrogen.

2. The neutral hydrogen passes through a collimating slit to restrict the amount of plasma seen.

3. The collimated neutrals are chopped by a slotted disk (chopper) rotating with a frequency of 10,000 RPM.

4. The chopped neutrals become spatially ordered as the faster particles reach the detector sooner than the slower ones.

5. The neutrals incident on the detector undergo electron multiplication to convert the neutral particle beam into a measurable electric signal.

Several changes have been employed in an attempt to simplify previous TOF diagnostics. The Cu-Be plate used in prior diagnostics for secondary electron emission was necessary to boost electron multiplier signals whose gains did not exceed 10^5 [36]. Channel electron multipliers (CEM), like the one in this diagnostic, have a gain larger than 10^7 allowing the Cu-Be plate to be eliminated. Therefore, the neutrals hit the CEM directly, utilizing the fact that CEMs respond to neutrals[40]. This allows the geometry to be simplified as the detector is along the same axis as the line of sight.

Another difference is that the slotted disk is driven by a radio-controlled (RC) airplane brushless motor directly in vacuum. This motor has ball-bearings, which avoids the magnetic bearing motor and associated instabilities[36, 41]. A turbo pump has been used before, however RC airplane motors and controllers are much more readily available and are typically 1% of the cost[37, 38]. This also eliminates the need for a separate motor vacuum chamber[39].

Since the IFRC lifetime ($\sim$80 μs) is comparable to the chopping period, it is important to be able to control when the distribution function is being sampled during the plasma discharge. To accomplish this, a synchronization circuit has been developed that utilizes a reference laser similar to those employed by previous diagnostics[37, 38, 39]. Although the reference laser has been introduced for timing referencing in the past, it has not been used for synchronization. A complete electrical layout with all components is shown in Figure 4.2; however, the details of the various components are covered in the following sections.

This chapter discusses the time-of-flight diagnostic used for charge-exchange neutral particle analysis at IFRC. In Sec. 4.1, the relevant charge-exchange reactions along with their respective cross sections are discussed. Section 4.2 is a feasibility study prior to the development of the diagnostic. The criteria for parameter selection are explained in Sec. 4.3. The driving motor is discussed in Sec. 4.4. Section 4.5 covers the slotted disk along with the rotation frequency measurement. The detector and its implementation are described in Sec. 4.6. Calibration of the timing between the chopper and reference laser is in Sec. 4.7. Section 4.8 covers the calibration of the complete diagnostic using a lithium ion source. The calculation required to convert the detector signal into the energy distribution function is discussed in Sec. 4.9.

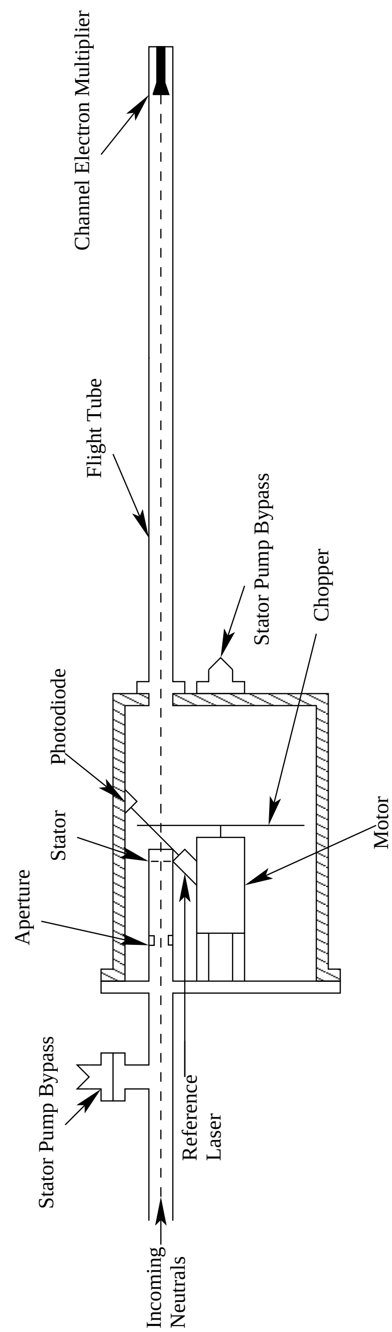

Figure 4.1: The time-of-flight diagnostic

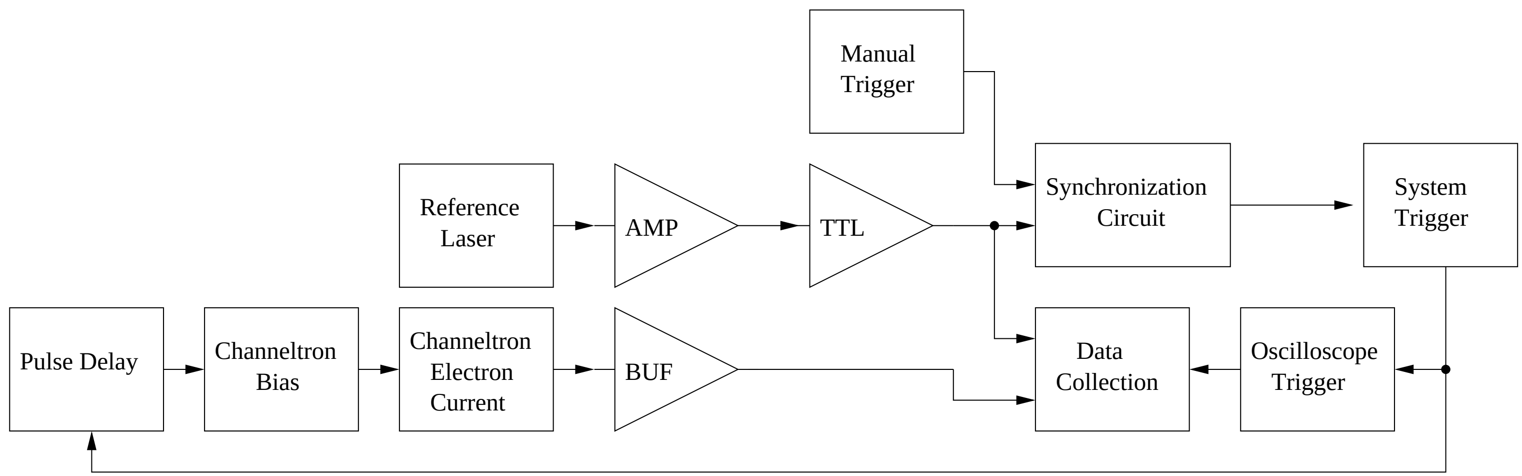

Figure 4.2: Electrical schematic of TOF system.

4.1 Charge-Exchange Considerations

As explained in Chapter 2, charge-exchange is the transfer of an electron from one atom to another. The time-of-flight diagnostic relies on charge-exchange reactions to carry information (such as ion velocity distribution and temperature) about the ions away from the plasma. In IFRC the plasma source produces hydrogen and carbon. The relative charge-exchange cross sections in the expected energy range are evaluated here to determine whether hydrogen or carbon reactions are more likely to occur.

For atomic hydrogen, the relevant charge-exchange reaction is

$$H^0 + H^+ \rightarrow H^+ + H^0 \tag{4.1}$$

and the cross section is shown in Fig. 4.3. As shown, there is only 20% difference in

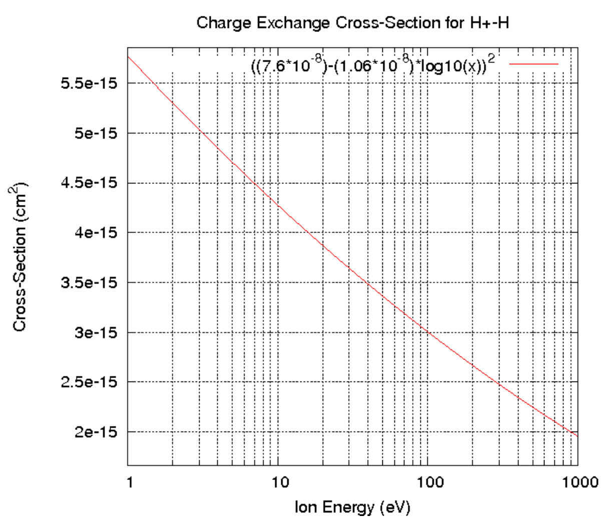

Figure 4.3: Hydrogen charge-exchange cross section.

cross section over the expected energy range, 10 to 100 eV. For neutral hydrogen and singly ionized carbon, the charge-exchange cross section for the reaction

$$H^0 + C^+ \rightarrow H^+ + C^0 \tag{4.2}$$

is several orders of magnitude less than hydrogen over the same energy range, as shown in Fig. 4.4. For 100 eV ions, the cross section is $\sim 10^{-21}$ cm^2 for charge-

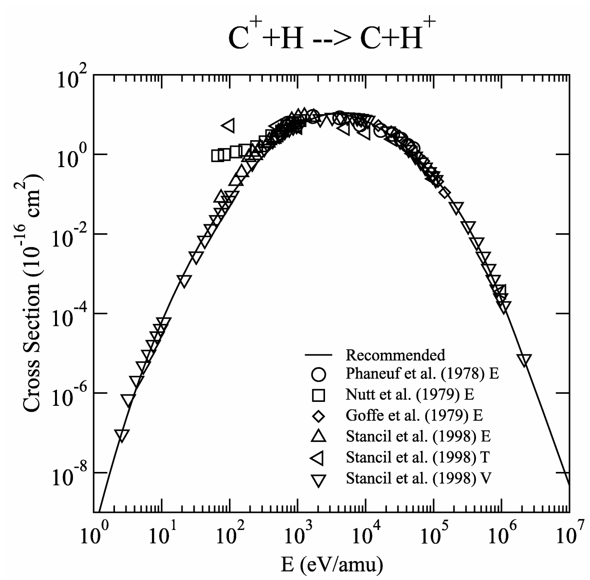

Figure 4.4: Carbon charge exchange cross section. [42]

exchange with neutral carbon compared to $\sim 10^{-15}$ cm^2 for hydrogen. Based on this, it is assumed that the detected neutrals in IFRC are predominantly hydrogen.

4.2 Feasibility

An estimate of the number of charge-exchange neutrals that reach the detector is calculated from the emissivity (Eq. 2.25) Triple probe data at the time of this calculation gave a density $n_i \sim 5 \times 10^{12}$ cm^{-3}. The neutral density is estimated from the vacuum pressure ($\sim 5 \times 10^{-6}$ Torr) using the ideal gas law, giving $n_0 \simeq 10^{11}$ cm^{-3}. The ion velocity is estimated to be 35 eV, as described in Chapter 2 (though later measurements show a much lower velocity). At this energy, the charge exchange cross section is $\sim 3.6 \times 10^{-15}$ cm^2 [43]. From this, the emissivity is $\varepsilon = 1.4 \times 10^{16}$ particles/s/cm^3. Projecting a proposed detector size ($\sim$1 cm diameter) through the stator slits onto the plasma, gives an ellipse with a major and minor axis of 5 mm and 1.7 mm, respectively. This ellipse has an area of 27 mm^2 and if we estimate the length of the plasma viewed to be 10 cm, we have a viewable plasma volume of 2.7×10^4 mm^3. The emissivity multiplied by this volume gives 3.7×10^{16} particles/s emitted from this volume. Since the ions are orbiting due to the magnetic field, their velocities before charge exchange are not all in the same direction. Assuming that any direction is equally likely, we can multiply this count rate by the scale factor equivalent to the detector size divided by the area of a sphere whose radius is equivalent to the plasma-to-detector distance. For the 1 cm diameter detector at a distance 2 m from the plasma, the scale factor is 1.56×10^{-6}. This results in an expected 5.8×10^4 neutrals hitting the detector every microsecond. For microchannel plates, the absolute detection efficiency for neutral hydrogen has been experimentally measured to be between 0.005-0.02 at energies between 20-40 eV. From this, it is expected that around 300 neutrals should be detected per microsecond.

4.3 Diagnostic Parameters

The dimensions of the slotted disk and flight tube length are determined by considering the different time scales involved. For a standard shot, typical time scales are:

- FRC lifetime of $\sim$80 μs

- FRC formation time of $\sim$10 μs

These FRC time scales are used to determine the following chopping time scales:

- t_o, is the time that the slit is open for neutrals to pass through
- t_s, is the time between successive slit openings

A constraint is placed on the relationship between t_o and t_s to achieve spatial ordering, meaning the neutrals arrive at the detector according to their velocity. Specifically, the requirement $t_o \ll t_s$ must be satisfied in order to minimize the amount of neutrals with different velocities hitting the detector at the same time. This is quantified by the uncertainty in arrival time measured by the detector, as discussed later.

The chopping frequency $1/t_s$ is chosen based on how many times the distribution function is to be sampled within a given shot. In order to have a time resolved energy distribution, t_s must be chosen such that there are many chops within the FRC lifetime. It is desirable to have as many of these as possible, however there are several physical limitations that will be pointed out throughout the section. The parameters are evaluated by choosing a potential number of samples, say 10 (which can be modified later), at the chopping frequency (determined later) and adjust it as necessary.

From t_s we can obtain the flight distance L between the chopper and the detector using the lowest expected velocity. As mentioned in Sec. 4.2, the expected average drift velocity is in the range of 35 eV. Previous experiments show that the detection efficiency is quite steep in this range, differing by over a factor of two between 30 eV and 20 eV [40]. The calibration for this cuts off at 20 eV, but to ensure that nothing with lower energy interferes with subsequent distributions, the low energy limit for the diagnostic is taken to be 10 eV. From this, the maximum length that will allow those neutrals to reach the detector before the next sample is performed by the chopper is just

$$L = \frac{t_s}{v_{10eV}}. \tag{4.3}$$

Calculating the maximum acceptable value for t_o requires choosing an acceptable energy uncertainty. To calculate the uncertainty, the aperture function $A(t)$ must first be introduced. The aperture function represents the time dependent area of the chopper that is open for particles to pass through. It is given by

$$A(t) = \begin{cases} A_{slit}(1 - \frac{|t|}{t_g}) & |t| \leq t_g, \\ 0 & |t| > t_g \end{cases} \tag{4.4}$$

where A_{slit} is the area of the chopper slit, and t_g is half of the total gate time t_o. Since the chopper rotation frequency is constant, $A(t)$ takes a triangular form. The theoretical uncertainty, $\Delta E/E$, is computed by

$$\frac{\Delta E}{E} = \frac{E(v) - E(\frac{L}{L/v+t'})}{E(v)} \tag{4.5}$$

where $E(v)$ is the energy for a velocity v, $L/(L/v+t')$ is the shift in velocity resulting from the finite open time of the chopper and t', obtained by integrating the aperture function, is the time at which all but e^{-1} of the transmitted particles pass through the chopper. By choosing the desired uncertainty at the largest expected energy, a value for t_o is found.

parameter	t_o	t_s	L	f	N
value	2.5 μs	76 μs	1.5 m	165 Hz	80

Table 4.1: Resulting chopper parameters determined by the prescribed method. Initially N was 160 and t_s was 38 μs, however a second chopper was made with 80 slits to block very low velocity neutrals.

Now, t_o is related to the disk parameters (d, the slit width, R, the radius where the slits are located, and f, the rotation frequency of the disk) by

$$t_o = \frac{d}{\pi R f}. \tag{4.6}$$

From this, it is apparent that d needs to be small, while R and f need to be relatively big in order to keep t_o small. A constraint placed on the minimum value of d arises from the manufacturing process involved. Because of the tight tolerances and small slit capabilities, the disk was manufactured using photochemical etching by Fotofab, Inc. Dimensional tolerances for this process are typically $\pm 10\%$ of the metal thickness while the minimum slot size is 1.2 times the metal thickness. The thinnest metal available for use at FotoFab is 0.005" which gives d = 0.006" and a tolerance of $\pm$0.0005".

Equation 4.6 reduces to an expression relating R and f by $R \propto 1/f$. The problem with this is that it is desirable to have both f and R small quantities. To resolve this, the maximum rotation frequency is chosen to fall within the operating range of available brushless motors which is 30,000 RPM, or 500 Hz. This gives a value for R based on the other chosen quantities. The number of slits on the disk N is related to the chopping period by

$$t_s = \frac{1}{\pi R f N}(\pi R - N d), \tag{4.7}$$

allowing N to be chosen once all the other parameters are determined. The chopper parameters obtained through the described process are summarized in Table 4.1.

It should be noted here that taking data from IFRC reveals a flaw with this procedure. Originally, the number of slits was 160 and t_s was 38 μs. Low energy neutrals (<10 eV) were observed and were overlapping with data from the subsequent distribution. Decreasing the number of slits to 80, thereby increasing t_s by a factor of two, resolved this issue. It should be noted that although neutrals in the range of 10-20 eV are observed, the Channeltron detection efficiency is not known in this range. Because of this, the data are restricted to energies greater than 20 eV.

4.4 Chopper Driver

4.4.1 Brushed vs. Brushless Motors

Because the disk is in vacuum, either a feedthrough capable of allowing rotations up to 30,000 RPM or a motor capable of being run in vacuum is required. Ferrofluidic feedthroughs are only capable of rotating up to ~7,500 RPM, much lower than what is required for this application. A turbomolecular pump was certainly a possibility, however, a remote-controlled (RC) airplane motor is used since they are about 1% of the cost.

There are two classes of electric airplane motors: brushed and brushless. A brushed motor is much simpler to work with since its frequency is controlled by an applied DC voltage. A brushless motor requires a special controller (called an electronic speed controller, or ESC) since its commutation is controlled electrically. To determine which type of motor works best in vacuum, a comparison of their performance is presented.

A sample load machined out of $\frac{1}{8}$" thick aluminum with a radius of 3.1 cm is used instead of the actual disk to avoid unnecessary damage. This is designed to have the same moment of inertia of a 0.005" thick titanium disk of radius 6 cm. This was a very early stage of development and it was later decided that a 12 cm radius stainless steel disk should be used, however the conclusions about the motors remain the same. In order to measure the rotation frequency, a 3 mm hole is drilled completely through the disk at a 2 cm radius to allow light from a LED to pass through and hit a photodiode connected to a circuit, as shown in Fig. 4.5.

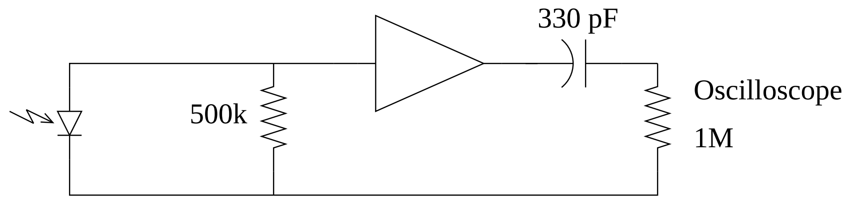

Figure 4.5: Photodiode circuit for RPM measurement.

The 500 kΩ photodiode load is chosen to provide a large voltage input into the buffer whose input impedance is 5 MΩ. The 330 pF capacitor in series with the 1 MΩ oscilloscope internal impedance act as a high pass filter to suppress large 60 Hz noise.

The main concerns regarding motor vacuum performance are: a steady, high (500 Hz) rotation frequency and a slow temperature increase. Both motors have a temperature limit of 93°C because the Neodymium rotor magnets can be damaged at high temperatures. Motor temperature is monitored using two thermistors- one at each end of the motor along the axis of rotation. For the thermistors used, 85°C corresponds to 150 Ω so that is the chosen cut-off point.

After pumping down to a pressure of 50 mTorr, 2 volts applied to the brushed motor raises the temperature to above 85°C in under 30 seconds. The brushed motor requires 20 V to spin up to 30,000 RPM. With this in mind, the brushed motor is not a good candidate.

At the same pressure level, it takes approximately five minutes for the temperature to rise to the same level for the brushless motor while rotating at 30,000 RPM. Based on these findings, the brushless motor is used for the diagnostic.

4.4.2 Motor Control

Several brushless motor controllers were used throughout the development of the diagnostic. The current load when spinning up the chopper can be as high as $\sim$10 A, which exceeds the capabilities of some controllers and causes them to get hot and/or fry components. For this reason, a fan is installed on the present controller which is a Castle Creations Thunderbird-18. This controller is capable of 18 A continuous current, and 20 V max on the supply.

Since radio controlled airplanes are, in fact, "radio controlled" they have a receiver that converts the radio signal into an electrical signal which goes to the controller telling it how fast to spin. The receiver does this by sending a pulse-width modulated (PWM) square pulse to the controller. The pulse is repeated at 50 Hz and the duty cycle varies from 0.05 to 0.1, corresponding to no rotation and the fastest rotation, respectively. The PWM circuit (called the "pulser") used is shown in Fig. 4.6. Connecting the pulser to the ESC is accomplished by using only the orange (signal) wire and the brown (reference) wire, as shown in Fig. 4.7. The $\sim$24 AWG red wire on the ESC is a 5 V output and not used in this application. The three wires leading from the ESC to the motor can be connected in any arrangement, and reversal of the motor rotation direction is accomplished by switching any two motor wires.

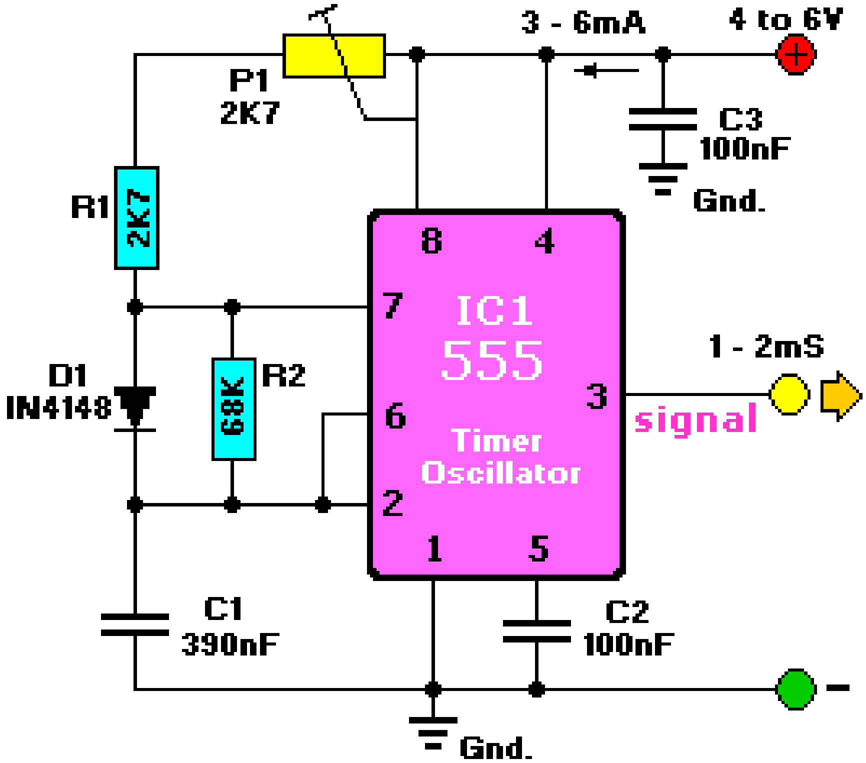

Figure 4.6: Motor controller.[44]

4.4.3 Motor Diagnostics

There are several things that must be measured to ensure proper operation of the motor. These include:

- Motor temperature - Neodymium magnets will suffer permanent damage if the temperature rises above $\sim 90°$C.
- Motor current - The motor controller used can only safely supply 18 A without damage to the MOSFETs.
- Motor voltage - The motor controller can only handle a maximum voltage of 20 V.

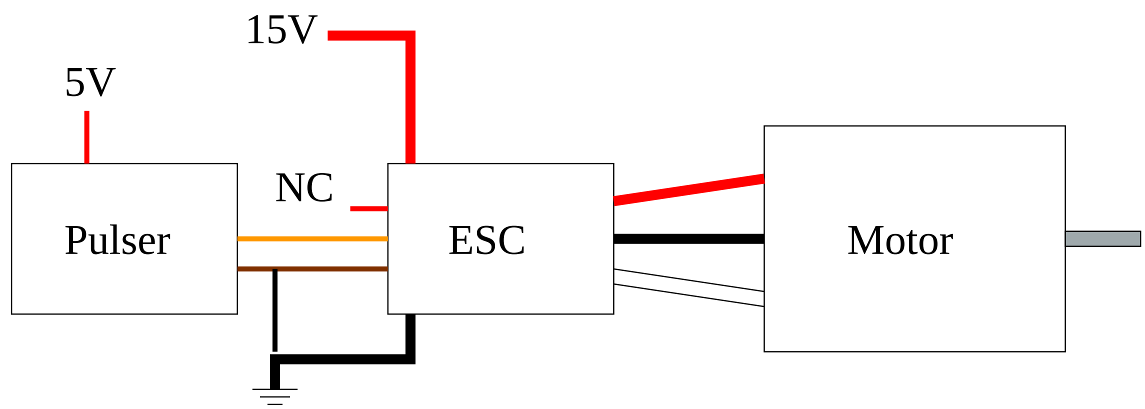

Figure 4.7: ESC Implementation

- Rotation frequency - This determines the chopping frequency and must be accurately known to allow synchronization with the plasma discharge.

The temperature was monitored by a thermistor attached to the motor, with an electrical feedthrough on the vacuum vessel. At the typical running speed of 10,000 RPM, the motor reaches thermal equilibrium at a temperature of 38°C.

The motor voltage is measured by a DPM-35 Digital Panel Meter from Martel Electronics Corporation. Increasing the supply voltage provides more current that can be sourced by the controller, which in turn corresponds to a higher rotation frequency. The current is measured by the ESC power supply, which is a Power/Mate Corp. regulated power supply capable of 60 V, 20 A DC. Frequency measurement involves passing light through the chopper, so it is discussed after the chopper.

A metal control box located near the high voltage power supplies is shown in Fig. 4.8. The PWM circuit is inside with a knob connected to variable resistor for controlling the disk rotation frequency. The two red meters shown do not work. Instead, the two banana plug jacks are connected to the thermistor for temperature measurements, and the rotation frequency is measured using an oscilloscope as described later.

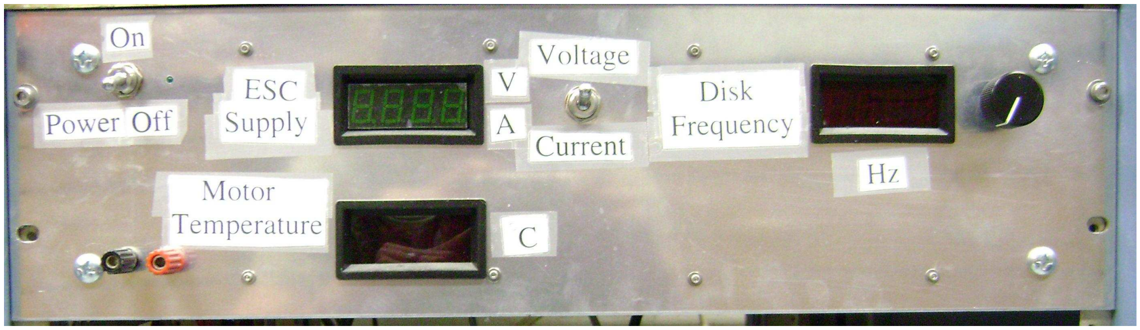

Figure 4.8: Time-of-flight diagnostic control panel.

4.5 Chopper

The chopper has evolved through several generations throughout the development of the time-of-flight diagnostic. They are all made of 0.005" thick stainless steel with 13 cm radii, which has a mass of 30 g each. The first two versions have 160 slits while the third has 80. A 3.2 mm thick G-10 support attached using cyanoacrylate, shown in Fig. 4.9, was originally intended to provide mechanical stability to the chopper and allow a more secure attachment to the motor shaft by being able to tighten the collet without damaging the disk. As explained below, the first version resulted in catastrophe, so a thinner support (1.6 mm) extending only 6cm was used as a replacement. This version works fine, aside from having too many slits, as it was later determined. The final version has 80 slits and no G-10 support, and there is no problem with attachment to the motor provided that extreme care is taken during the process.

4.5.1 Disk Balancing

For any system that implements a rapidly rotating object, it is extremely important to make sure that the object in question is properly balanced. There are two types of balancing that can be performed: static, and dynamic. When an object is statically balanced, its center of mass is along the axis of rotation. Dynamic balancing is demonstrated when the object can rotate without wobbling.

Static balancing of the chopper is performed by placing the disk on an axis which rests on an arrangement of knife-edged disks that are free to rotate with minimal friction as in Fig. 4.9. The device shown is a Dubro Tru-Spin Prop Balancer, which

Figure 4.9: Chopper balancing set-up.

is designed for balancing model airplane propellers but also works quite well for the chopper. If there is an imbalance of mass between opposite sides of the disk, the heavy side will rotate to the bottom. Removing some of the mass from the heavy side, by drilling out some of the material, brings the disk closer to a balanced state, and the process is repeated. An estimate of how much mass to remove can be obtained by attaching a known mass to the lighter side. When the disk is positioned at any angle without rotating, as in Fig. 4.10, is it statically balanced.

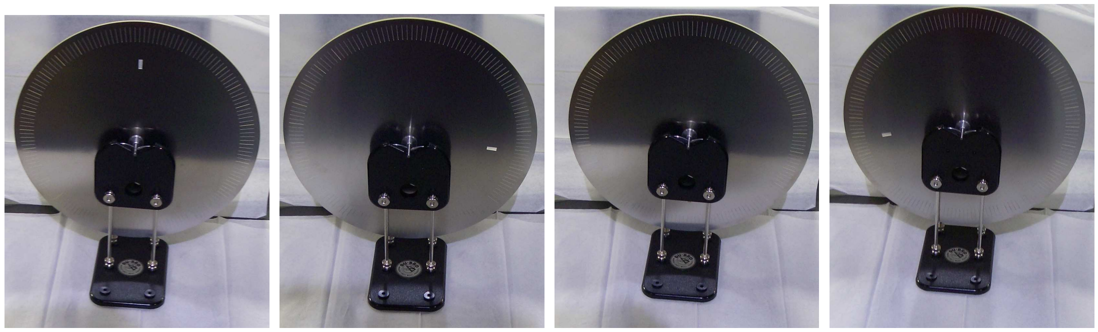

Figure 4.10: Balanced disk.

4.5.2 Chopper Attachment to Motor

Since the motor shaft itself does not have a mechanism for attaching anything to it, an additional piece was necessary. For model airplanes, there exist two types of propeller adapters that are used for motor attachment. One type implements a set screw on one side and is not axially symmetric. The other uses a collet to clamp onto the motor shaft from three sides. The latter, being axially symmetric, was the desired choice to eliminate any possible imbalance.

Using the frequency measurement method described in Section 4.5.3, a high speed test was performed to see if the chopper could spin up to 30,000 RPM. This test used the first chopper/support design shown in Figure 4.9, and ultimately resulted in catastrophe near 20,000 RPM. Upon investigation, the aluminum collet attachment broke causing the chopper to fly off and break apart on impact with the vacuum vessel. Two improvements were implemented after this test:

1. A new collet was custom machined out of stainless steel
2. A smaller, thinner chopper support was introduced

Although the collet shattering was the result of excessive vibration due to imbalance, the fact that it occurred at all was a surprise. The stainless steel collet has not had any problems as of the writing of this thesis. As mentioned above, the second G-10 support is 1.6 mm thin with a radius of 6 cm.

4.5.3 Frequency Measurement

The rotation frequency of the disk must be precisely known for the reasons mentioned in Sec. 4.4.3. The chopping frequency, which determines the distance between the chopper and detector, is directly proportional to the rotation frequency. As demonstrated in Sec. 4.3, choosing a specific uncertainty, streaming distance, and chopping frequency requires a specific rotation frequency. In addition, the synchronization of the chopper with the system is heavily dependent upon a precisely known rotation frequency.

A laser diode (M650-5 from NVG, Inc.) is mounted inside the vacuum vessel on one side of the chopper and a photodiode is on the opposite side. They are arranged so that the laser light hits the photodiode after passing through the same slit that the neutrals pass through[1]. The photodiode is an OP906, chosen because of its fast ($\sim$5 ns) response time, whose signal is fed to a box directly connected to the vacuum electrical feedthrough. The circuit, shown in Figure 4.11, converts the photocurrent into a voltage through the 1.5 kΩ resistor. The signal is passed through a 100 ns low pass filter and amplified by $\sim$82 using an OPA657 operational amplifier, chosen for its large gain-bandwidth product (1600 MHz). Testing the amplifier with a gain of 166 (where amplified bandwidth was 9.6 MHz) results in rise-times of 104 ns, so dividing the gain in half gives rise times around 50 ns. The amplified signal was then converted into square pulses through the inverter with Schmitt trigger inputs. A Schmitt trigger has hysteresis in the threshold voltage in order to prevent noise alone

[1]Originally a separate timing slit was used, however it was discovered that repositioning the chopper disk by removing and re-attaching causes the timing calibration (discussed later) to be incorrect.

from switching the output. The resulting square pulses are used for both frequency measurement by looking at them on an oscilloscope, and synchronization with the plasma discharge.

4.5.4 Synchronization Using a Reference Laser

In order to control when the chopper slot first opens, t_{open}, relative to the plasma firing sequence, the delay circuit (Fig. 4.12) is used to synchronize the timing between the two. The D-Flip-Flop takes an initial trigger (the trigger from the operator firing the discharge) as a clock pulse input, which changes Q's output to 'high'. Then the circuit waits until the second input on the AND gate receives a reference timing signal. The AND gate triggers a series of transistors used to step up the voltage to 15 V in order to trigger the delay box, which then triggers the plasma discharge after a chosen delay. Then the delayed trigger is inverted and fed back to the D-Flip-Flop to reset the Q output to 'low', which resets the circuit until the operator fires again.

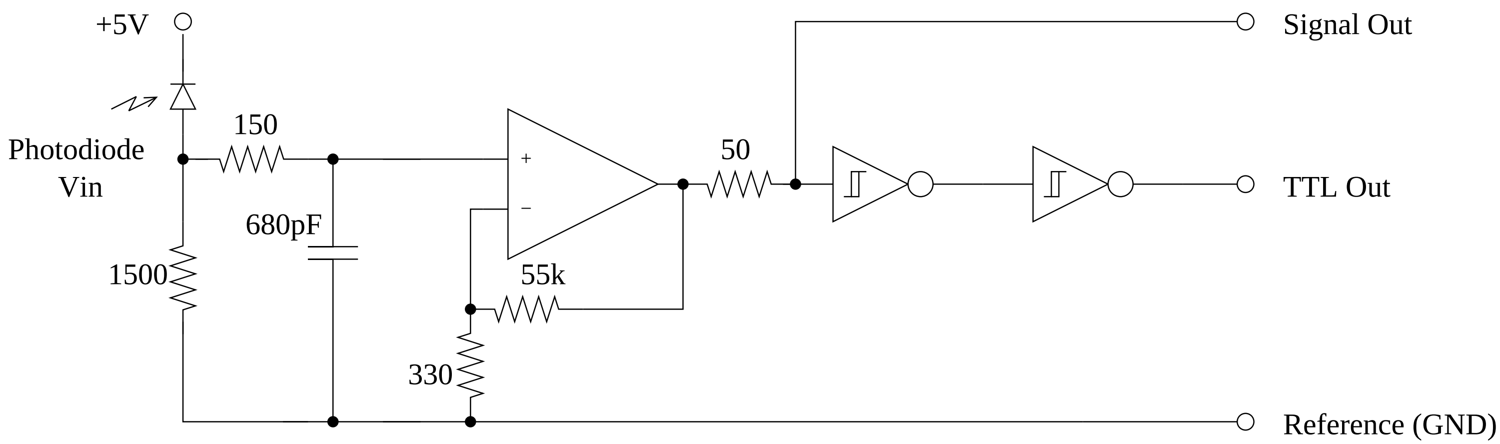

Figure 4.11: Photodiode pulse transmitter.

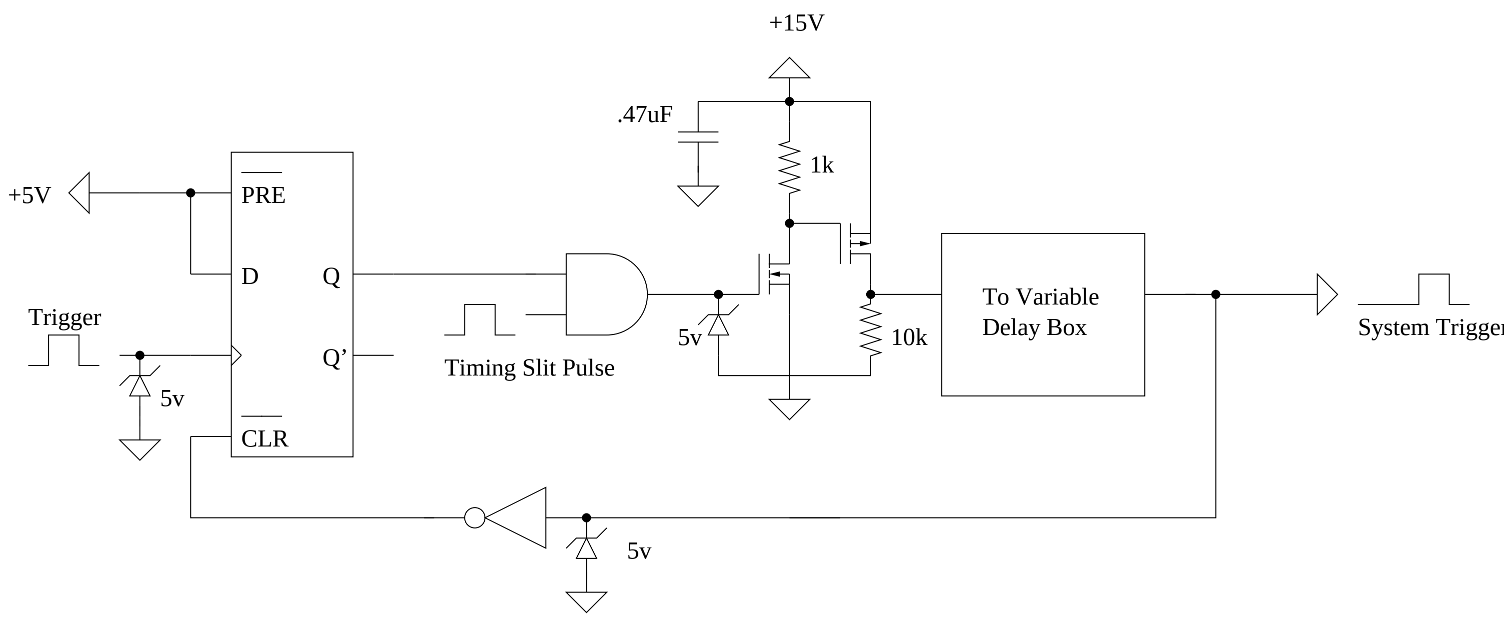

Figure 4.12: Synchronization Circuit.

4.6 Detector Implementation

The detector is installed at the end of a 1.5 m long tube. DC biasing is accomplished through the use of an UltraVolt -4 kV high voltage power supply. For noise reduction, the power supply has a Mu-metal/RF shielded case and an electronic line filter. The maximum voltage that can be applied to the Channeltron is -2.8 kV, with the detector entrance held negative for neutral particle measurements.

The collector output is fed into a 2 kΩ resistor and then buffered as shown in Fig. 4.13. The 2 kΩ resistor converts the secondary electron current into a voltage.

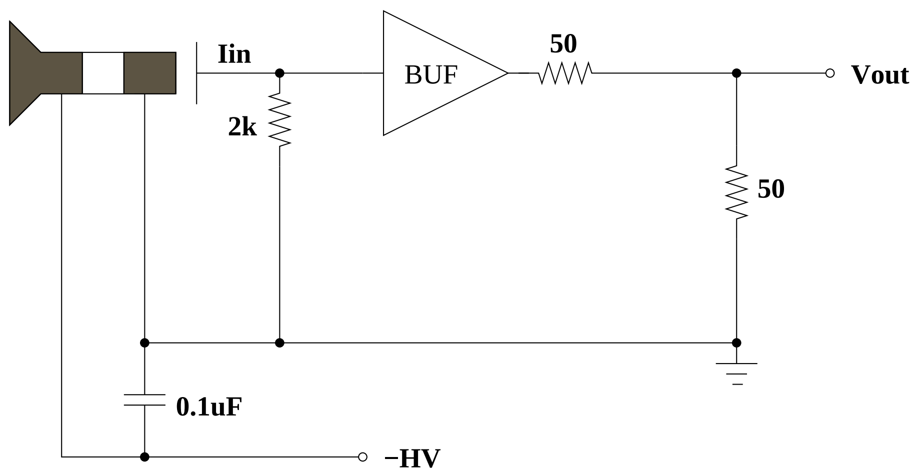

Figure 4.13: Channeltron collector signal collection electronics.

Although it is desirable to have a large signal, increasing the resistor results in a slower response time due to capacitance of the collector to ground. In the tests performed with the lithium source (described later), the collector capacitance to ground was found to be ∼26 pF by measuring the RC decay for different values of R. The 2 kΩ resistor provides a good balance between a small RC time (50 ns), and good signal level (50 mV).

The alignment of the detector, chopper, and collimator is accomplished by first replacing the detector and neutral particle input with glass windows. After pumping down with a mechanical pump to ensure that all the flanges are seated as they are under vacuum, an incandescent light bulb is used to see where the light hits the window at the detector. A transparency is used on top of the window to pinpoint the center and the chopped beam of light is observed by sight to line up with the center of the transparency. This verifies that there was a straight line of sight from the neutral particle input, through the aperture and collimator, and onto the detector.

4.7 Calibration using a Xenon Source

In order to perform the transformation from the time to velocity (and energy) domain, the time at which the chopper slits pass in front of the collimating slit must be calibrated. The reference laser can be used for this purpose provided that the delay between it and the detector signal is measured. Ultraviolet (UV) light can be used as a source since the Channeltron is sensitive to light with wavelengths shorter than ∼160 nm[45]. Channeltron detection efficiency as a function of wavelength is shown in Fig. 4.14. Although it was discovered that the IFRC plasma produces enough UV to be used as a timing reference, the diagnostic timing was also verified using a xenon lamp as a UV source, as described here.

A xenon discharge lamp was placed on the opposite side of the vacuum vessel as a UV light source. The emission spectra for a typical xenon lamp[46] is shown in Fig. 4.15. To maximize the amount of UV photons making it into the vacuum vessel, a sapphire window was installed whose transmission characteristics are shown in Fig. 4.16. Since the UV source emission falls below 1% around 200 nm, and the transmittance through the sapphire window is less than 10%, the incident flux in the vacuum UV range was expected to be very small. It was observed that, on

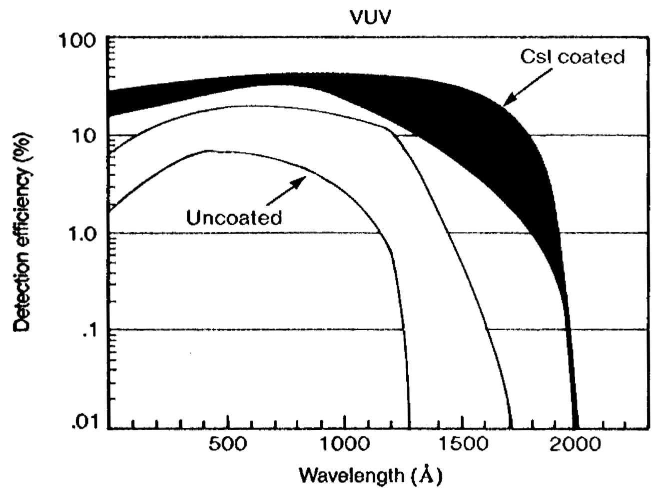

Figure 4.14: Photon detection efficiencies for Channeltron.[45]

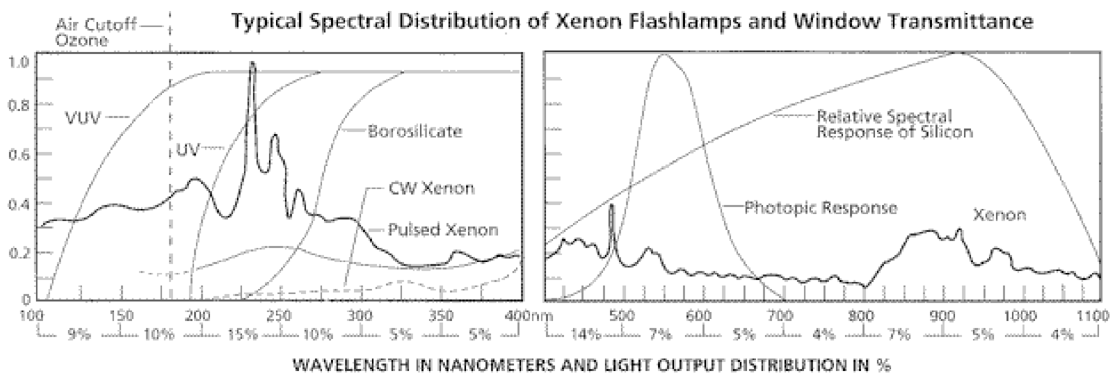

Figure 4.15: Typical xenon lamp full spectrum.

average, there were approximately five photons detected every second. Because of this extremely low count rate, signals were triggered off of the photon signal from the Channeltron amplifier circuit and the delay was measured between the photon peak and the reference laser signal.

To account for the finite open time of the chopper, an average of 128 photon triggers was performed using the oscilloscope's averaging feature on the reference laser signal. The expected signal, $F(t)$, was computed numerically by a convolution[48]

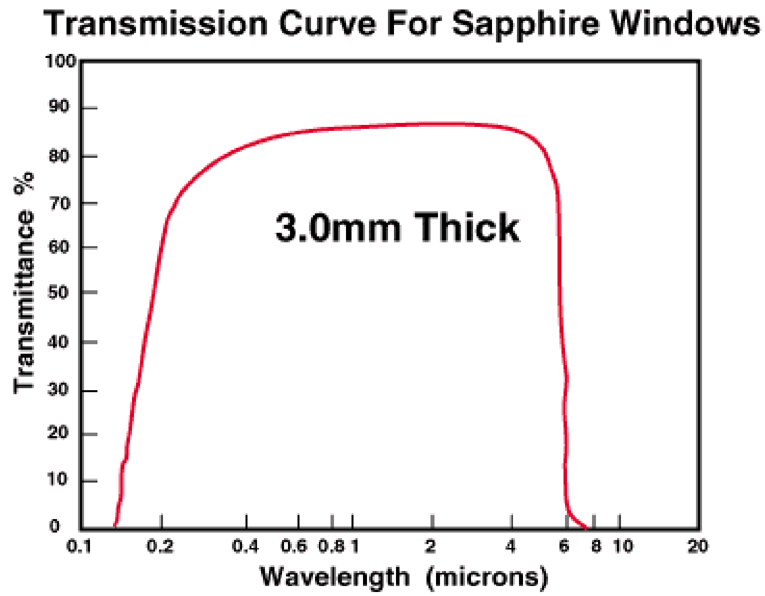

Figure 4.16: Sapphire window transmission curve[47].

$$F(t) = \int_{-\infty}^{\infty} d\tau f(\tau) A(t - \tau) \tag{4.8}$$

where $A(t)$ represents the cross-sectional area of the opened chopper slit as a function of time (Eq. 4.4) and $f(t)$ is the response of a single pulse from the reference laser.

An average of five shots, each shot an average of 128 photon triggers, was compared with the numerical convolution to confirm agreement. The time delay between the reference laser and detector signal was then measured to be 1.6 μs. An average of five shots, each shot an average of 128 photon triggers, is shown as the dotted trace in Figure 4.17b. The numerical convolution, shown as dashes, closely matches the shape of the measured average aside from a slight broadening. This shows the 1.6 μs time delay between the reference laser and detector signal as differences between when the peaks occur.

As shown in Chapter 6, UV light produced in the IFRC can be used as a timing reference. This calibration procedure verified that the observed large peaks ($>$ 10%

maximum signal) from the IFRC were due to UV light rather than fast neutrals. In experiments where there is no UV light produced, this procedure can be used prior to data collection in the absence of UV light for an absolute timing calibration.

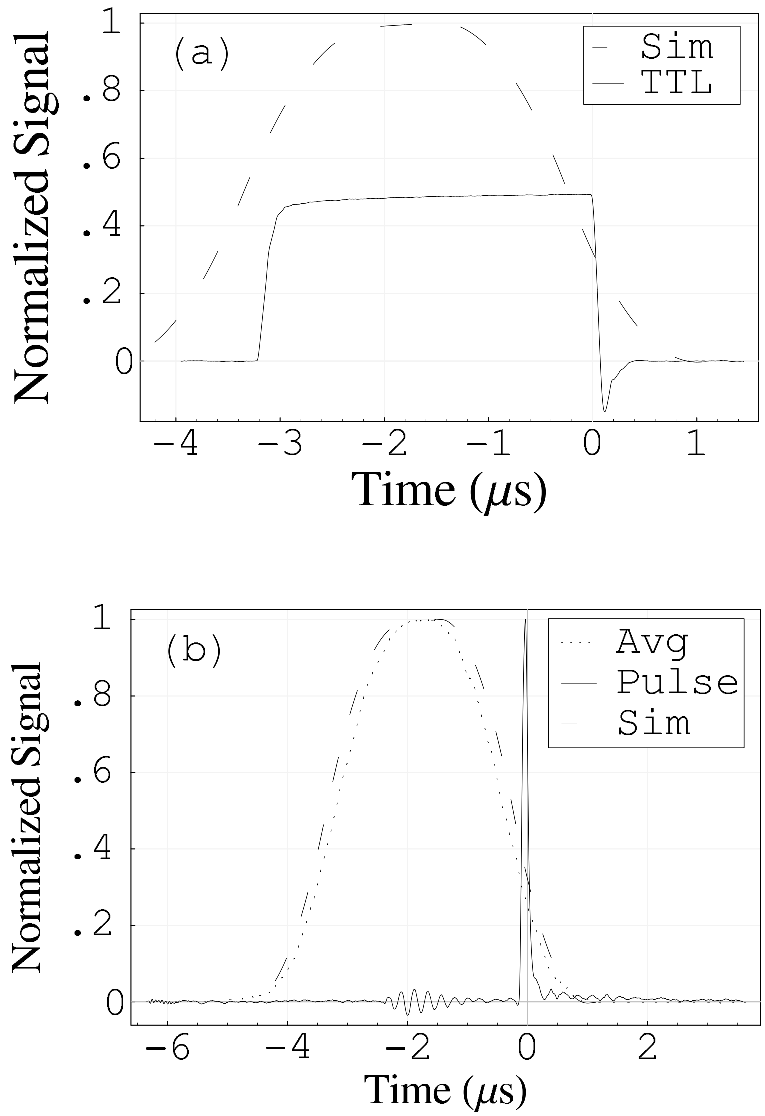

Figure 4.17: (a) Single TTL pulse from reference laser (solid) together with the expected pulse shape $F(t)$ (dashed) after convolution with a slit that is open for 2.5 μs. (b) Individual pulse from an UV photon (solid), average signal over five shots (dotted), where each shot is an average of 128 reference laser pulse cycles, and predicted average signal (dashed).

4.8 Calibration using a Lithium Ion Source

4.8.1 Energy Scan

An energy calibration of the TOF diagnostic was performed using a lithium ion beam [19]. An ion source with a tunable energy was used to verify that the TOF diagnostic measured the expected energies. The UV calibration method described in Sec. 4.7 could not be used as a timing reference for this test, since the ion source blocked the UV photon path. Using a 500 V emitter bias for the source, an energy of 460 eV (obtained from the ion source calibration[19]) was used to calculate the slot open time and an energy scan was performed.

The lithium source produces a beam current of 0.1-1 mA/cm^2, which corresponds to a maximum of 1.8×10^{15} ions/s. Taking into account the beam divergence of 3° and the flux reduction due to the slit geometry, the maximum expected ion rate was around 9 ions/μs. The measured unchopped ion rate was actually 3 ions/μs for an emitter bias of 600 V, meaning the count rate was low enough to detect individual particles.

The ion source bias voltage was varied over its entire range, 300 V to 1500 V, and five shots were taken for each bias as an energy scan. Because of the low ion flux, only 1-5 ions were typically detected per 2.5 μs gate time. A sample shot is shown in Figure 4.18. For all data used in this section, the oscilloscope was triggered off of the TTL signal generated from the reference laser and the pulse times were all measured from the point at which the signal was 5% of the maximum on the leading edge.

For the data shown in Figure 4.19, the delay between the reference laser and the average pulse position, Δt_{total}, was measured for a 500 V emitter bias on the ion source. The delay between the slot open time and the reference laser signal, Δt_{ref},

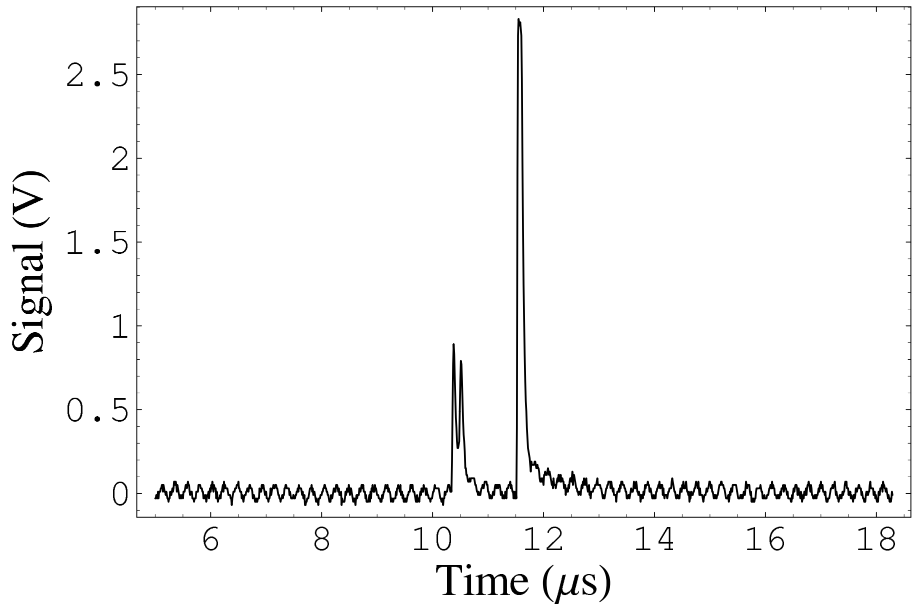

Figure 4.18: Shot 2300 - Pulses from lithium ion source. Emitter Bias 800 V, Chop Frequency 26 kHz. Two neutrals are observed near 10.5 μs and one at 11.5 μs. The amplitude differences are attributed to the pulse height distribution[45].

was then calculated using an average ion energy of 460 eV.

$$\Delta t_{ref} = \Delta t_{total} - \Delta t_{460} \tag{4.9}$$

where Δt_{460} is the travel time for a 460 eV Li ion, which is 14.2 μs for a 1.6 m distance. Δt_{ref} was then used to calculate the slot open time for various ion energies as the emitter bias was scanned. The standard deviation of the 500 V bias data was 1.06 μs and can be attributed to the finite slit open time. Error bars in Figure 4.19 were calculated by the deviation from the mean at each bias voltage. As shown, the fitted line of the averaged data differs from the expected energies by 16%.

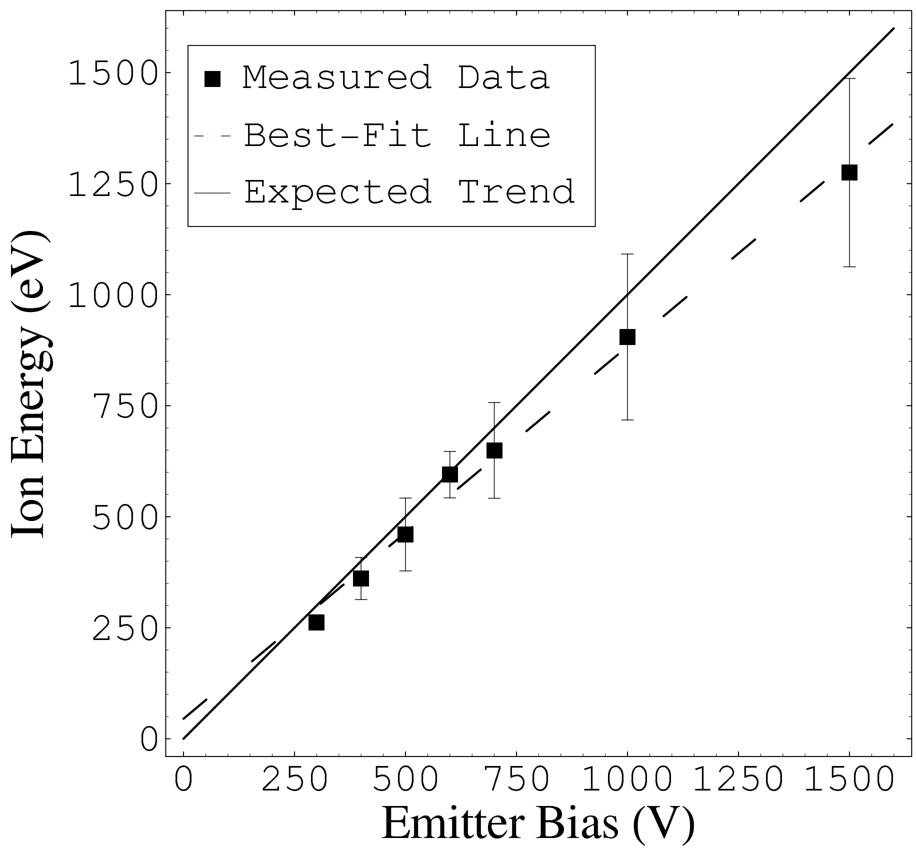

Figure 4.19: Lithium ion energy scan. Expected trend (solid) represents a 1:1 correspondence between ion energy and emitter bias. Best-fit line (dashed) falls within error bars.

4.8.2 Lithium Energy Distribution Function

To determine the distribution function, 650 pulses were sampled at an 800 V emitter bias and binned according to the time difference between the reference laser and the arrival time as shown in Figure 4.20. The flux from a drifting Maxwell-Boltzmann distribution with a peak energy of 750 eV and temperature of 83 eV (computed by a least-squares fit) is shown in addition to data taken from a biased planar collector [19]. The Maxwell-Boltzmann distribution and the collector data have both been

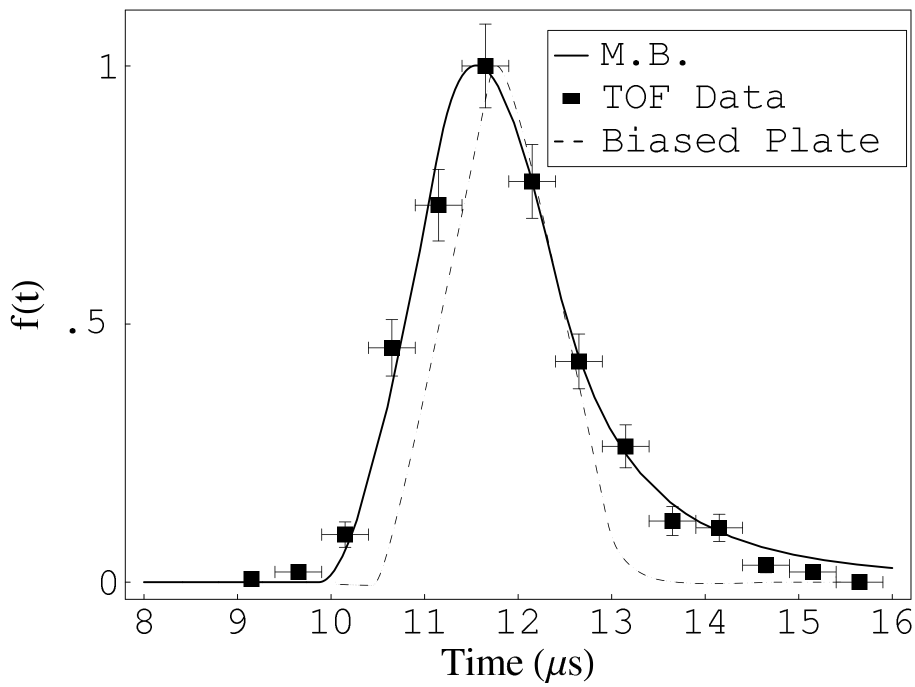

Figure 4.20: Lithium ion distribution function for 800 V bias in time domain as measured by TOF diagnostic (boxes) where data are binned into 500 ns intervals. Maxwell-Boltzmann distribution comparison (solid) with 83 eV temperature and 750 eV drift convoluted with the aperture function and compared with convoluted biased plate collector data (dashed) from the ion beam calibration[19].

transformed to the time-domain and convoluted with the aperture function, Equation 4.4, in order to compare with the TOF data. Since the data consist of a finite number of points, the convolution performed was a discretized form of Equation 4.8.

The emitter temperature in the ion source is typically 1100°C, or 0.1 eV. Since the TOF data shows a broadening of 83 eV at a 750 eV beam energy, the resulting uncertainty, $\Delta E/E$, is 0.11. The theoretical uncertainty, $\Delta E/E$, is 0.09 and is computed by Eq. 4.5.

4.9 IFRC Data Correction

The process by which the signal from the detector is converted into an energy distribution function is described in this section. First, the data is transformed from the time domain into velocity space by the replacement

$$f(t) \rightarrow f\left(\frac{L}{t - t_0}\right) \tag{4.10}$$

where L is the flight distance and t_0 is the open time of the slit. The velocity, v, is then converted into its corresponding energy for a hydrogen atom.

The data must also be corrected for detector sensitivity and charge-exchange cross-sectional dependence on particle energy. For atomic hydrogen, the charge-exchange cross-section is empirically[43]

$$\sigma(E) = (7.6 \times 10^{-8} - 1.06 \times 10^{-8} \log_{10} E)^2 \mathrm{cm}^2. \tag{4.11}$$

Absolute detection efficiency has been performed down to 20 eV and is approximated by[40]

$$\eta(E) = 1.1 \times 10^{-3} E - 1.1 \times 10^{-2}. \tag{4.12}$$

The data correction is accomplished through the transformation

$$f(E) \rightarrow \frac{f(E)}{\sigma(E)v(E)\eta(E)} \tag{4.13}$$

and is used for the data presented in Chapter 6.

Chapter 5

Visible Emission Spectroscopy

5.1 Light Emission from a Plasma

Plasmas emit electromagnetic radiation as a result of several distinct processes. The acceleration of charged particles by cyclotron motion and bremsstrahlung are commonly observed sources of radiation from electrons[25]. Radiation from atoms and ions within the plasma that occur when electrons transition from a higher to lower energy state can provide information about the ions, such as drift velocity and temperature. In IFRC, visible light from hydrogen and carbon (plasma source products) as well as helium, argon, and krypton (impurities) has been analyzed using a spectrometer in order to obtain drift velocities and temperatures. The impurities are introduced by filling a plenum attached to the plasma vessel by a needle valve, and opening the valve until background pressures resulting in measurable emission lines ($>$ 20 mV) are reached. Table 5.1 summarizes the observed lines.

Some basic information about important considerations when designing a spectrometer system is described in Sec. 5.2. An overall description of the spectrometer

Species	H	He	C	Ar	Kr
Ionization	I	I	II	II	II
Transition	$2p$ - $3d$	$1s2p$ - $1s3d$	$2s^2 3s$ - $2s^2 3p$	$3s^2 3p^4 4s$ - $3s^2 3p^4 4p$	$4s^2 4p^4 5s$ - $4s^2 4p^4 5p$
Wavelength (Å)	6562.85	5875.62	6578.05	4879.86	5681.90
Fill Pressure (Torr)	-	1.1E-4	-	1.6E-5	1.3E-5

Table 5.1: Lines analyzed

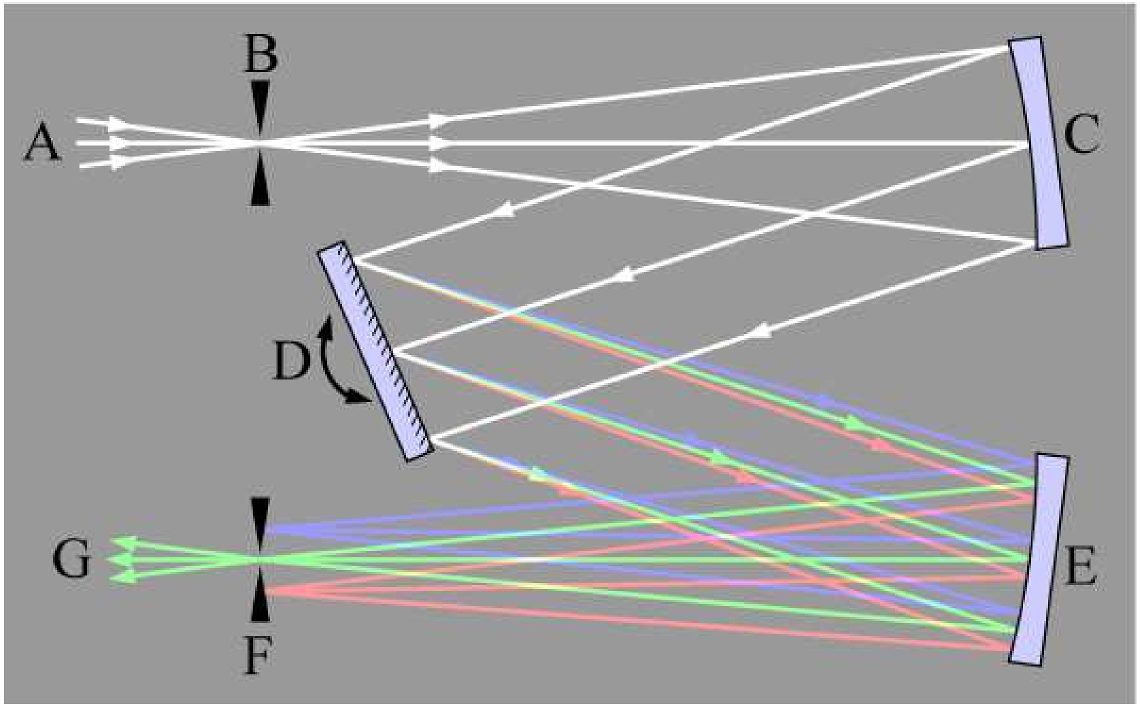

Figure 5.1: Czerny-Turner monochromator[49].

used at IFRC is covered in Sec. 5.3 along with the details of the optics and calibration. The procedure used for performing the Gaussian fits for data analysis is discussed in Sec. 5.4. Section 5.5 covers the sources of broadening that must be considered.

5.2 Spectroscopy Basics

The spectrometer used in IFRC is a modified Czerny-Turner monochromator described in the next section. A Czerny-Turner configuration requires two concave mirrors whose focal lengths are equivalent to the distance from the mirrors to the entrance and exit slits, as shown in Fig. 5.1. When an object is focused onto the entrance slit (B), the mirror (C) collimates the light so that the rays incident on diffraction grating (D) are all parallel. The light rays incident on mirror (E) are dispersed according to the angle of the diffraction grating and its groove density. A

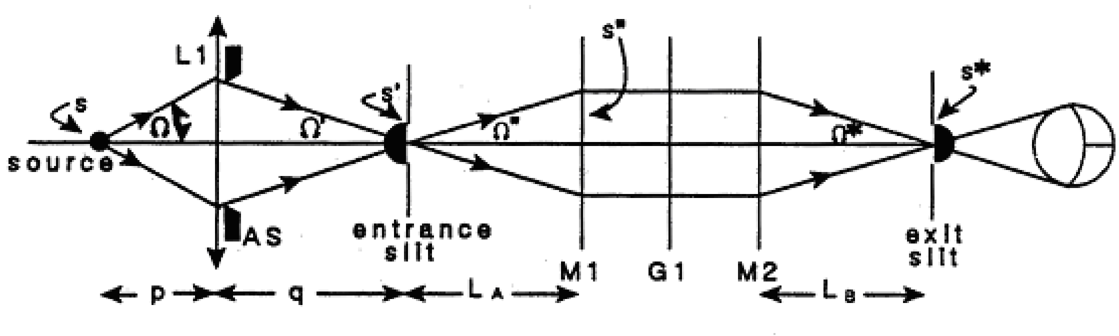

Figure 5.2: Etendue matching in an optical system.[50].

narrow range of wavelengths is focused onto the exit slit (F) by the mirror (E).

Maximization of the monochromator throughput (ratio of output light to input light) is accomplished by matching the etendue at each optical element (lens or mirror). Etendue can be interpreted as the maximum beam size the instrument can accept, and is characterized by

$$G = \pi S \sin^2(\Omega) \tag{5.1}$$

where S is the cross-sectional area of the source and Ω is the half-angle of the maximum cone of light that can enter the optical element[50]. Matching of the etendue is demonstrated in Fig. 5.2 and is accomplished when

$$G = \pi S \sin^2(\Omega) = \pi S' \sin^2(\Omega') = \pi S'' \sin^2(\Omega'') = \pi S^* \sin^2(\Omega^*). \tag{5.2}$$

The sizes and focal lengths of optical elements should be chosen so that G in Eq. 5.1 is as large as possible.

Referring back to Fig. 5.1, in order to maximize the amount of light collected by the mirror (C) the angle Ω, which is equivalent to $\arctan(C/2\overline{BC})$, must satisfy

$$\tan \Omega = \frac{C}{2\overline{BC}} \geq \frac{D}{2f} \tag{5.3}$$

where D and f are the size and focal length of the input lens. The terms on either side of the inequality are the numerical apertures of the optical elements. The quantity f/D, called the f-number, is a common number used to describe lenses. Equation 5.3 can be expressed in terms of the f-numbers by saying that the f-number of the input optical element must be greater than or equal to the f-number of the output. For optical systems with many components, this translates into saying that each successive optical element must have an f-number less than or equal to the previous one.

The modification employed by the IFRC spectrometer is that the exit slit is opened wide to allow a large range of wavelengths (passband) to pass through. The passband depends on the exit slit width, and the linear dispersion of the spectrometer. Linear dispersion $d\lambda/dx$ quantifies how much of a spectral interval is spread over the focal plane of a spectrometer[50]:

$$\frac{d\lambda}{dx} = \frac{10^6 \cos \beta}{knL_B} \text{nm/mm} \tag{5.4}$$

where k is the diffraction order, n is the groove density, β is the angle of diffraction, and L_B is the exit focal length. Measuring β at a wavelength of 656 nm gives a linear dispersion of 0.66 nm/mm. This is comparable to the manufacturer's quoted dispersion of 0.7 nm/mm. Discrepancy is due to the difficulty in measuring β because of limited access to the diffraction grating.

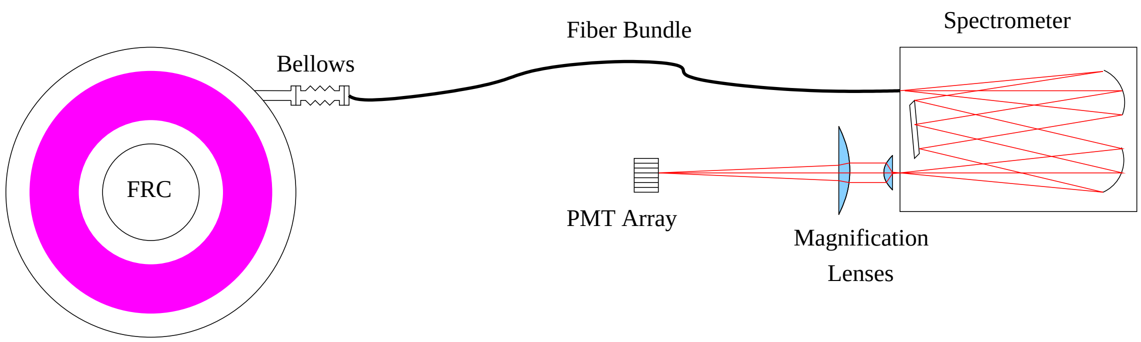

Figure 5.3: Spectroscopy on IFRC

5.3 Spectrometer Setup

In IFRC, a SPEX 1702 Czerny-Turner spectrometer has been implemented along with a Hamamatsu R5900U-20-L16 photomultiplier tube (PMT) array as a detector. With a 0.75 m focal length, and a grating with 1800 grooves/mm, the specified resolution is 0.15 Å for an entrance slit width of 10 μm. The general setup is shown in Fig. 5.3.

The spectrometer itself has been upgraded to allow remote control through a personal computer running LabView. The stepper motor was replaced by a 23M50 (from MicroKinetics Corp.) capable of 200 half-steps per revolution and the motor driver by a UnoDrive (also from MicroKinetics). For compactness, the controller is mounted inside of the spectrometer and is powered by a 24 V DC wall transformer that plugs into the side. The controller is interfaced with the computer through a NI USB-6008 multifunction I/O data acquisition card from National Instruments. The USB connection allows easy installation to any computer that is running LabView software.

An additional change was made in order to accommodate the 6.4 mm focal length of the lens directly outside of the exit slit. As described later, the exit slit must be at the focal length of the lens. This was not possible with the screws that were previously used to attach the exit slits to the monochromator- the screw head was 2.7 mm and the washer was 0.6 mm thick. The screws are replaced with ones with a much lower profile (1.5 mm), and the stainless steel washers with thinner plastic ones (0.1 mm). Replacement of these components allows the lens to be placed at the appropriate distance from the exit slit.

5.3.1 Entrance Optics

The emitted light from the plasma is coupled to a fiber bundle using a fiber optic collimator that sits 8 cm behind a 15 cm long 1 cm diameter tube which restricts the view of the plasma to improve spatial resolution. The projection of the fiber collimator onto the plasma at the minimum intersecting chord is a circle with a 2.5 cm radius. With this arrangement, there is adequate light detected and modest spatial resolution.

The fiber collimator has an SMA connector for a fiber optic cable, and is designed so that the distance from the tip of the fiber to the collimating lens is equal to the focal length of the lens. In IFRC, a bundle of $\sim$150 μm diameter fibers is used to carry the light from the plasma vessel to the spectrometer. The fiber bundle (Fig. 5.4) consists of $\sim$100 fibers arranged in a filled circle with a 1.5 mm diameter at one end, and a straight line segment at the other.

Originally, a single fiber was used (Fig. 5.5a) but this did not provide enough throughput for the narrow slit widths required for high wavelength resolution. Replacing the single fiber with the fiber bundle as in Fig. 5.5b increased the throughput by a factor of three. The linear segment of fibers is mounted with two translation stages and two rotation stages so that the positioning can be adjusted in order to

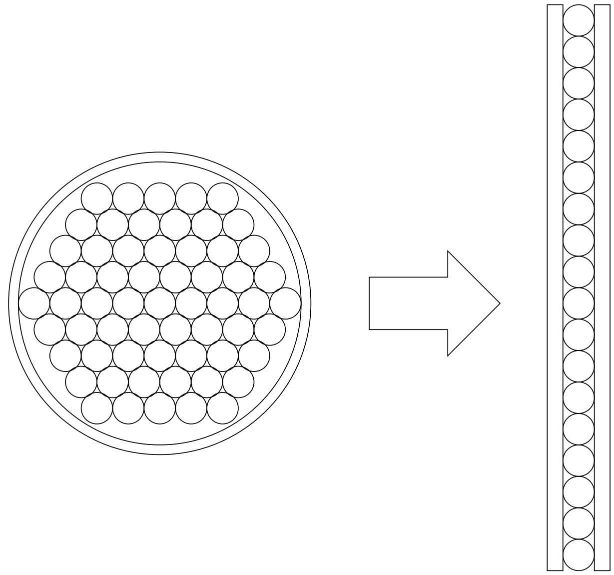

Figure 5.4: Fiber bundle going from a circular input surface to a linear output surface.

maximize the amount of light going into the spectrometer. If necessary in the future, a two lens setup like Fig. 5.5a can be used in conjunction with the fiber bundle if more light is needed.

5.3.2 Exit Optics

As mentioned in Sec. 5.2, the linear dispersion for the spectrometer is 7 Å/mm. The width of the exit slit is determined by the passband required to perform the desired measurements. Since both Doppler broadening and Doppler shifting of lines are of interest, the design takes both of these into consideration.

Expected hydrogen temperatures are in the range of 10 eV, which corresponds to a Doppler broadening of 0.69 Å at the H_α line (6562.8 Å). For measuring multiple wavelengths at the same time, the exit slit of the spectrometer is opened 680 μm. Multiplying this by the linear dispersion gives a passband of 4.8 Å, which is adequate for the expected broadened profile. As determined by the time-of-flight diagnostic in

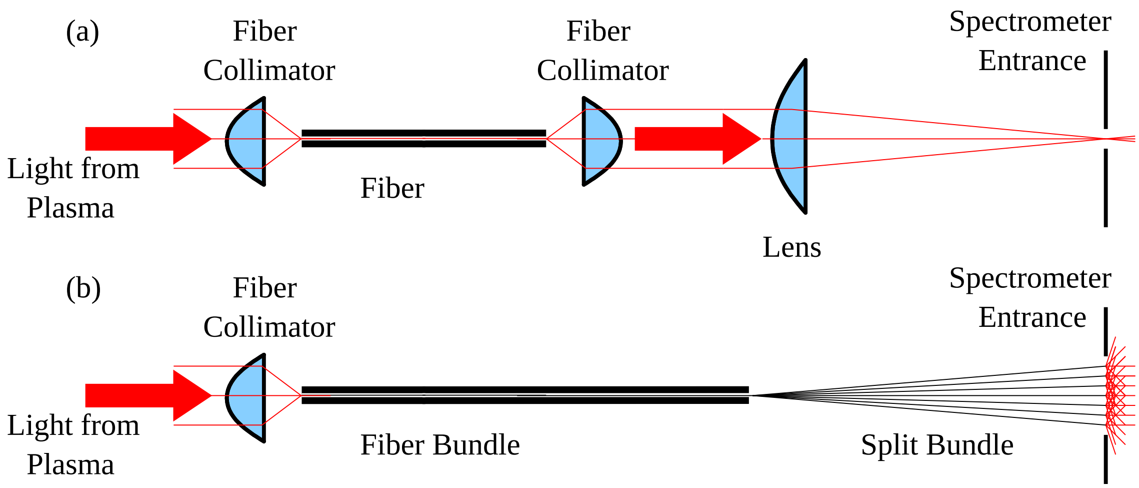

Figure 5.5: Spectrometer entrance optics. (a) Single fiber with entrance optics to improve light throughput. (b) Fiber bundle, without lenses results in more light at output of spectrometer.

Chapter 6, the average ion drift is less than 20 eV. For drifts of 1 eV and 20 eV, the Doppler shifts of the H_α line are 0.3 Å and 1.4 Å, respectively. The channel spacing, obtained by dividing the passband by the total number of channels, is 0.3 Å. This was tested using the He-Ne laser as described in the following section and scanning the diffraction grating over λ so the peak signal from the laser could be measured on different channels, giving 0.42 Å between channels. Discrepancy is likely due to additional dispersion introduced by the magnification lenses. Doppler shifts between 1 eV and 20 eV and temperatures around 10 eV are all measureable with the setup as described.

The PMT array has a total width of 16 mm, so the exit slit is magnified by a factor of 23. The lenses used for the magnification are plano-convex BK-7 precision cylindrical lenses from Newport Corporation. Cylindrical lenses are used since magnification is only required along the axis of the width of the slit (as opposed to the height). A 6.4 mm focal length lens is placed so that the focal plane of the spectrometer is at the focal point of the lens. A 150 mm focal length lens is placed behind

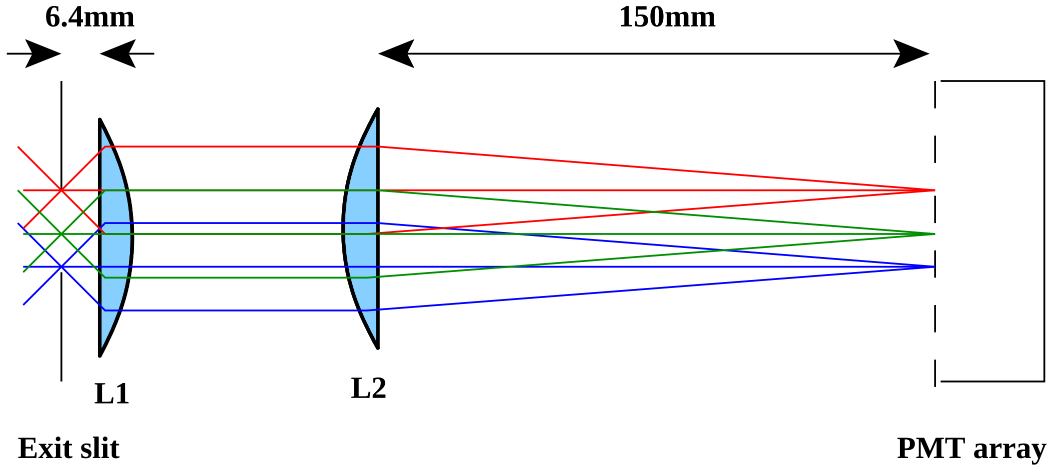

Figure 5.6: Optical setup for magnifying the exit slit onto the PMT array.

the other lens, so that the PMT array is at the focal point of the 150 mm lens. The optical setup is shown in Fig. 5.6. Rotation and translation stages are used for fine adjustments described below.

5.3.3 Lens Alignment

The lens system at the output of the spectrometer must be properly aligned in order to minimize the instrumental broadening. This is accomplished by aiming a He-Ne laser through the entrance of the spectrometer. Alignment of the laser with the spectrometer was ensured by centering the beam on the center of the input collection mirror. After rotating the diffraction grating so that the beam spot was centered on the exit slit, the first lens was centered horizontally by making sure the imaged beam spot was symmetric using the PMT array. The alignment of the lens along the optical axis was accomplished by maximizing the signal on the center PMT channel. The second lens was installed after the first was aligned, and the procedure was repeated for the new lens.

5.3.4 Calibration

Calibration of the diagnostic is accomplished using a hydrogen lamp. The H_α, H_β, and H_γ lines are all observable in the present setup and are used for establishing a reference from which other lines can be found. Once a known line is found by centering the peak on one of the PMT channels, a new line is found by stepping the spectrometer to the desired location.

The spectrometer is dialed by selecting the number of steps to increase in the software. Each step corresponds to 0.02 Å on the spectrometer's built in dial. An important consideration, however, is an additional (multiplicative) factor equal to 1.49921[1] that must be included in order to arrive at the correct wavelength. The correction factor works as follows: suppose the spectrometer is dialed to H_β, which is located at 4861.33 Å. The H_α (6562.81 Å) line, located 1701.48 Å away from the present line, is

$$1701.48\text{Å} \times \frac{1}{0.02\text{Å}} \times \frac{1}{1.49921} = 56746$$

total steps away.

This method has proved to be fairly accurate- typically resulting in errors of at most 1 channel or 0.4 Å. Further verification of where the central line is obtained by looking at the Doppler shift in both directions (co- and counter-current) and taking the average.

[1] The precision here is necessary because over a 2000 Å range, the number of (uncorrected) steps is 100000.

5.4 Gaussian Fitting

For a standard shot, time series data are recorded on 12 Tektronix oscilloscope channels. The analysis of these data involves first binning the data from each oscilloscope channel into 1 μs wide bins for smoothing purposes. The data are then converted from a voltage $V_i(t)$ to a number of photons $N_i(t)$ by first finding the number of photons N_i detected in each bin. Here i denotes the oscilloscope channel, each corresponding to a unique wavelength. During a time interval $[t_0, t_f]$, N_i is

$$N_i = \frac{\int_{t_0}^{t_f} \frac{V_i(t)}{R} dt}{\int_{t_0}^{t_f} \frac{V_p(t)}{R} dt} \tag{5.5}$$

where $V_p(t)$ is the voltage signal from a single photon pulse, and R is the impedance of the oscilloscope. The integral in the denominator is calculated (from a measured single photon pulse) to be 120 ns·mV/Ω. For each time bin, N_i is calculated and $N_i(t)$ is the result of converting all bins into number of photons.

After the signal is converted to $N_i(t)$, a least-squares Gaussian fit is performed over the 12 channels using an IDL routine called MPFIT[51]. The errors used for the weights for each wavelength bin are $\sqrt{N_i(t)}$. From the Gaussian fit, the average channel number A_0 and channel spread S_0 are found. The channel spread is multiplied by the channel spacing to get the wavelength spread

$$\Delta\lambda = 0.42 \times S_0(\text{Å}). \tag{5.6}$$

This wavelength spread is converted into a temperature after correcting for other sources of broadening described in the next section.

The Doppler shift $\Delta\lambda_D$ is the shift in wavelength from emission with an average drift velocity of zero. This is obtained from A_0 and is equivalent to

$$\Delta\lambda_D = 0.42 \times (A_0 - A_0')(\text{Å}) \tag{5.7}$$

where A_0' is the channel number corresponding with the unshifted wavelength λ_0. The resulting drift v is related to the Doppler shift by

$$v = c\left(\frac{\lambda_0 + \Delta\lambda_D}{\lambda_0} - 1\right) \tag{5.8}$$

where c is the speed of light in vacuum.

A sample spectrum from a standard IFRC shot looking at the H_α line is shown in Fig. 5.7 along with its corresponding Gaussian fit. Error bars for temperature and drift velocity measurements (Chapters 6&7) are obtained from the statistical deviation of the resulting Gaussian fit parameters between multiple shots.

5.5 Sources of Broadening

Assuming a Gaussian line profile, the resolution of an optical system is determined by the different contributions of line broadening added in quadrature. For a spectrometer, typical sources of line broadening occur from diffraction, $d\lambda_{diffraction}$, and the finite entrance and exit slit widths, $d\lambda_{slits}$. Additionally, the line width being observed, $d\lambda_{line}$, must be taken into account giving a resolution of

$$FWHM = \sqrt{d\lambda^2_{diffraction} + d\lambda^2_{slits} + d\lambda^2_{line}}. \tag{5.9}$$

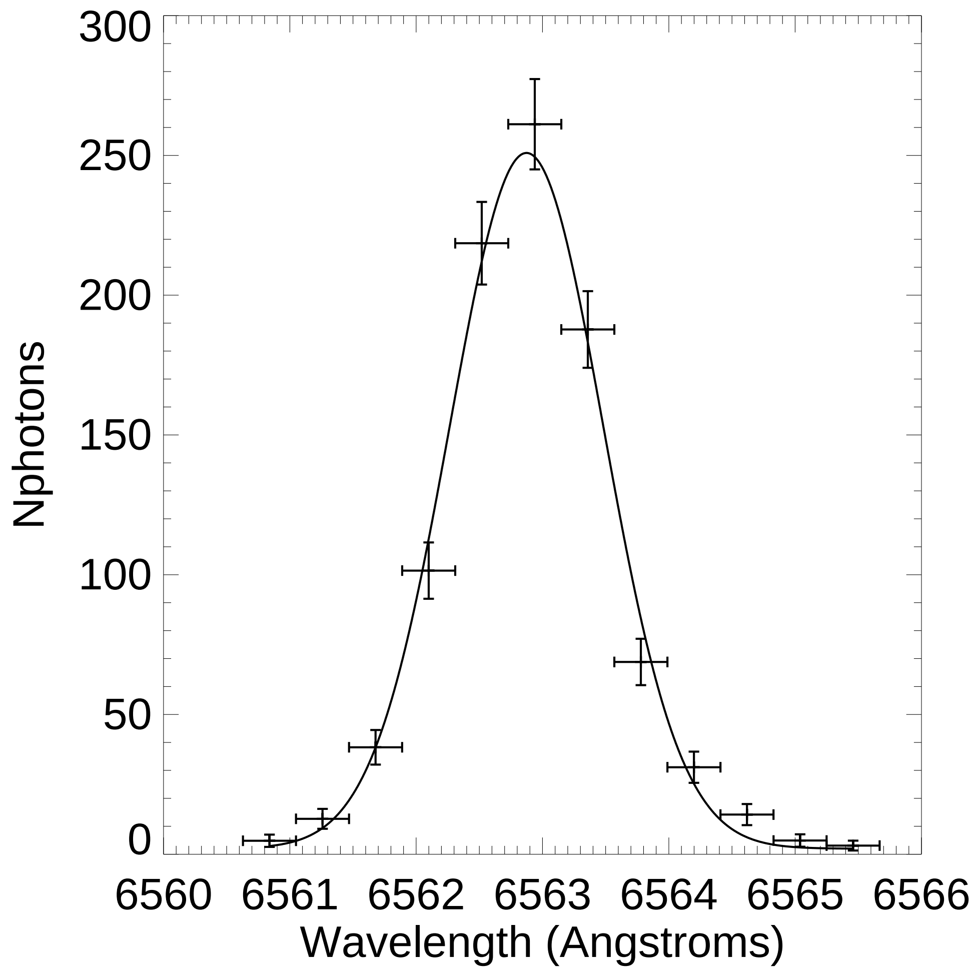

Figure 5.7: Gaussian fit performed over an average of five shots looking at H_α at $t = 60$ μs. Here, $\Delta\lambda = 0.6$ Å and $\lambda_0 = 6562.9$ Å.

The effect of the slits is approximated by

$$d\lambda_{slits} \approx \frac{d\lambda}{dx} \times w \tag{5.10}$$

where $d\lambda/dx$ is the linear dispersion as described previously, and w is the slit width. The line broadening due to diffraction $d\lambda_{diffraction}$ is calculated to be 0.05 Å by considering the theoretical resolving power, R, which is related to $d\lambda$ by

$$R = \frac{\lambda}{d\lambda} = kN \tag{5.11}$$

where k is the diffraction order (1 for this spectrometer arrangement) and N is the total number of grooves on the diffraction grating. As determined in the following section, the instrumental broadening is measured to be 0.30 Å indicating that the resolution is not limited by diffraction. Additional sources of broadening, like instrumental and Stark broadening, add in quadrature to obtain

$$d\lambda_{measured} = \sqrt{d\lambda^2_{instrumental} + d\lambda^2_{doppler} + d\lambda^2_{stark} + ...} \tag{5.12}$$

These sources are evaluated in the following sections.

5.5.1 Instrumental Broadening

Instrumental broadening is measured using a hydrogen lamp. The actual temperature of the lamp is 1400 K (0.12 eV) as measured using an optical pyrometer. This corresponds with a Doppler broadening $\Delta\lambda = 0.07$ Å at H_α. The spectrum measured by the spectrometer is shown in Fig. 5.8. A Gaussian fit to the data gives a width of 0.73 channels, which corresponds to $\Delta\lambda = .31$ Å. Since the broadening sources are added in quadrature, it is concluded that the instrumental broadening is 0.30 Å.

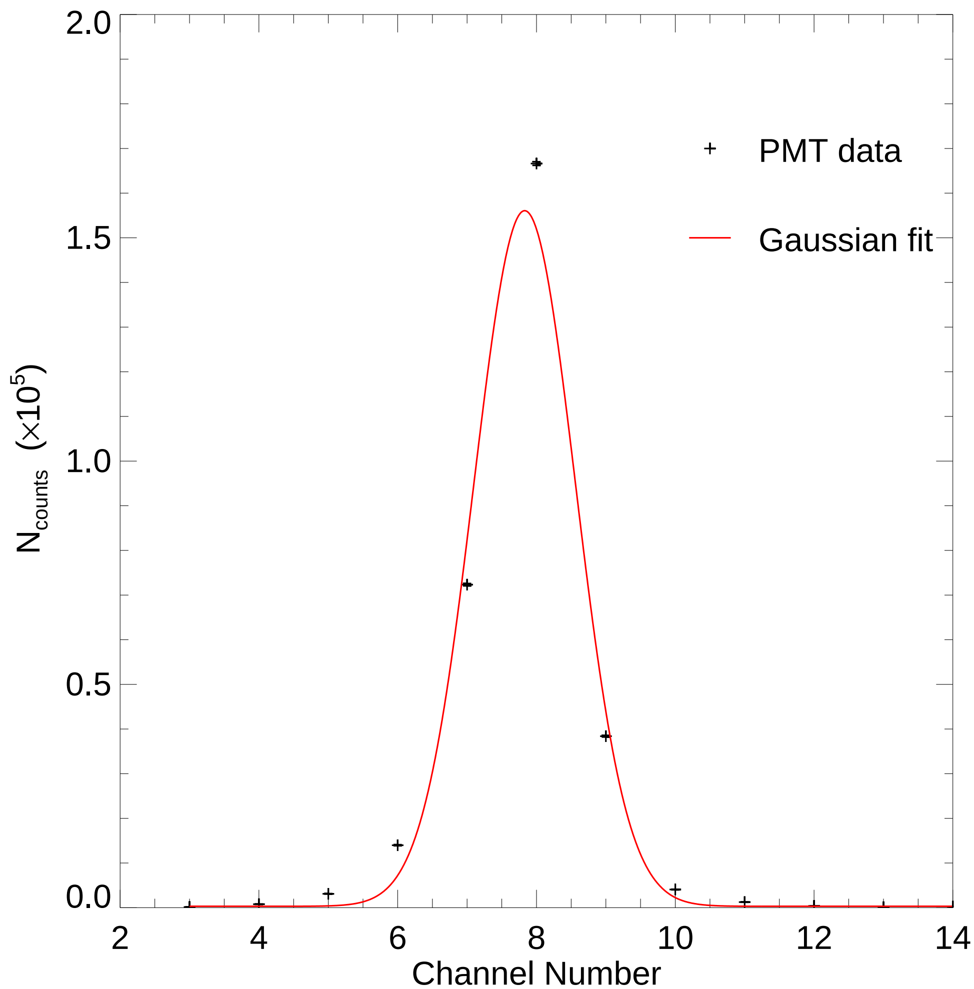

Figure 5.8: Gaussian fit performed on hydrogen lamp. Peak is at channel 7.83 and the width is 0.73 channels.

Species	H	He	C	Ar	Kr
Ionization	I	I	II	II	II
Wavelength (Å)	6562.85	5875.62	6578.05	4879.86	5681.90
$\Delta\lambda(T = 1\text{eV})$ (Å)	0.22	0.10	0.06	0.03	0.02
$\Delta\lambda(T = 10\text{eV})$ (Å)	0.69	0.31	0.20	0.08	0.07
$\Delta\lambda(T = 100\text{eV})$ (Å)	2.2	0.99	0.63	0.26	0.21

Table 5.2: Doppler shifts for observed lines at various temperatures.

5.5.2 Doppler Broadening

Doppler broadening is line broadening due to the thermal motion of the plasma. For a plasma in the presence of a magnetic field, cyclotron motion also results in broadening. However, if the plasma is described by a Maxwellian distribution, then the cyclotron broadening is identical to Doppler broadening[52]. The Doppler broadened width is given by

$$\Delta\lambda = \lambda_0\sqrt{\frac{kT}{mc^2}}. \tag{5.13}$$

Computed values for Doppler shifts over a wide temperature range is shown in Table 5.2.

5.5.3 Stark Broadening

Stark broadening is the broadening of a line due to the presence of an electric field. In a plasma, this becomes a noteworthy effect at high densities. The density threshold at which Stark broadening becomes important depends the point at which it becomes comparable to the other broadening sources.

An estimate of the effect Stark broadening has on an emission line is obtained by considering the quasi-static perturbation to the electric field[53]. This model is based on the following assumptions:

1. Perturbers are distributed randomly in space.

2. Only the perturber closest to the emitter exerts the field on the emitter.

A physical interpretation of the model is that the particles are moving sufficiently slowly so that the frequencies characterizing the time-dependence of the perturbing electric field $F(t)$ produced near the emitter during the interaction are much smaller than the resulting Stark shifts[54]. This is satisfied if

$$\left|\frac{\dot{F}(t)}{F(t)}\right| << |\Delta\omega(F)| \tag{5.14}$$

where $\Delta\omega$ is the Stark shift in frequency for a perturbing field F. The perturbing field is just the Coulomb force

$$F = \frac{Zq}{4\pi\epsilon_0 r^2} \tag{5.15}$$

with the nearest perturbing distance r given by $(4\pi n_e/3)^{-1/3}$ where n_e is the electron density. The rate at which measured quantities such as the magnetic fields, plasma current, and density change is at most around 1 MHz, or 6 Mrad/s. To determine whether or not this model is valid, the right hand side of Eq. 5.14 must be evaluated and compared with typical time scales.

Calculation of the Stark shift requires the multipole expansion of the electrostatic interaction Hamiltonian

$$H_{int} = -q^2 Z \sum_i \left\{ \frac{\vec{r_a} \cdot \vec{r_i}}{|r_i|^3} + \frac{3}{2}\left[\frac{(\vec{r_a} \cdot \vec{r_i})(\vec{r_a} \cdot \vec{r_i})}{|r_i|^5} - \frac{1}{3}\frac{\vec{r_a} \cdot \vec{r_i}}{|r_i|^3} \right] \right\} \tag{5.16}$$

where the subscript a is for the radiating electron, and i is for the perturber (nearby electron). To first order, this is just

$$H_{int} = -q\vec{r_a} \cdot \vec{F}. \tag{5.17}$$

From quantum mechanics, the shift in energy is found by evaluating the matrix elements ($< n', l', m'|H_{int}|n, l, m >$)[55]. The shifted frequency $\Delta\omega$ from $E = \hbar\omega$, is[54]

$$\Delta\omega(F) = \frac{3}{2}n(n_1 - n_2)\frac{qa_0}{\hbar Z}F \tag{5.18}$$

where a_0 is the Bohr radius, n is the principle quantum number, and n_1 and n_2 are the parabolic quantum numbers. The angular momentum quantum number l can have the values $0, 1, ..., n-1$ and the parabolic quantum number n_j can have the values $0, 1, ..., n-l-1$, so the maximum possible Stark shift is obtained when $n_1 - n_2 \rightarrow n-1$ giving

$$\Delta\omega(F) = \frac{3}{2}n(n-1)\frac{qa_0}{\hbar Z}F \tag{5.19}$$

For the H_α transition, $n = 3$ resulting in $\Delta\omega = 1.4 \times 10^5$ Mrad/s. From this, Eq. 5.14 is satisfied and the model is applicable.

For the H_α transition, the resulting broadening is calculated to be 0.27 Å. The computation of the quantum mechanical matrix elements becomes increasingly complex with the introduction of more electrons (and degeneracy of energy levels[53]) for the other observed transitions listed in Table 5.1. For these transitions, the relationship analogous to Eq. 5.19 is quadratic in F:

$$\Delta\omega(F) \propto F^2. \tag{5.20}$$

The Stark broadening for non-hydrogenic lines is estimated by using experimentally measured data and scaling it to the densities expected in IFRC using Eq. 5.20 and Eq. 5.15. The estimated Stark shifts, based on an electron density in IFRC of 10^{14} cm^{-3}, are shown in Table 5.3. Hydrogen is the only observed line with a Stark shift that is comparable to the Doppler and instrumental broadening.

Species	$n_e(cm^{-3})$	$\Delta\lambda(\text{Å})$	Ref.	IFRC $\Delta\lambda$ (Å)
H	10^{15}	1.2	[56]	0.26
He	10^{18}	33	[57]	2×10^{-4}
C	2×10^{17}	2.2	[58]	10^{-4}
Ar	10^{17}	0.2	[59]	2×10^{-5}
Kr	10^{17}	0.2	[60]	2×10^{-5}

Table 5.3: Stark shifts for observed lines from experimentally measured data.

Chapter 6

IFRC Characterization

This chapter contains the data from the diagnostics described in the previous chapters. These data are used to understand IFRC's magnetic and electric field structure, as well as the density profile. The ion and electron temperatures have been measured, as well as the ion drift velocity and plasma current.

In addition to these measurements, some noteworthy features are discussed along with possible explanations. A very important observation is that the null surface moves out of the line-of-sight of several of the diagnostics (interferometer, charge-exchange analyzer, and spectrometer) throughout the discharge. The average ion drift velocity is below the minimum energy threshold of the time-of-flight diagnostic. The time evolution of the intensities for the different spectral lines under investigation are not the same. Finally, the broadening of the spectral lines is much larger for the ions than it is for the neutrals.

Section 6.1 gives an overview of a typical IFRC discharge. The magnetic field structure is presented in Sec. 6.2. Measurements from the charge-exchange neutral particle analyzer are shown in Sec. 6.3. Section 6.4 has the data from the spectrometer, along with analyses of the intensity's temporal evolution and line broadening. Section 6.5 shows some data from a set of charging parameters that results in a larger ($5\times$) gyroradius during FRC formation. A summary of IFRC's plasma characteristics is in Sec. 6.6.

6.1 General Overview

The charging parameters for a typical shot in IFRC are 5.4 kV on the flux coil, 1.3 kV on the limiter coil, and 16 kV on the plasma guns. The relative timing between the capacitor bank triggers are (dialed settings): limiter coil at $t = 0$ μs, plasma guns 5 μs after the limiter coil, and flux coil 6 μs after the plasma guns. These dialed settings actually correspond to the limiter firing at $t = 5$ μs, plasma guns at $t = 9$ μs, and flux coil at $t = 17$ μs where $t = 0$ μs is when the data acquisition system is triggered. The parameters are chosen to give a plasma that lasts as long as the rise time of the flux coil.

As mentioned in Chapter 3, the magnetic fields in IFRC are produced by capacitive discharges through magnetic field coils. The current through these coils are measured by Rogowski current monitors, which are useful since they tell us exactly when the coils fire and how strong the applied fields are. The timing of the magnetic fields in IFRC is shown by the current traces in Fig. 6.1. Figure 6.1a shows the current that provides the background magnetic field through the limiter coil and the flux coil, delayed about 13 μs afterwards, is shown in Fig. 6.1b. The Rogowski coil measuring the plasma current shows that it rapidly rises as soon as the flux coil fires, and peaks at 15 kA. From this, it is evident that the flux coil is driving the plasma current, as expected from the explanation in Chapter 2.

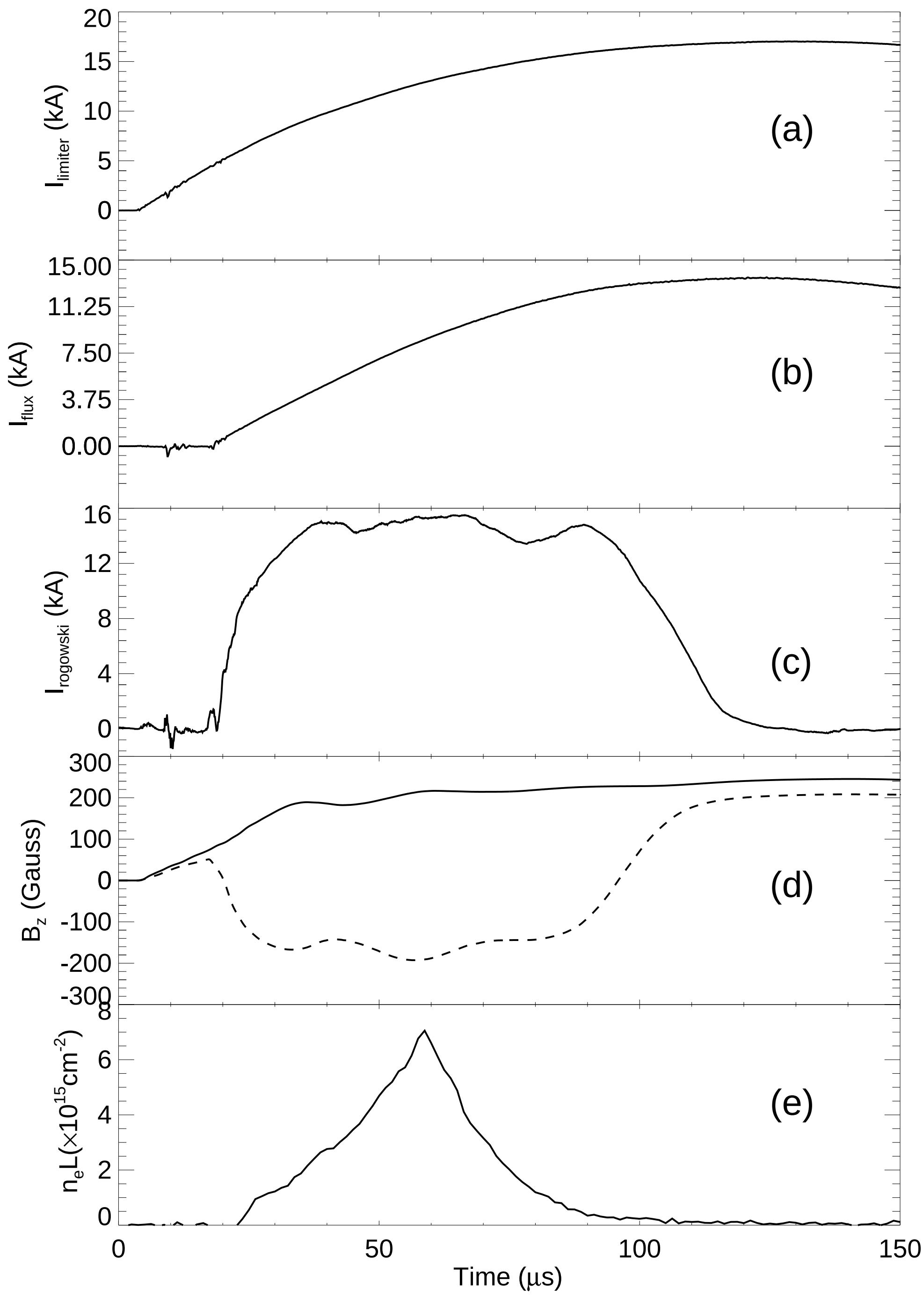

Figure 6.1: Current through the limiter coil (a), flux coil (b), and total plasma current (c). Axial magnetic field (d) at the midplane on the outermost radius (solid) and innermost radius (dashed). Line integrated density (e) measured on a similar discharge.

Pick-up loops measuring the axial magnetic field (described in Chapter 3) show that the field reversal starts within 250 ns of the firing of the flux coil. The magnetic field measured at the flux coil (innermost, dashed trace) and limiter coil (outermost, solid trace) radii in Fig. 6.1d show typical field reversal of $\pm$200 Gauss and a lifetime of 80 μs. As shown in the dashed trace, the time it takes for reversal to occur is $\sim$ 10 μs.

The line integrated electron density for a typical shot is shown in Fig. 6.1e. Although the signal decays after 60 μs, this is most likely due to plasma core moving out of the interferometer's line of sight. As shown in the following section, radial magnetic probe measurements show the null surface moving inwards (out of the line of sight) during this time. The motion of the null surface is dependent on the external field, as shown for different charging parameters in Sec. 6.5.

As observed in these traces, the plasma current starts to drop as the flux coil approaches its peak. It is not clear whether the lifetime is restricted by the rise time of the flux coil or density decay since the line integrated density starts to decay much earlier than the current. Viewing port limitations restrict the interferometer chord to the present location.

6.2 Magnetic Field Structure

A radial array of magnetic probes oriented in the axial direction is used to map the magnetic structure within the plasma. The resulting data are shown in Fig. 6.2 with nine probes left out for clarity. A characteristic of the FRC is that the outermost probes remain in the positive direction throughout the discharge while the innermost probes reverse directions. After $\sim$100 μs, the FRC is no longer sustained and the

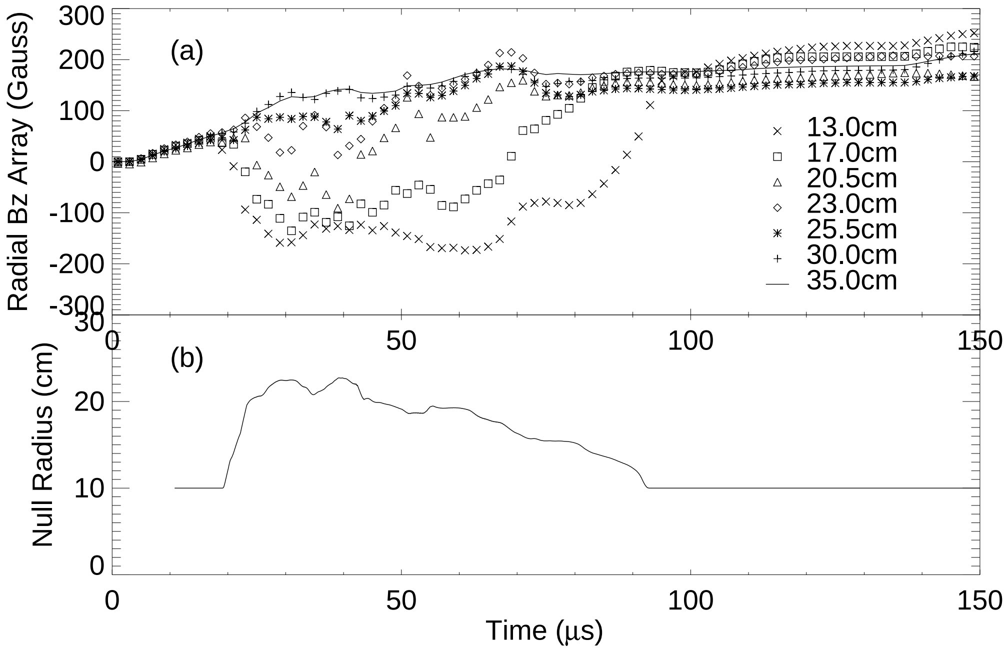

Figure 6.2: (a) Radial magnetic field profile at the midplane for a typical shot. Only seven probes are shown for clarity. (b) The interpolated null surface versus time.

measured fields are from the background magnetic field.

The null radius (where $B = 0$) is found by interpolating the radial probe data. Theoretically (Chapter 2), the peak density is centered near the null surface, so this estimate of the null radius provides an estimate of the extent of the current ring. This set of formation parameters results in a null surface that gradually collapses onto the flux coil as time evolves.

6.3 Charge-Exchange Neutral Flux Measurements

Time-of-flight data from IFRC are shown in Fig. 6.3. Timing calibration described in Chapter 4 was performed to verify that the peaks at 37 and 75 μs are photon pulses from emitted UV radiation. In all further data analysis, the photon peak is used as a timing reference. It should be noted that as the detector bias increases, the photon pulse distorts and widens due to saturation of the detector. This explains why the photon peak in Fig. 6.3a is wider than the 2.5 μs slot open time. At low bias voltages ($\sim$1.5 kV), however, the photon peak closely resembles the expected aperture function from Eq. 4.4. To verify that the detector has recovered from saturation, the output current has been integrated to show that the total charge depletion is typically less than 10% of the total charge, indicating there is still plenty of charge reserved for when the neutrals arrive. The charge-exchanged neutral signal lies between the photon pulses and can be seen by increasing the vertical resolution as shown in Fig. 6.3. The data indicate that the neutral detection is operating in a regime between analog and pulse counting mode, as seen by the sharp pulses overlaid on top of a broad signal.

Raw data from the charge-exchange neutral particle analyzer at a single time slice are shown in Fig. 6.4. The observed neutral flux peaks at $\sim$60eV. After taking into account the energy dependent detector sensitivity and charge-exchange cross section (described in Chapter 4), these data indicate that the peak toroidal drift energy of the detected neutrals is less than 20 eV (30 km/s), which is the low energy cutoff for the diagnostic.

By varying the time delay of the plasma discharge relative to the chopper wheel rotation, the toroidal velocity distribution function is found as a function of time (Fig. 6.5). For all contours of the neutral particle flux, the levels increase linearly. The data shown is along a line of sight whose minimum radius is 17 cm and peaks at $\sim$45 eV at 54 μs. The red, green, and blue vertical lines indicate when the limiter coil, plasma guns, and flux coil fire, respectively. Correcting for the detection efficiency and charge-exchange cross section results in the contour plot shown in Fig. 6.6. As in Fig. 6.4, the corrected data results in a peak below the 20 eV minimum energy threshold.

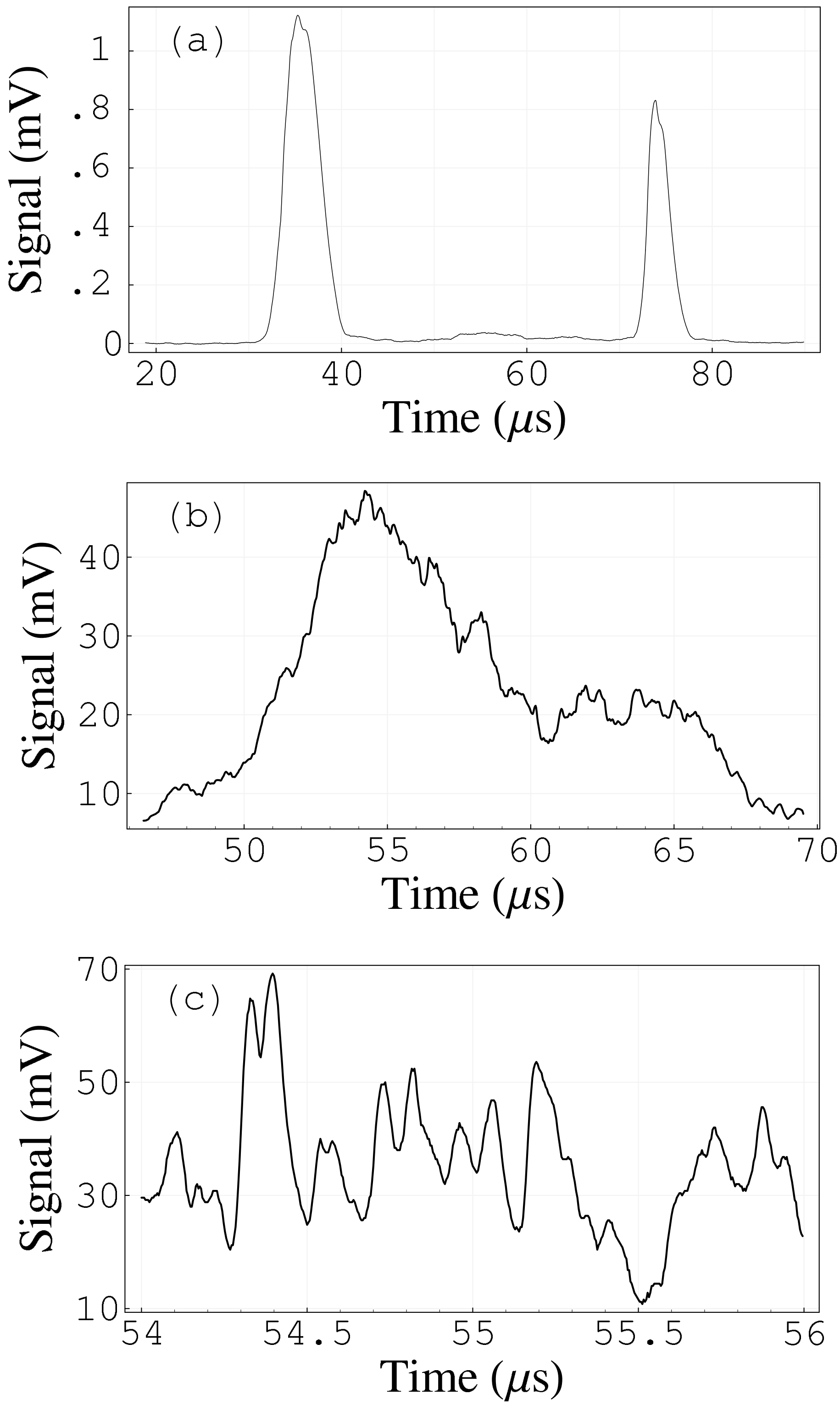

Figure 6.3: TOF data from IFRC for CEM biased at -2.5 kV. The data have been smoothed over 1 μs for (a) and (b). The photon peaks are shown in (a), while the neutral signal in (b) has been zoomed to show response from individual ions in (c).

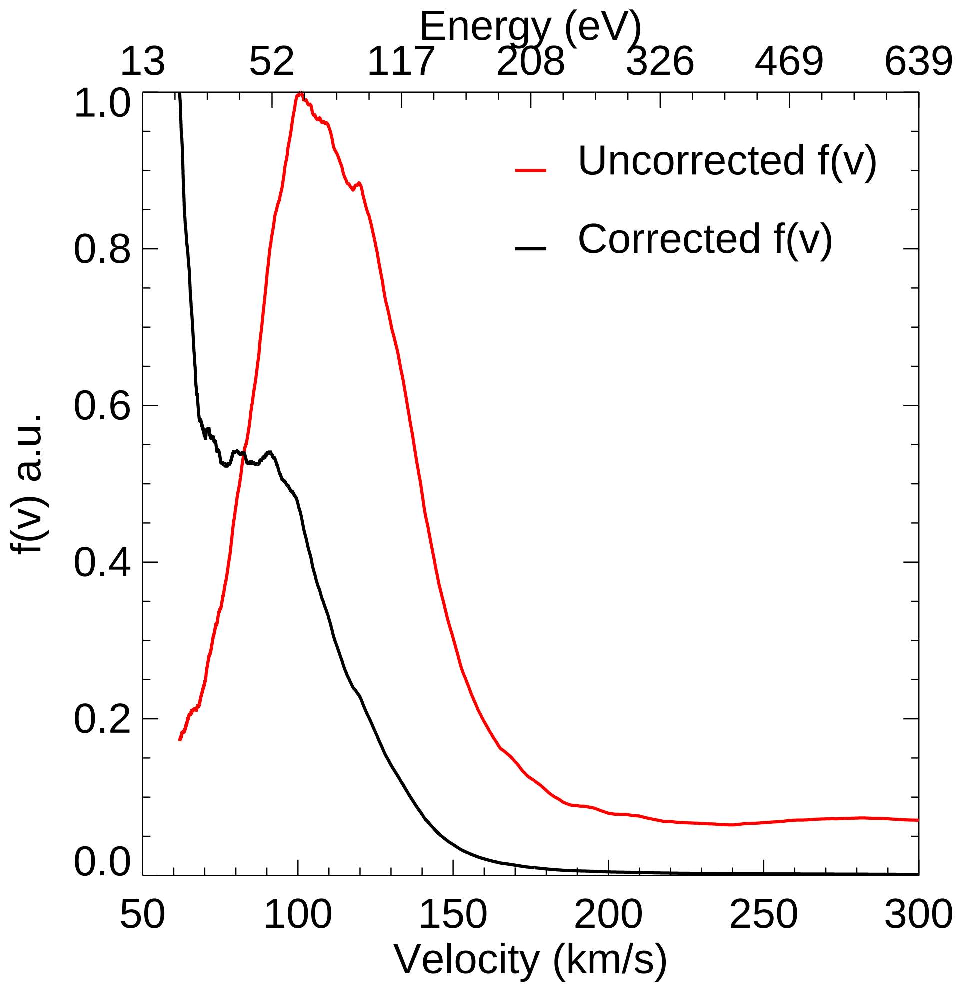

Figure 6.4: Charge-exchange neutral particle velocity distribution- uncorrected (red) and corrected (black) for detection efficiency and charge exchange cross section energy dependence.

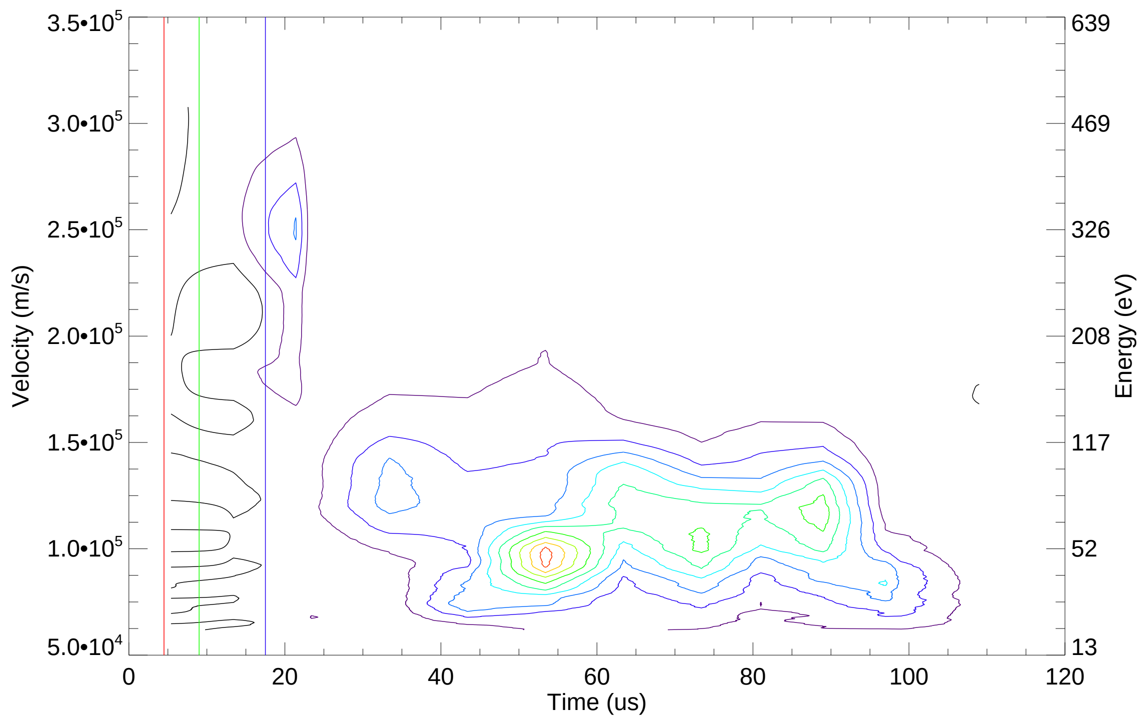

Figure 6.5: Contour showing uncorrected charge-exchange neutral particle velocity distribution as a function of time. Contour levels are in increments of 10% of the total distribution. The red, green, and blue vertical lines indicate when the limiter coil, plasma guns, and flux coil fire, respectively.

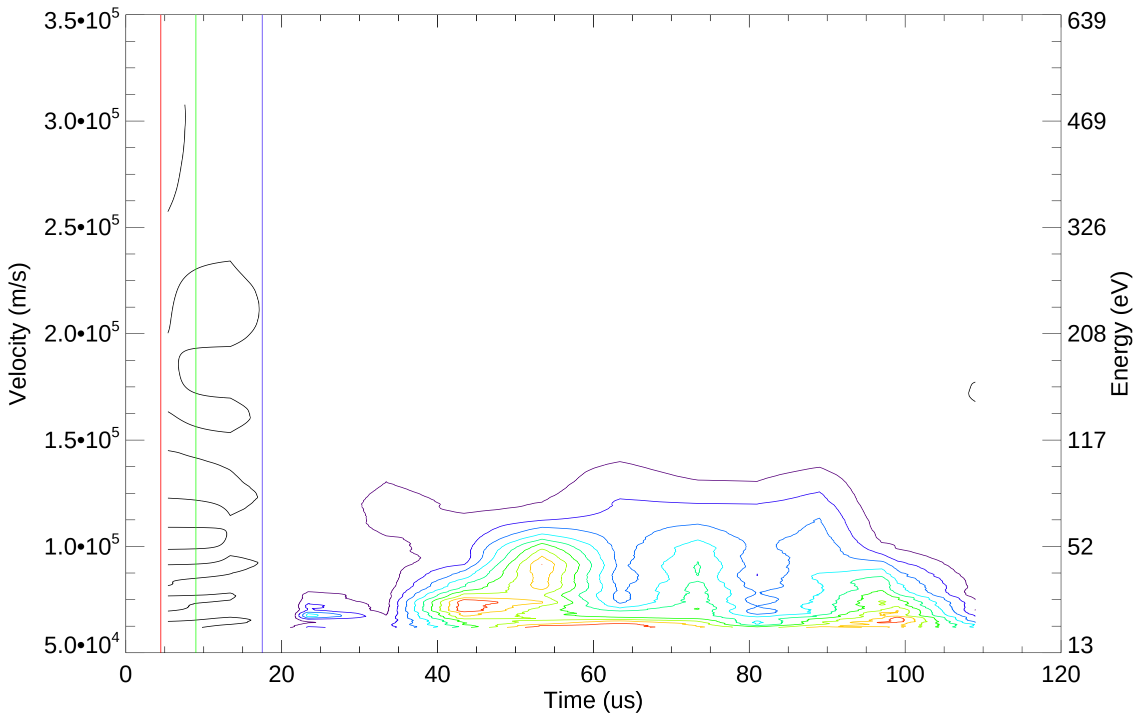

Figure 6.6: Contour showing charge-exchange neutral particle velocity distribution as a function of time. Contour levels are in increments of 10% of the total distribution.

Varying the diagnostic's line-of-sight permits neutral flux measurements to be made along various chords (Fig. 6.7). In doing this, the maximum signal occurs when the line-of-sight intersects the part of the plasma with the largest number of charge exchange reactions. This region is the core of the plasma at the null surface, where the ion density is the highest. As shown, the neutral flux is largest at a minimum intersecting radius of 17 cm, which is the lowest limit possible due to physical constraints of the vessel.

The previous data from the time-of-flight diagnostic are with the detector facing the direction of the plasma current. Measurements from this direction should show a peak at the location of the average drift velocity. Similarly, moving the diagnostic so that the line-of-sight is along the opposite direction should result in seeing only the tail of the distribution. Data from observations along both (co- and counter-current) directions are shown in Fig. 6.8. The data are obtained by averaging five shots with the detector looking in the co-current direction, so that detected neutrals ($v<0$) must be traveling in the counter-current direction, and repeated with the detector facing in the counter-current direction ($v>0$). As observed, the peak in the neutral flux lies below the minimum energy threshold when viewed from both directions. This indicates that the flow of neutrals must be less than 30 km/s, which is in agreement with the spectroscopic data shown below. A flow of 30 km/s is less than 5 eV, which is much lower than the 35 eV drift estimate calculated in Chapter 2. It is likely that collisions which were neglected in the calculation are playing a role in inhibiting the ion acceleration.

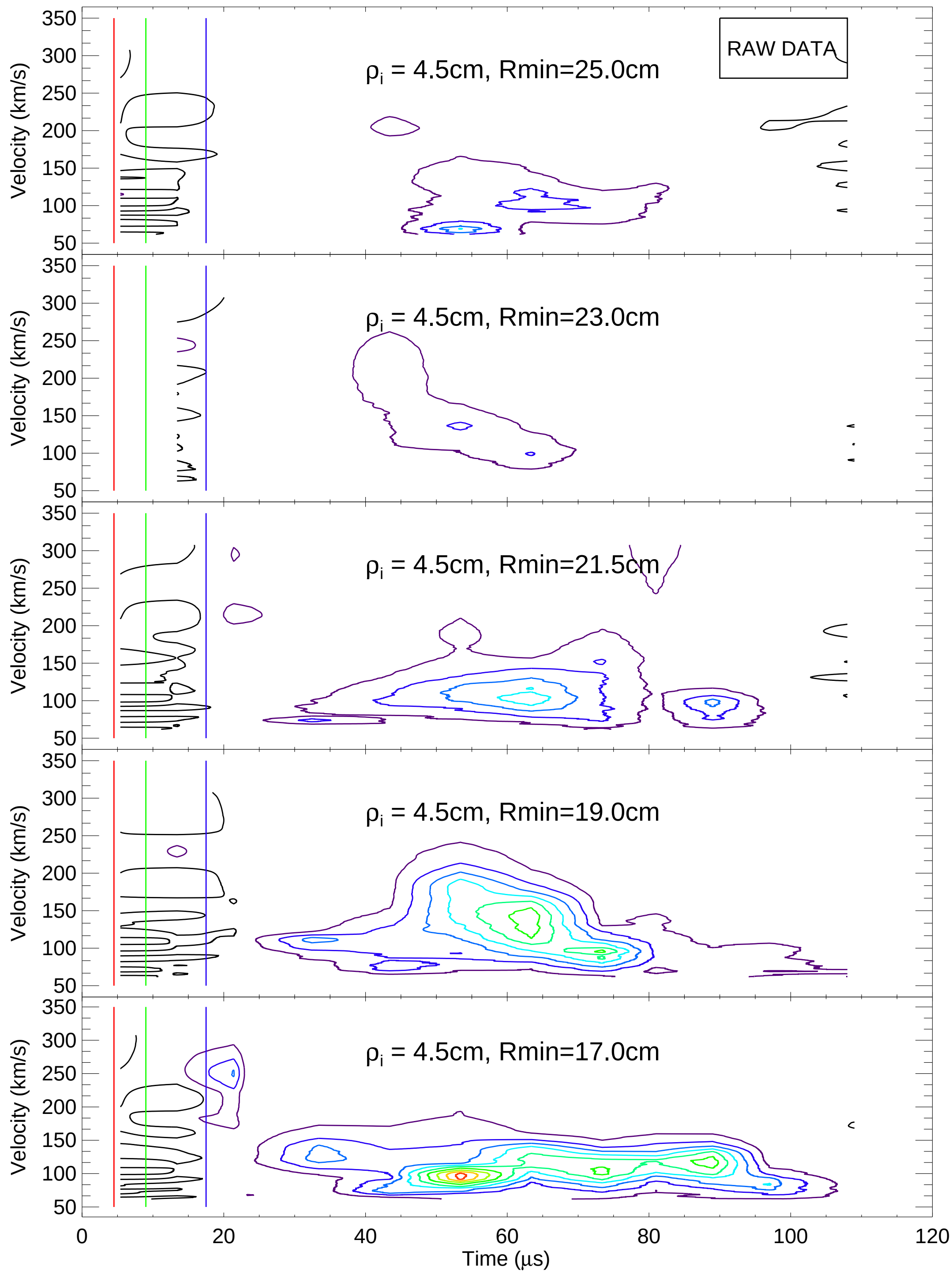

Figure 6.7: Radial variation of neutral flux measurements.

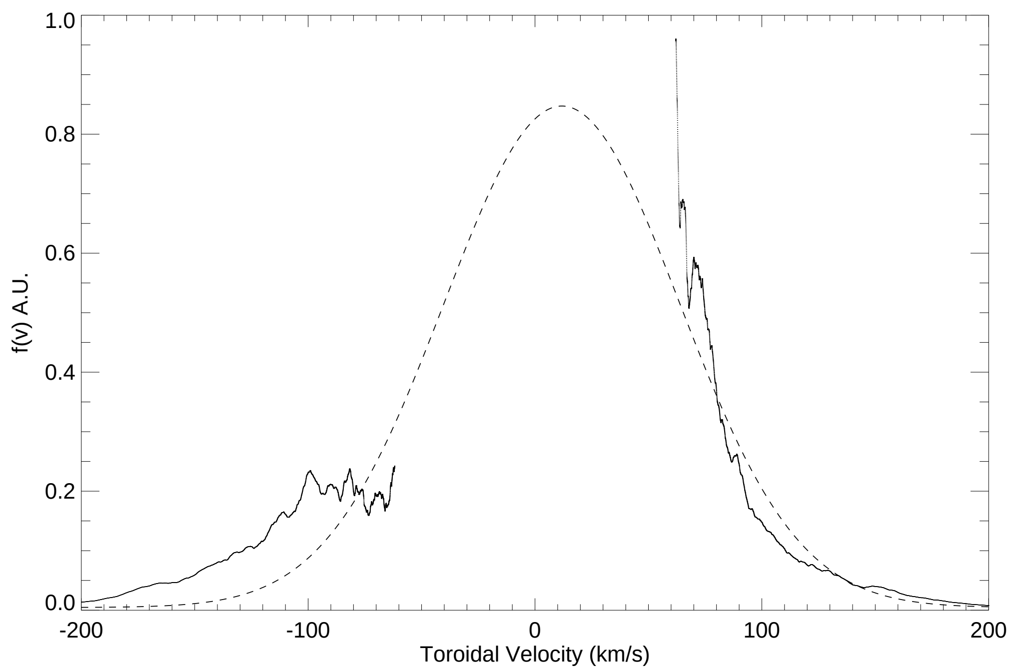

Figure 6.8: Neutral flux measurements looking in the co-current (v<0) and counter-current (v>0) directions (solid). Cartoon indicating that peak of data lies below minimum detectable energy (dashed).

6.4 Visible Emission Spectroscopy

Visible emission spectroscopy is performed on hydrogen and carbon (products from the plasma source), as well as helium, argon, and krypton impurities (as explained in Chapter 5). From these measurements, it is possible to determine the ion (and neutral) drift velocity as well as the ion and electron temperatures. In addition, the line intensities are analyzed for consistency with what is observed from the plasma density measurements.

6.4.1 Line Ratios

The electron temperature can be estimated by the emissivity ratio of different spectral lines in hydrogen[61]. For this method to be valid, the following requirements must be satisfied[61]

- Electrons satisfy a Maxwellian velocity distribution.
- The plasma is optically thin.
- The plasma is in coronal equilibrium.

The Maxwellian distribution is justified since the electron-electron Coulomb collision time is ∼25 ps while the plasma lifetime is 80 μs. Although opacity measurements have not been performed, it is a reasonable assumption that the plasma is optically thin based on the fact that ion Doppler shifts are observed, which presumably originate from the plasma core. The coronal equilibrium condition has been evaluated as follows: the source rates for neutrals $n_i < \sigma_{rec} v >$ and electrons $n_n < \sigma_{ion} v >$ through recombination and electron-impact ionization have been compared to the lifetime of the plasma. Although the exact neutral hydrogen density is not known, assuming

$n_n \approx 0.01 n_i$ and an electron temperature of 3 eV (which is the resulting temperature from the model in question) results in time scales for the corresponding rates of 2 ms and 200 μs for sourcing neutrals and electrons, respectively. It is possible that neutrals are ejected from the plasma guns and the neutral density is actually much larger than 1% of the ion density. In this case, a lower electron temperature is required to balance the rates mentioned above for the coronal model to be applicable.

Since the lifetime of the plasma is typically 80 μs, the coronal model can be employed for electron temperature measurements to a reasonable approximation. The expression used for calculating the electron temperature is

$$kT_e = \frac{x_\beta - x_\alpha}{\ln\left(\frac{\mathcal{E}_\alpha}{\mathcal{E}_\beta}\right) - \ln\left(\frac{\lambda_\beta}{\lambda_\alpha}\frac{f_\alpha}{f_\beta}\frac{A_\alpha}{\sum_i A_{\alpha_i}}\frac{\sum_j A_{\beta_j}}{A_\beta}\frac{x_\beta}{x_\alpha}\right)} \tag{6.1}$$

where x is the upper energy level for the transition, λ is the wavelength, f is the absorption oscillator strength, A is the Einstein transition probability, $\sum_i A_i$ is the total Einstein transition probability for the upper level, k is Boltzmann's constant, T_e is the electron temperature, and $\mathcal{E}$ is the emissivity of the line[61].

The ratio of H_α to H_β emission is used for this analysis, and the resulting data are shown in Fig. 6.9. The line intensities were measured using the spectrometer, and an average of five shots for each line was used for the analysis. As calculated using this method, the electron temperature is in the range of 2-4 eV through the majority of the discharge.

Electron temperature profiles have been shown[62] to be uniform inside the separatrix. Based on this, calculations involving the electron temperature such as the pressure balance condition, assume that the temperature is uniform throughout the plasma.

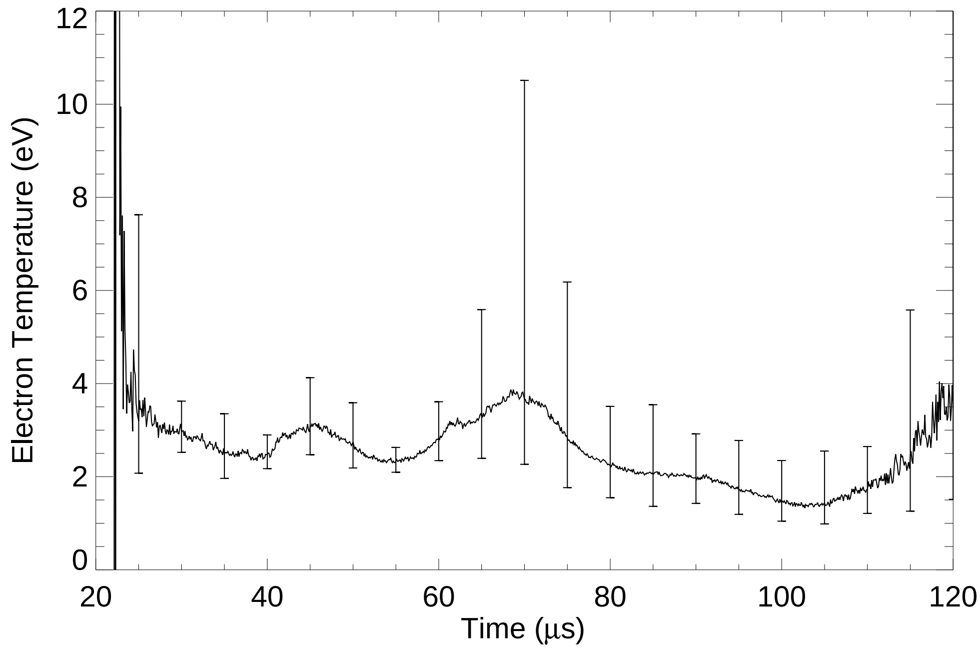

Figure 6.9: Electron temperature as determined by the ratio of H_α to H_β. Error bars from statistical deviation of intensity between multiple shots.

6.4.2 Intensity Measurements

Intensities of the different spectral lines are show in Fig. 6.10. Hydrogen and carbon, being natural products of the plasma source, have the largest intensities (up to 2 V) while helium has the lowest (up to 20 mV). He II was not observed, which is why data is only presented for He I. Argon and krypton gave comparable intensities around 200 mV.

The intensity of the light is proportional to the number of photons detected, which is proportional to the emissivity (Eq. 2.25) where σ is the cross section for electron impact excitation into the observed line. Further discussion of the observed features will be in terms of the emissivity rather than intensity. The emissivity of hydrogen peaks around 65 μs, which is close to when the line-integrated density peaks in Fig. 6.1e. For comparison, the line-integrated density and intensity of the hydrogen

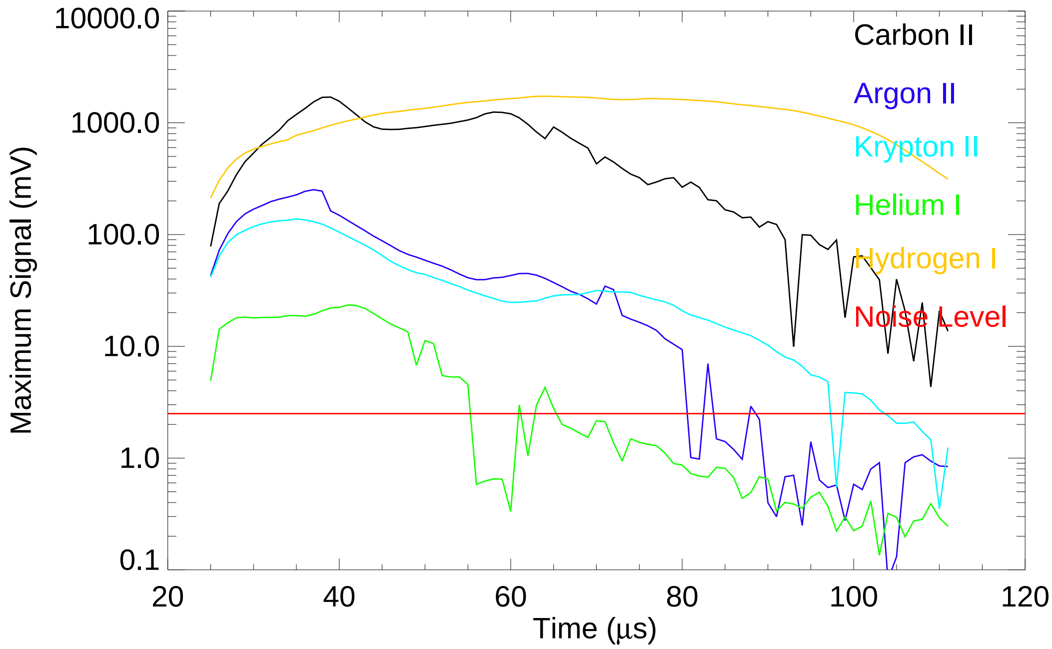

Figure 6.10: Intensities of all spectral lines.

line are shown together in Fig. 6.11a&b, respectively. The differences in the widths is probably due to the fact that the hydrogen emission is occurring throughout the vessel (and mostly at the edge, as described later) while the interferometer measurements are primarily influenced by the dense plasma core, which rapidly moves out of the diagnostic's line of sight.

Argon and krypton, on the other hand, peak much earlier in the discharge at around 40 μs. This can be explained by considering the ionization rate of their neutral atom counterparts. The background neutral density n_0 is determined from the fill pressure in Table 5.1, which turns out to be 5×10^{11} cm^{-3} for argon. The ionization rate is calculated using an empirical formula for the electron impact ionization cross-section σ_{ion}[63]

$$\sigma(E) = a \{1 - b \exp(-c(U-1))\} \sum_{i=1}^{N} q_i \frac{\log(E/P_i)}{EP_i} \tag{6.2}$$

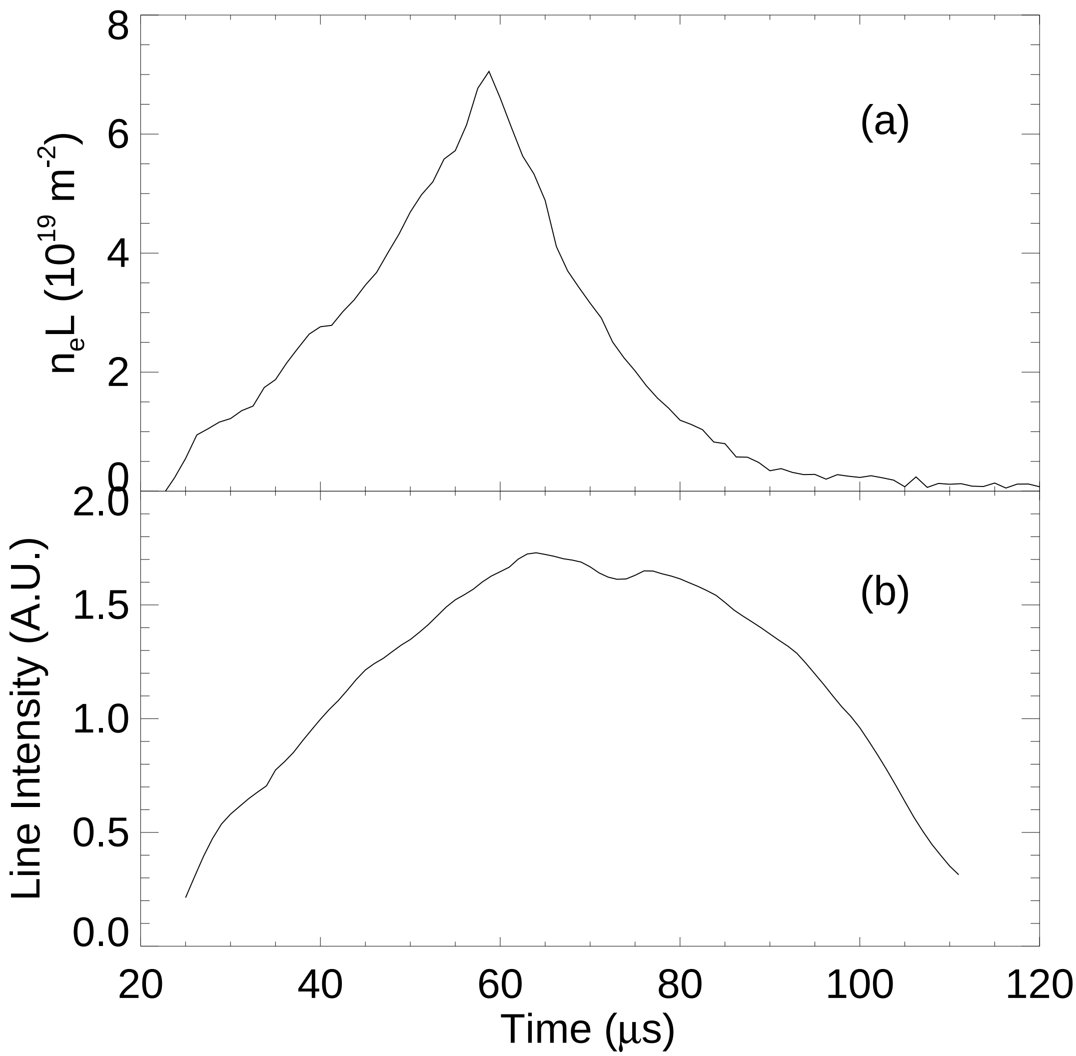

Figure 6.11: Comparison of line integrated density (a) with intensity of hydrogen emission line (b).

where $a = 4.0 \times 10^{-14}$ cm^2, b =0.62, c =0.4, P_1 =15.8 eV, P_2 =29.2 eV, $N = 2$, q_1=6, and q_2=2. Since σ_{ion} is expressed as a function of impact energy E (from the relative velocity between the electron and atom), an average must be performed over all possible electron velocities. The average cross-section $< \sigma v > (t)$ is

$$< \sigma v > (t) = \int_0^\infty f(v,t)\sigma(v)v dv \tag{6.3}$$

where f(v) is the Maxwell speed distribution

$$f(v) = 4\pi \left(\frac{m_e}{2\pi k T_e(t)}\right)^{3/2} \exp\left(\frac{-m_e v^2}{2kT_e(t)}\right) \tag{6.4}$$

and the time dependence arises from $T_e(t)$. The time dependent version of Eq. 2.25 is

$$\varepsilon(t) = n_n(t) n_e(t) < \sigma v(t) > . \tag{6.5}$$

The neutral density $n_n(t)$ is time dependent since they become ionized throughout the discharge. It can be expressed as

$$n_n(t) = n_n(0) - \int_0^t \varepsilon(t')dt' \tag{6.6}$$

where $n_n(0)$ is the neutral density at $t = 0$. It should be noted that this expression neglects electron-ion recombination and is only used as an estimate the shape of the temporal evolution of the emissivity. Combining Eqs. 6.5&6.6 gives

$$\varepsilon(t) = \left(n_n(0) - \int_0^t \varepsilon(t')dt'\right) n_e(t) < \sigma v(t) > . \tag{6.7}$$

This equation is solved using the following recursive solution:

$$\begin{aligned}
\varepsilon(0) &= n_n(0)n_e(0) < \sigma v(0) > && (6.8) \\
\varepsilon(1) &= (n_n(0) - \varepsilon(0)\Delta t)n_e(1) < \sigma v(1) > && (6.9) \\
& \quad \ldots && (6.10) \\
\varepsilon(t_i) &= (n_n(0) - \varepsilon(t_i - 1)\Delta t)n_e(t_i) < \sigma v(t_i) > && (6.11)
\end{aligned}$$

where t_i is the time parametrized by the index i.

Now that the emissivity for ionization reactions is calculated, the emissivity for excitation reactions are calculated using Eq. 6.7 with $< \sigma v >$ being the average electron impact excitation cross-section. For excitation, the empirical formula is[64]

$$\sigma(E) = A\left(\frac{c_1\left(\frac{E-E_{th}}{E_R}\right)^{c_2}}{1+\left(\frac{E-E_{th}}{c_3}\right)^{c_2+c_4}} + \frac{d_1\left(\frac{E-E_{th}}{E_R}\right)^{d_2}}{1+\left(\frac{E-E_{th}}{d_3}\right)^{d_2+d_4}}\right) \tag{6.12}$$

where E_{th} =35.44 eV, c_1 =1.76, c_2 =1.20, c_3 =9.43, c_4 =0.42, d_1 =0.607, d_2 =2.81, d_3 =14.68, d_4 =0.845, and $A = 42 \times 10^{-20}$ cm^2. The analysis described above is summarized by the plots in Fig. 6.12. This shows that the peak emission is around 45 μs (Fig. 6.12d), which is much closer to the measured peak at ~38 μs (Fig. 6.12e). As shown, the excitation emissivity is very sensitive to electron temperature. Without taking the time dependence of the neutral density into account, the peak emission occurs where the electron temperature (Fig. 6.12a) peaks (~70 μs). For reference, the ionization emissivity is shown in Fig. 6.12b along with the corresponding time-dependent neutral density in Fig. 6.12c.

While the hydrogen line has a shape that peaks closer to where the line-integrated density peaks, the impurities do not. An analysis of the argon line shows that the neutral density decreases throughout the discharge, and results in fewer atoms available

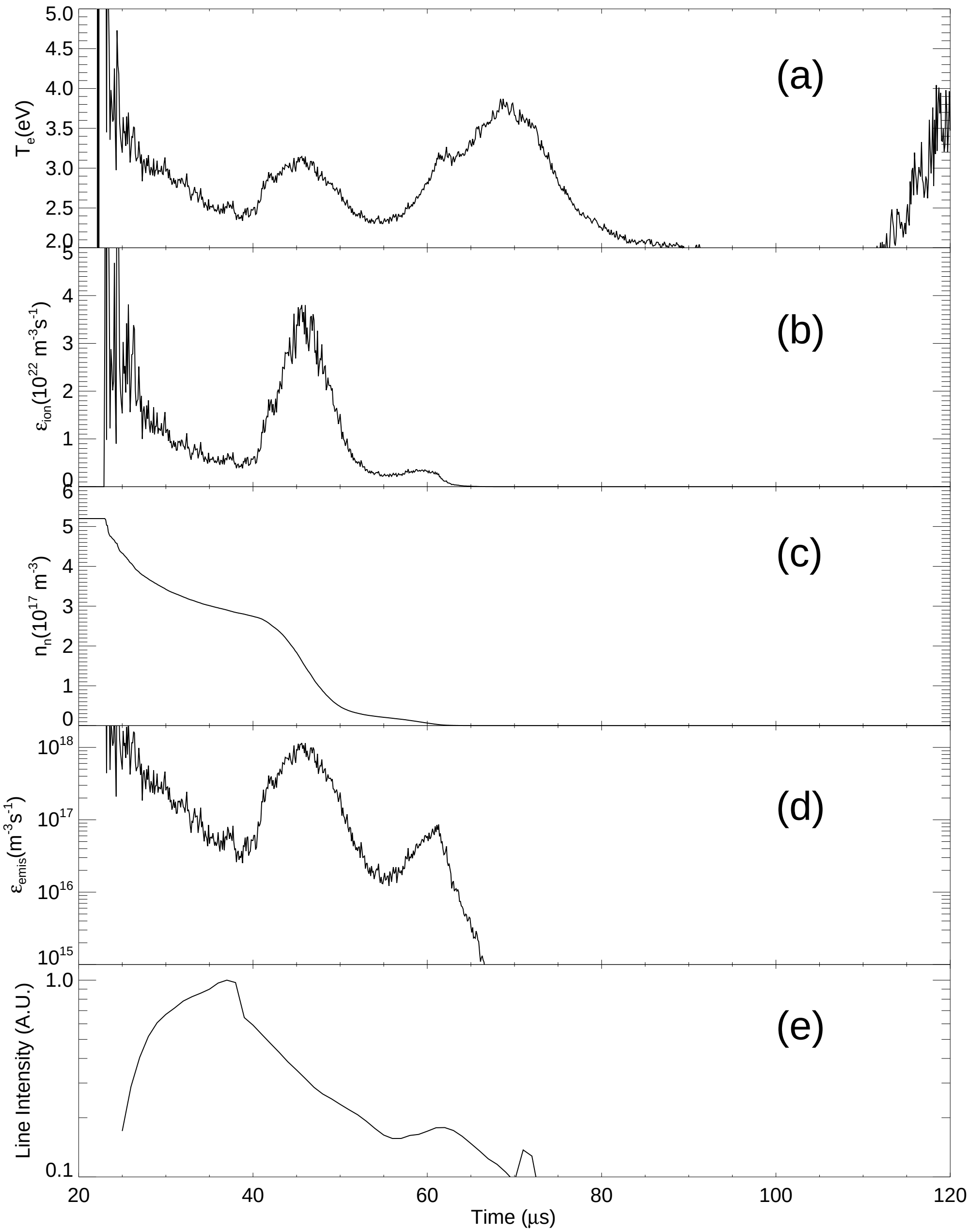

Figure 6.12: Analysis of the argon emission. Electron temperature (a) is shown for reference, along with the emissivity corresponding with argon ionization reactions (b), calculated neutral argon density (c), and emissivity of the observed line's excitation (d). Measured argon line intensity is shown in (e).

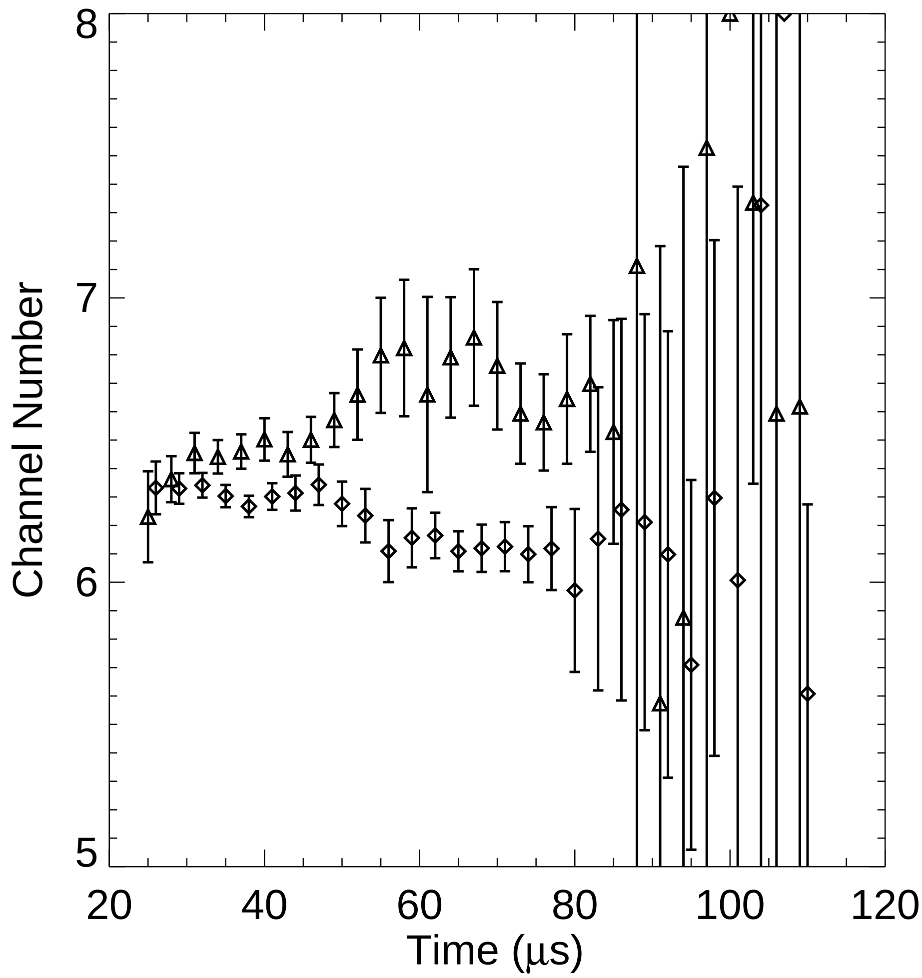

Figure 6.13: Gaussian fit giving the mean PMT channel number observing in the co-current (△) and counter-current (⋄) directions.

for simultaneous electron impact ionization and excitation. Although this analysis does not take into account recombination or electron transitions from different energy levels, it provides insight into the atomic processes that are involved.

6.4.3 Doppler Shifts

The Doppler shift of the argon line for two typical shots is shown in Fig. 6.13. The data shown is the mean channel number resulting from the Gaussian fit described in Chapter 5. It is clear that by looking in the opposite tangential direction, the Doppler shift is reversed. For the data shown in Fig. 6.14, the Doppler shift from the co-current observation direction was subtracted from the counter-current direction and divided by two showing the net ion flow in the direction of the plasma current. The measured Doppler shifts for ArII, KrII, and CII correspond to a drift velocity of 5-7 km/s during the stable FRC time period. Further analysis of the ion flow is presented in Chapter 7.

6.4.4 Line Broadening

The measured energy spread, or effective temperature, was determined by fitting the spectrum to a Gaussian distribution, and converting the wavelength spread into a Doppler broadened temperature after correcting for the instrumental broadening. Figure 6.15 shows the calculated effective temperatures. Although hydrogen and helium appear to have a temperature in the range of 5-10 eV, the ion species peak around 100 eV.

The source of broadening in the ion lines is not fully understood, but there is evidence that supports that it could be a line-integral effect caused by a radial electric field within the plasma. The effect is illustrated in Fig. 6.16. As shown, the projection of the radial electric field vector along the line of sight of the spectrometer's collection optics results in a non-zero component that can accelerate in both directions at opposite sides of the plasma. This results in an effective red and blue shift, which is observed as a broadened line.

As mentioned in Chapter 2, the FRC equilibrium requires a radial electric field. From Fig. 2.2, the peak electric field is around 400 V/m at the edge. Figure 6.15 shows

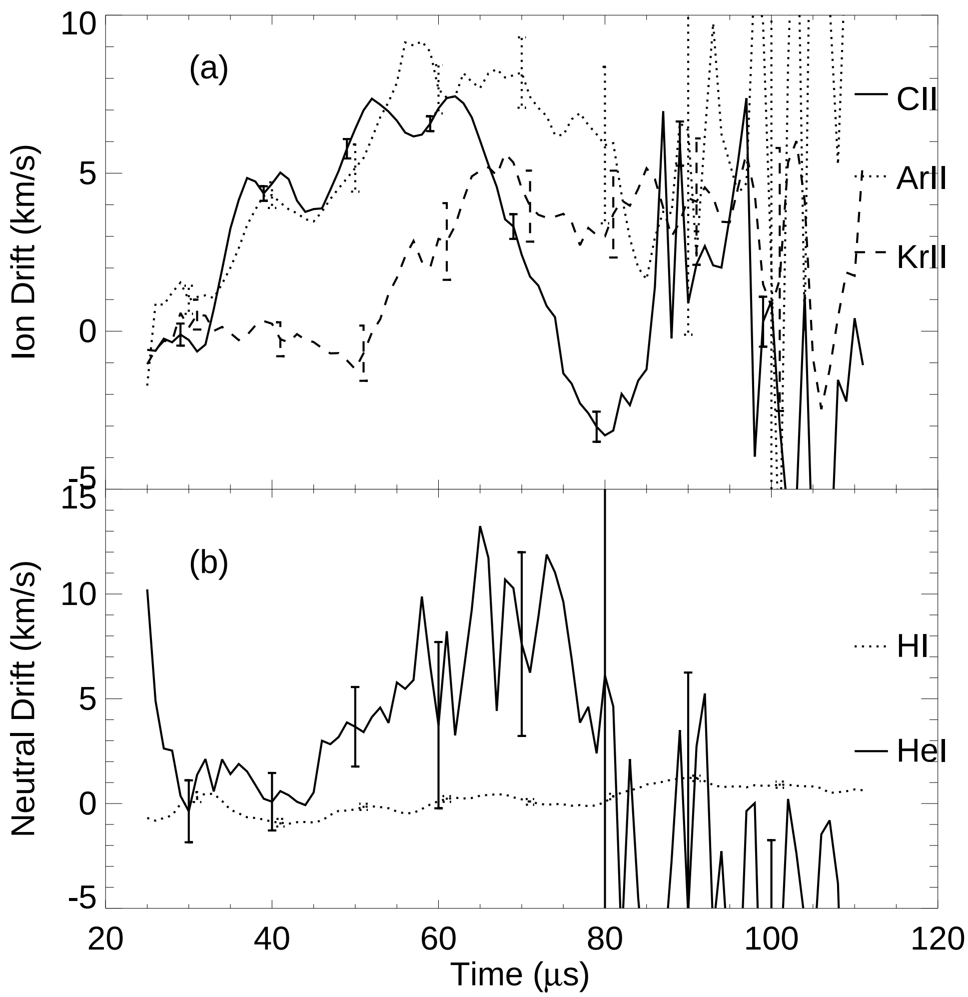

Figure 6.14: Average Doppler shift for observed spectral lines. Ion lines shown in (a) are carbon (solid), argon (dotted), and krypton (dashed). Neutral emission lines (b) are helium (solid) and hydrogen (dotted).

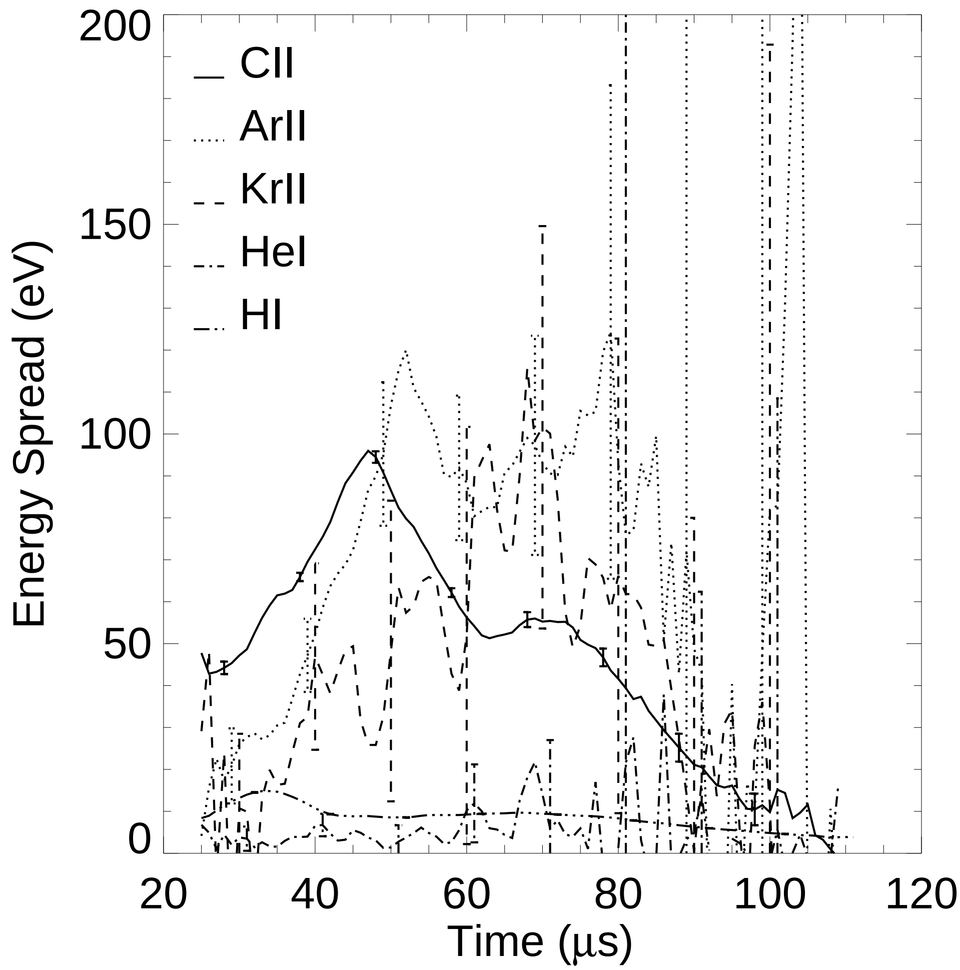

Figure 6.15: Effective temperatures for observed spectral lines: hydrogen (dash-dot-dot-dot), helium (dash-dot), carbon (solid), argon (dotted), and krypton (dashed).

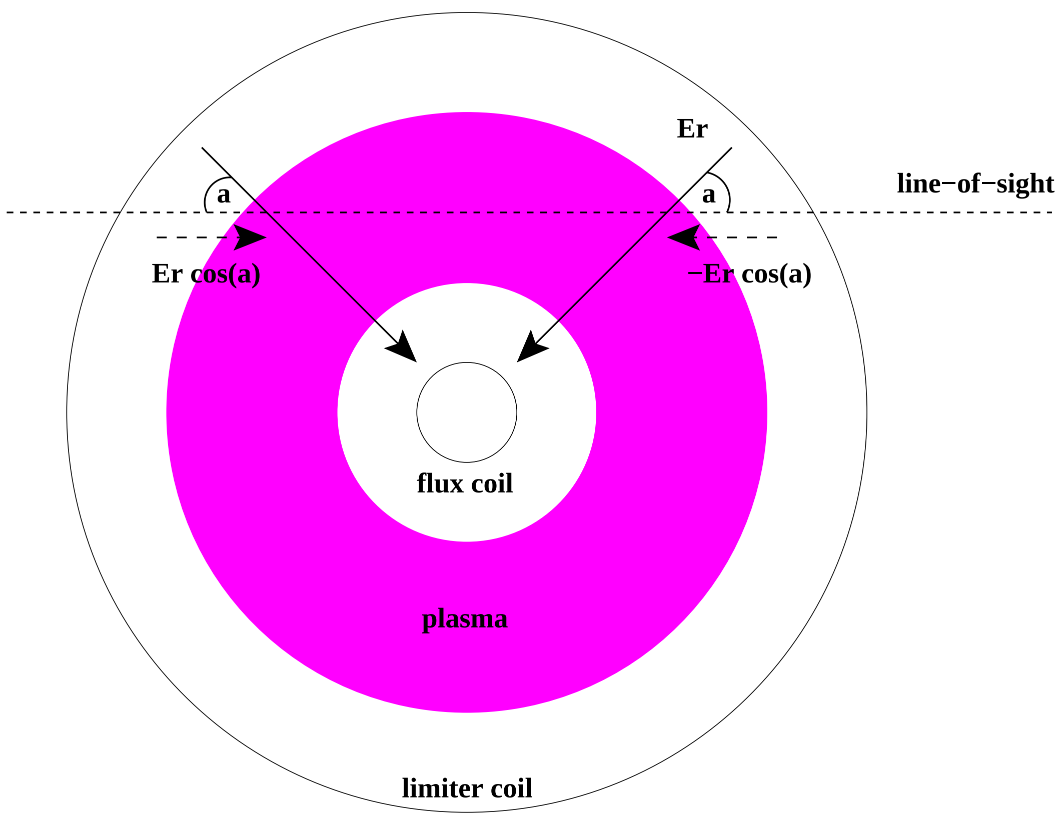

Figure 6.16: Cartoon illustrating line broadening as a result of the radial electric field.

ion temperatures over 100 eV, which corresponds to a thermal velocity of 22 km/s for argon. The amount of time required to accelerate an argon ion to 22 km/s (starting from rest) in an electric field of 400 V/m is ~7 ms, much longer than the time scales observed in IFRC. From this calculation, there would need to be a different radial electric field source for this to be valid.

An alternative source of the electric field could be a voltage differential between the limiter coil, flux coil, and/or plasma guns. This hypothesis was tested by varying the charging voltages on the flux coil and plasma guns and comparing the measured energy spreads for argon. Argon was chosen because:

1. The observed line is an ionized state, so it is affected by the radial electric field.
2. It is not a product of the plasma source, so we know its initial temperature.
3. The light intensity can be increased (by increasing the background pressure) when the signal levels drop low, which occurs at low charging voltages.

When increasing the flux coil charging voltage, an increase in energy spread is observed (Fig. 6.17). Averaging over the smoothest part of the discharge as measured by the magnetic fields and plasma current (50-80 μs), the energy spread is plotted as a function of flux coil charging voltage in Fig. 6.18. The spread clearly varies more than 50 eV over this range, indicating that the flux coil voltage has a significant effect on the energy spread. The error bars in the figure are from the standard deviation over the averaging period.

Keeping the flux coil (and limiter) voltage the same while varying the plasma gun charging voltage gives the traces in Fig. 6.19. For $t < 45$ μs, there is a clear correlation between plasma gun voltage and energy spread. It is reasonable that the plasma guns only affect the plasma in this manner during early times because they

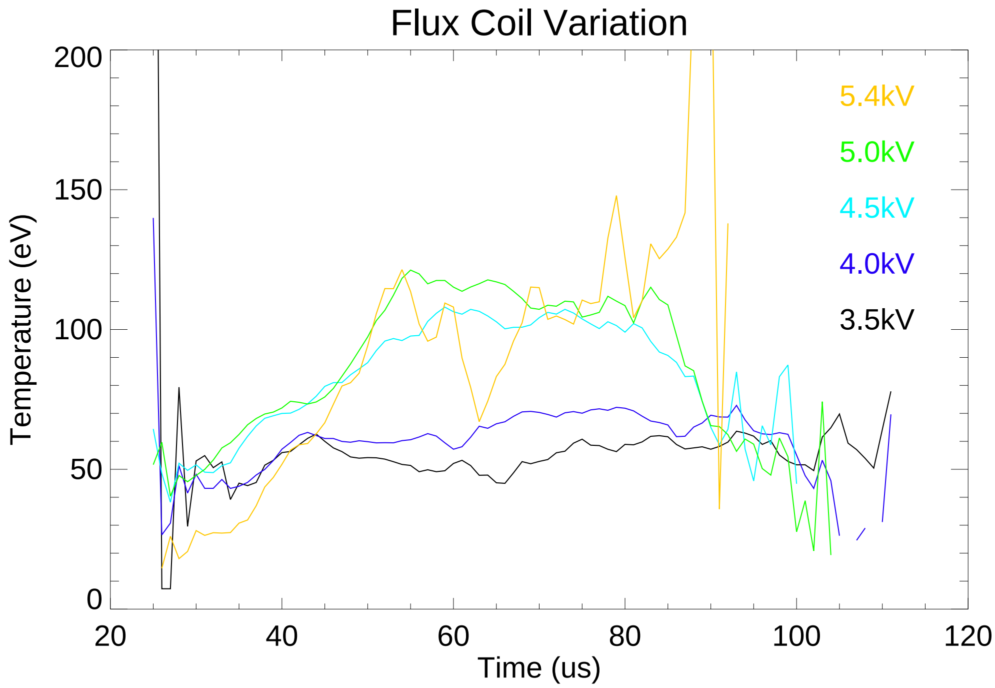

Figure 6.17: Increasing flux coil charging voltage increases energy spread for singly ionized argon.

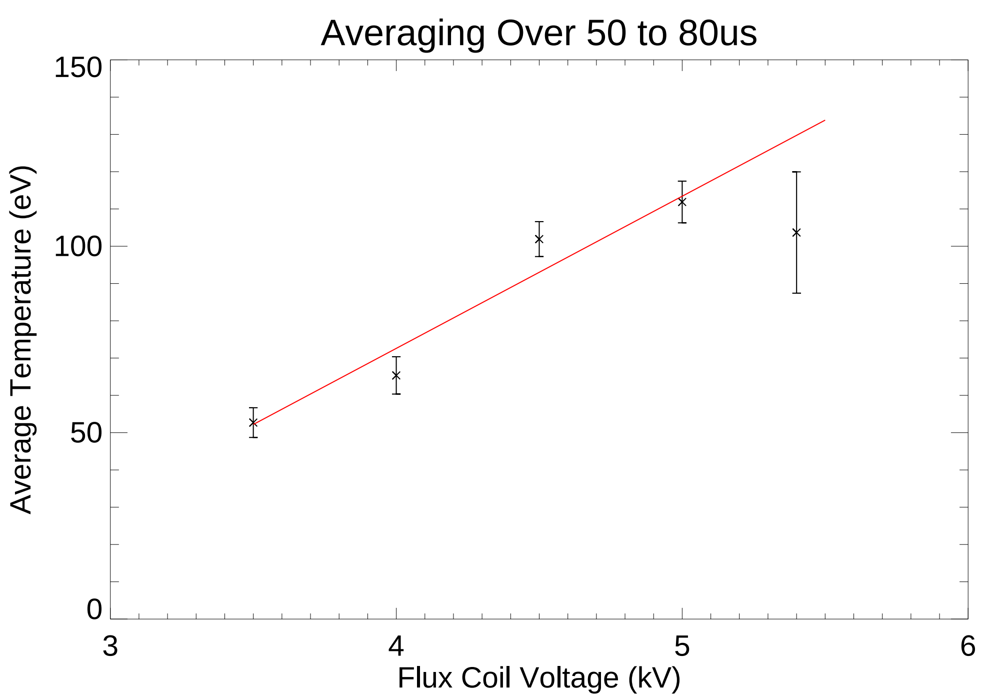

Figure 6.18: Average energy spread for argon over stable portion of discharge for various flux coil voltages.

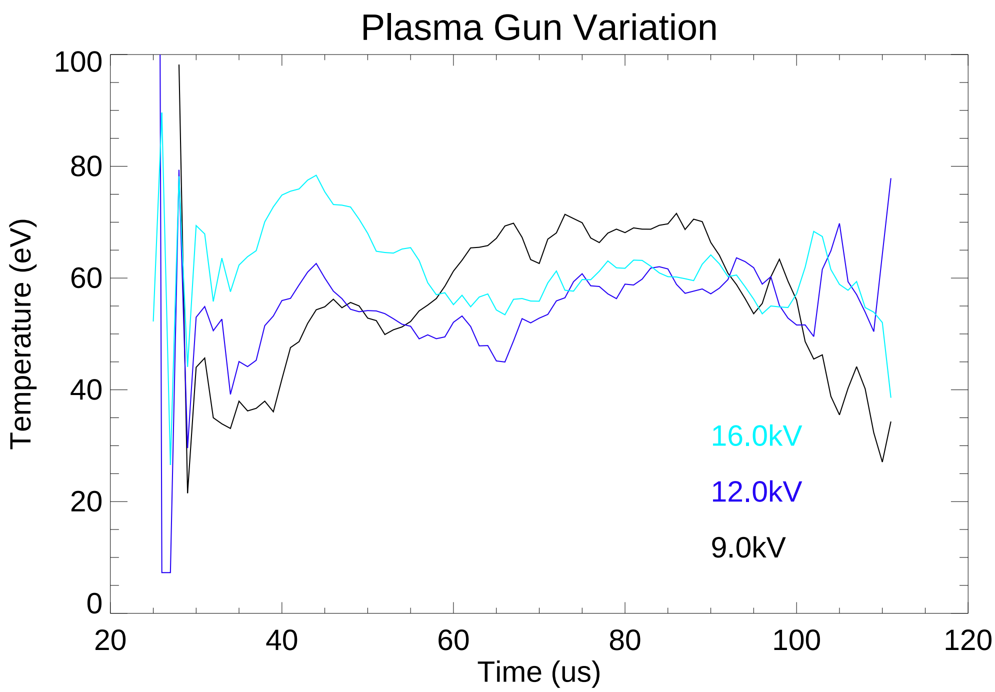

Figure 6.19: Increasing plasma gun charging voltage increases energy spread for singly ionized argon.

only last 10-20 μs after firing (recall, they fire around $t = 10$ μs). Averaging over 30-45 μs gives the traces in Fig. 6.20. From this, there is a 30 eV spread over this range of charging voltages. Again, the error bars are from the standard deviation over the averaging period.

It is clear that varying the flux coil and plasma gun voltages relative to each other has an influence on the measured energy spread. These tests suggest that the energy spread is a result of a radial electric field but do not prove it conclusively. Another possibility is that the plasma is very turbulent; light and heavy ions within the turbulence travel at the same velocity resulting in a higher "temperature" for the heavier ions.

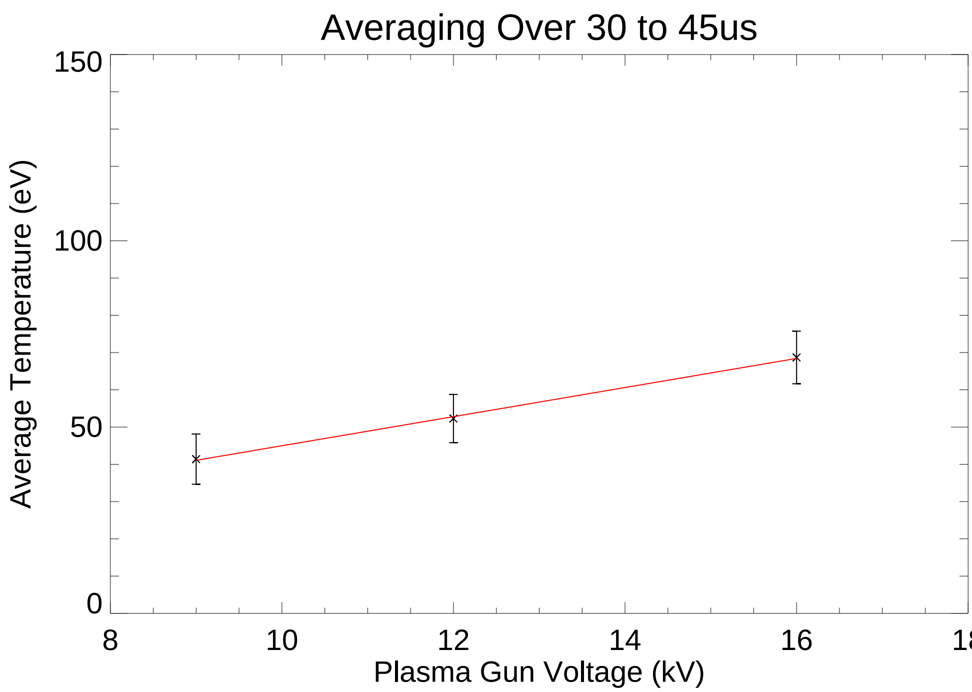

Figure 6.20: Average energy spread for argon over stable portion of discharge for various plasma gun voltages.

6.5 Alternative Formation Scheme

An alternative set of charging parameters (sometimes referred to as "case 2", where the standard set are "case 1") were used in an attempt to study the effect of increasing the ion gyroradius during FRC formation, as explained in Chapter 2. The idea is that, for ion acceleration to occur, the ion gyroradius should be comparable to the system size. When this requirement is met, the unmagnetized ions readily accelerate upon application of a toroidal electric field (from induction due to the flux coil). As outlined in Table 6.1, the magnetic field at the time of firing the flux coil is reduced from 100 Gauss to 20 Gauss. This is accomplished by decreasing the limiter coil charging voltage as well as the time delay when the flux coil fires. Doing this, the gyroradius increases from 4.5 cm to 22 cm.

	Case #1	Case #2
V_{Flux}	5.4 kV	5.4 kV
t_{Flux}	18 μs	12 μs
$V_{Limiter}$	1.3 kV	400 V
$t_{Limiter}$	5 μs	4 μs
V_{Plasma}	12 kV	12 kV
t_{Plasma}	9 μs	5 μs
B_0	100 Gauss	20 Gauss
ρ_i	4.5 cm	22 cm

Table 6.1: Standard (case 1) and alternative (case 2) formation schemes with their corresponding charging parameters.

The timing of the coils for the standard (dashed) and alternative (solid) formation schemes are shown in Fig. 6.21. The peak plasma current is just over 4 kA compared to 15 kA for the standard case. In addition, the peak magnetic field is about ±75 Gauss with lifetime of only 15 μs, compared to ±200 Gauss lasting 80 μs.

The radial magnetic field structure is shown in Fig. 6.22. As shown, the null surface moves outward throughout the lifetime of the FRC. This indicates that the external confining magnetic field is not strong enough to hold the plasma. Radial pressure balance (Chapter 7) is not satisfied because the plasma pressure nkT overwhelms the magnetic field pressure $B^2/2\mu_0$, resulting in the observed expanding ring.

The neutral flux measurements from the time-of-flight diagnostic are shown in the lower plot in Fig. 6.23. For comparison, the neutral flux measured from the standard formation scheme is shown in the upper plot. The contour levels are the same for both plots. The peak neutral flux is twice as large for the alternate case, which indicates that one or more terms (n_0,n_i, or v_i) in the expression for the emissivity (Eq. 2.25) has increased. Due to diagnostic limitations, a conclusion cannot be made about which terms increase. The interferometer was not available for density measurements when this test was performed. When the interferometer was available, measured line-integrated densities varied up to a factor of three when changing the charging parameters. In addition, there are no measurements of the neutral density so no strong conclusions can be made about which factors are playing a major role in the increase in neutral flux.

6.6 Summary

The plasma diagnostics on IFRC have been used to measure magnetic fields, plasma current, ion and electron temperature, electron density, and ion flow. Typical shots result in peak magnetic fields around ± 200 Gauss with a 15 kA peak plasma current that lasts about 80 μs. Observations of impurity lines show an ion flow in the range of 5-7 km/s. The neutral hydrogen temperature is about 10eV, and using the line ratio technique the electron temperature is 2-4 eV. Charge-exchange neutral particle analysis indicates that the average flow is less than the diagnostic's minimum energy cutoff (20 eV), which is consistent with the spectral measurements.

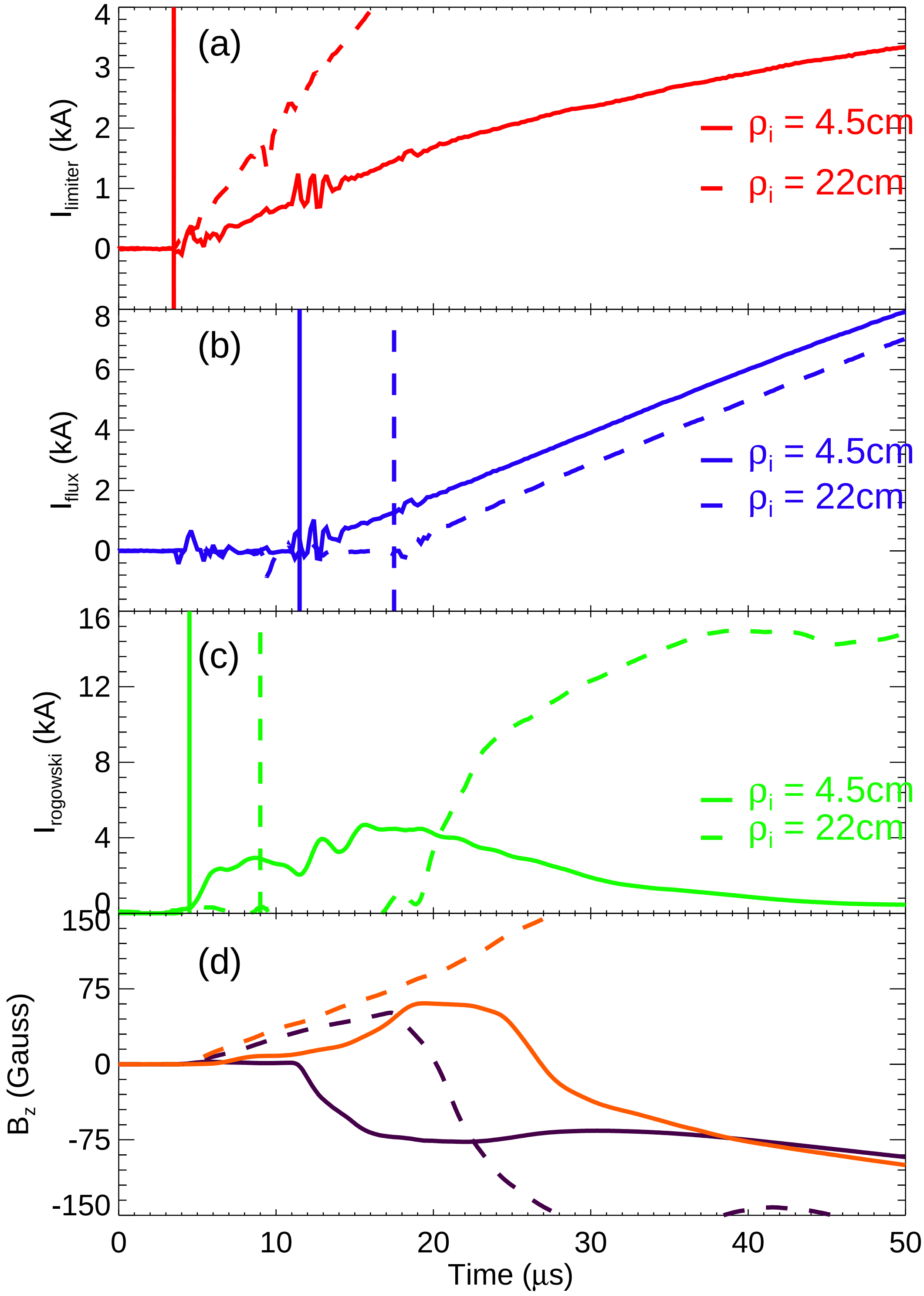

Figure 6.21: Comparison between standard formation (dashed) and formation with larger gyroradius (solid). Current through the limiter coil (a), flux coil (b), and total plasma current (c). Axial magnetic field at the midplane (d).

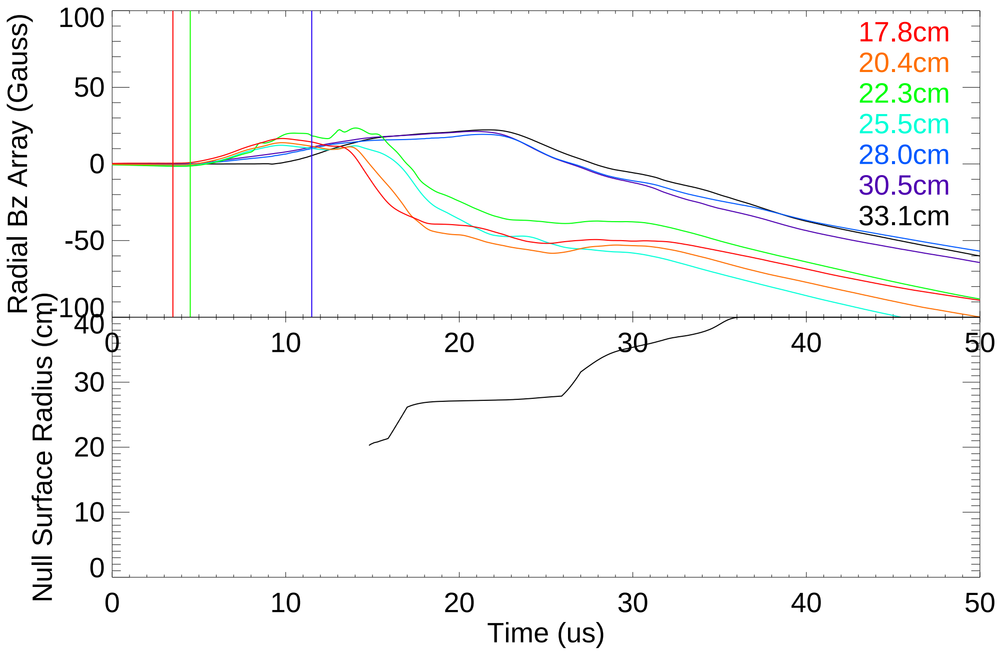

Figure 6.22: Radial variation of axial magnetic field at the midplane for alternative formation scheme (a). Interpolated null circle radius (b).

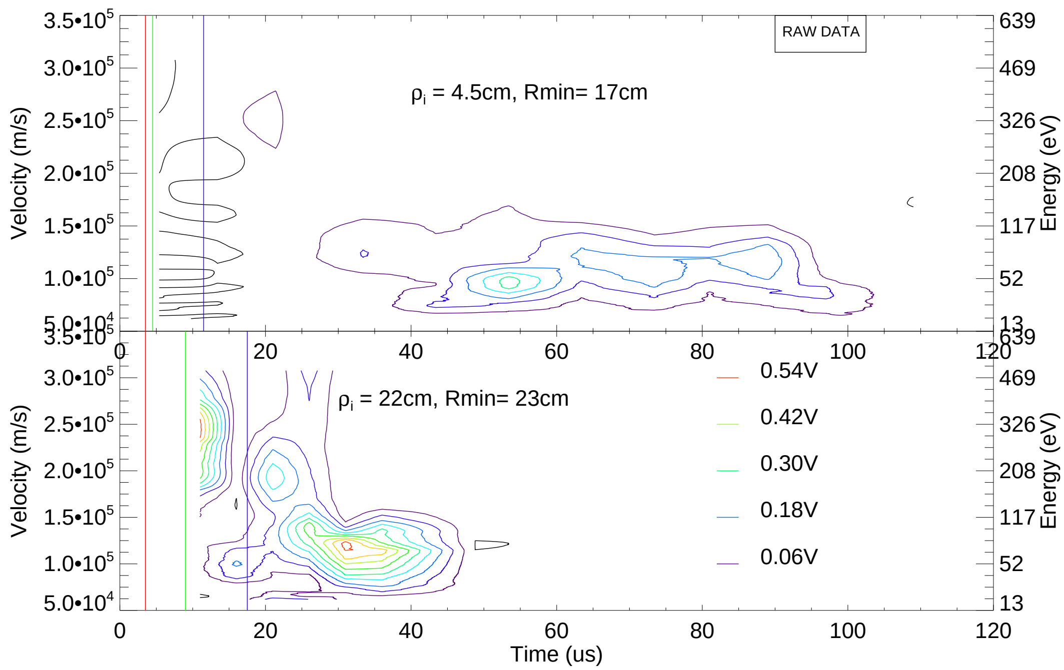

Figure 6.23: Neutral flux measurements from standard formation parameters (upper) and large gyroradius parameters (lower) .

Chapter 7

Ion Flow and Plasma Current Analysis

In this chapter the main goal of this work is presented, which is to compare the ion current as measured in the lab frame to the total plasma current. The ion current density J_i (in the lab frame) is calculated by

$$J_i(r, z, t) = q_i v_i(t) n_i(r, z, t) \tag{7.1}$$

where v_i is the average ion drift. The ion current I_i is found by integrating the current density over r and z

$$I_i(t) = \int_A J_i(r, z, t) dr dz. \tag{7.2}$$

Although the average drift velocity for impurities has been determined in Chapter 6, the ion density profile $n_i(r, z, t)$ is not directly measured (which can be accomplished using local density measurements with a Langmuir probe).

Once the ion current density has been determined, in order to make a valid comparison with the total plasma current the electron component must also be calculated. This is accomplished by considering the various drift orbits (described in Chapter 2). The drift velocities of these orbits are used in Eq. 7.1 for electrons and integrated to obtain their contribution to the current.

The following sections are arranged as follows. Section 7.1 provides calculations of the ion density profile using two methods: Sec. 7.1.1 uses pressure balance along with the magnetic probe data and Sec. 7.1.2 fits the magnetic fields from the theoretical equilibrium to the experimental data. The impurity drift measurements from Chapter 6 are discussed in Sec. 7.2 and related to the bulk ion drift velocity. The electron drift calculation is presented in Sec. 7.3. Section 7.4 contains the final analysis of the ion and electron current, and a comparison with the total plasma current from Chapter 6.

7.1 Ion Density Profile

7.1.1 Calculation Using Pressure Balance

The magnetic probe data from Chapter 6 has been used to construct the density distribution by using the pressure balance condition

$$\nabla(p + B^2/2\mu_0) = (B \cdot \nabla)B/\mu_0. \tag{7.3}$$

It should be noted that for the measured magnetic fields, the right hand side is within an order of magnitude of the left hand side of Eq. 7.3, so it cannot be approximated to zero as in other cases. As mentioned in Chapter 3, the magnetic probe array used for this calculation measures all three components of the magnetic field (B_r,B_θ, and B_z)

at 16 radial positions. The data is averaged over 5 shots, and the array is translated axially to obtain data at 12 different z-positions. Calculations are performed using IDL and are described below.

Looking at the radial component and integrating to obtain the density as a function of r and z gives

$$n(r,z) = \frac{1}{\mu_0 T}\left[\int \left(B_r \frac{\partial B_z}{\partial r} - \frac{B_\theta^2}{r}\right) dr - \frac{1}{2}\left(B_\theta^2 + B_z^2\right)\right] \tag{7.4}$$

where the temperature T is assumed to be constant throughout the plasma. The temperature is taken to be the average of the ion (∼8 eV) and electron (∼3 eV) temperature as measured using spectroscopy (from Chapter 6). The derivatives are computed using IDL's built in DERIV function, which performs numerical differentiation using 3-point, Lagrangian interpolation. The integral in Eq. 7.4 is calculated using the INT_TABULATED function in IDL, which uses a five-point Newton-Cotes integration formula. Since Eq. 7.4 contains a definite integral, and INT_TABULATED computes the indefinite integral between a specified interval, the following technique is employed:

1. Probe positions are designated by the subscript i at location r_i, where r_0 is the inner most probe.

2. Integration is performed over the interval $[r_0, r_i]$ giving the integral at r_i.

3. The probe position r_i is incremented.

4. Steps 2&3 are repeated until the final probe ($i = 16$) is reached.

Since an indefinite integral is only valid up to an arbitrary constant, the density profile obtained in this manner is scaled by choosing the density at the minimum point along

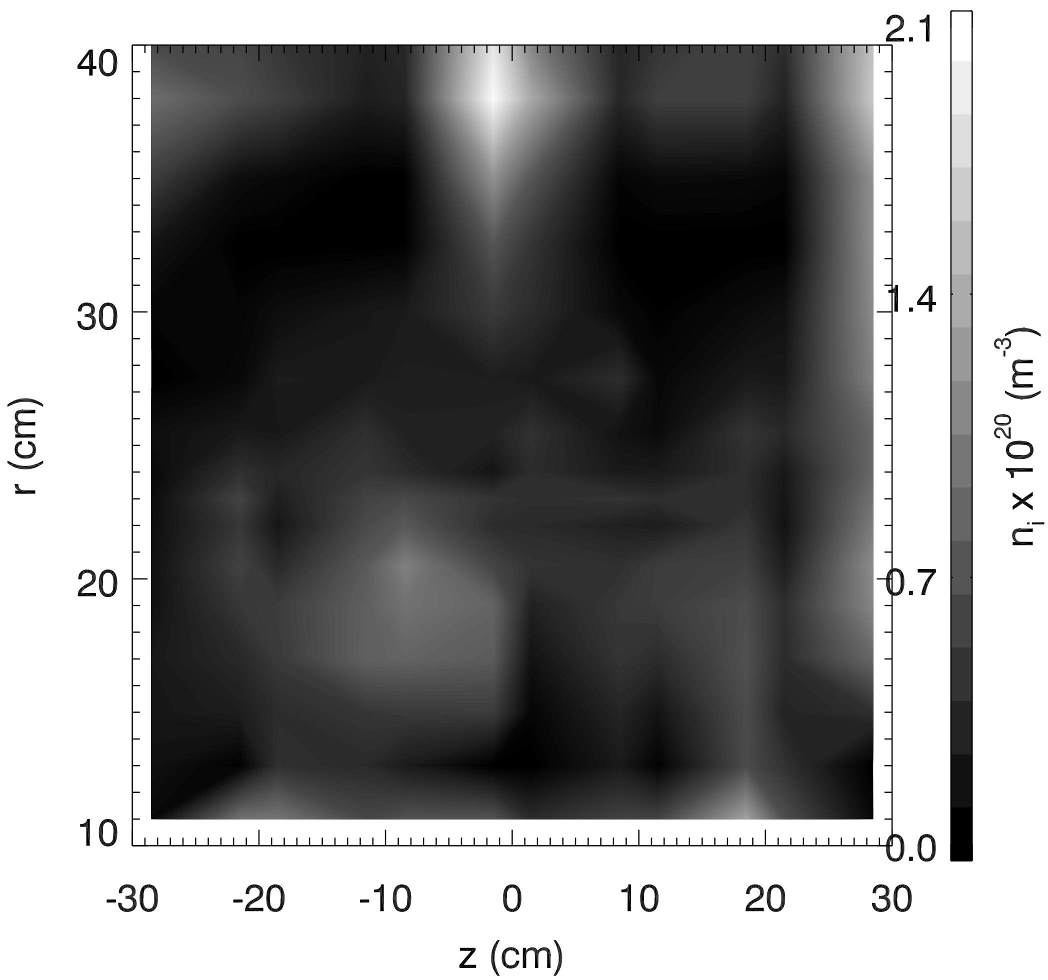

Figure 7.1: Density profile obtained from pressure balance at $t = 60\mu$s while plasma is stable.

each radius to be zero. Thus, a lower bound on the density is obtained using this method (Fig. 7.1). The density appears to increase at the radial boundaries using this method, which contradicts Langmuir probe measurements. This is presumably because the magnetic probe array is placed between the magnetic field coils, where stray fields are in the $\hat{r}$ direction. Looking at the first term of the integral in Eq. 7.4, it is clear that a non-zero B_r can increase the pressure using this method.

By applying the condition that the density goes to zero at the boundaries, the

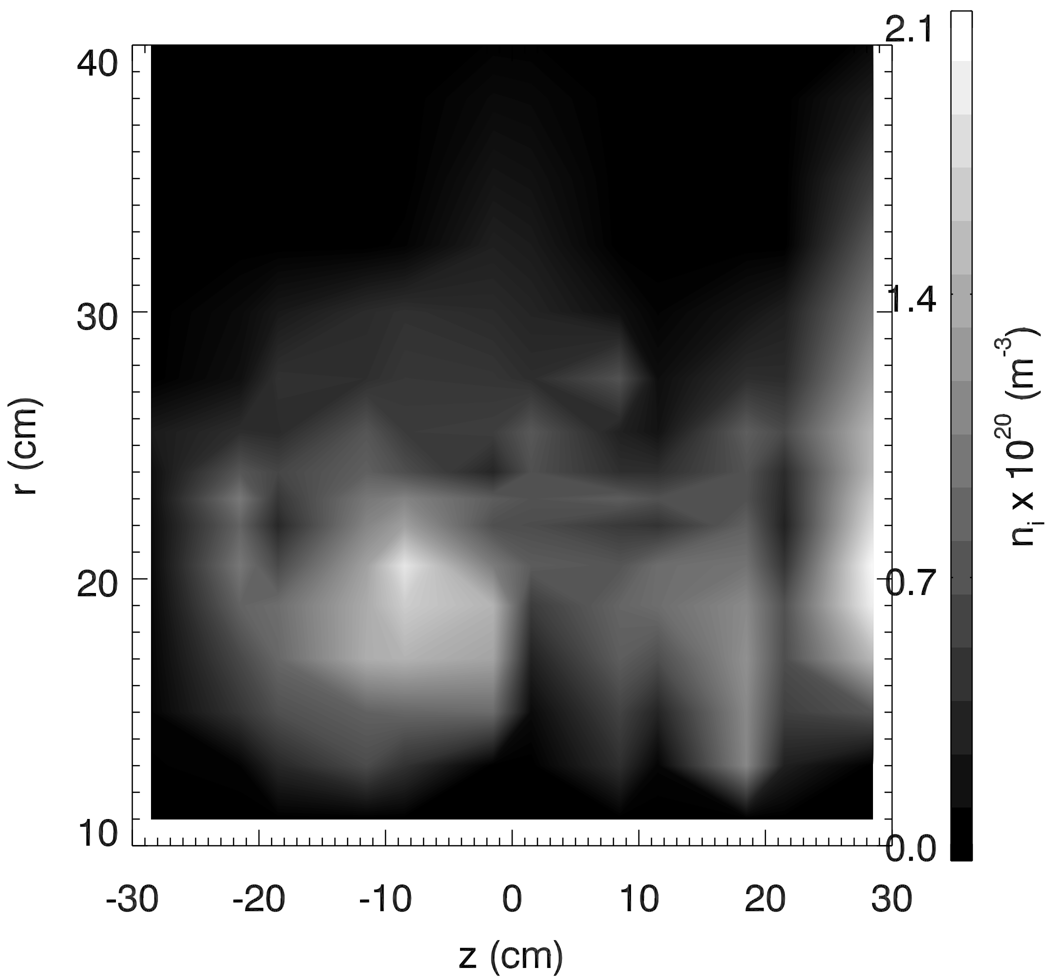

Figure 7.2: Density profile obtained from pressure balance at $t = 60\mu$s while plasma is stable with the condition that the density goes to zero at the boundary.

profile more closely resembles what has been measured by a Langmuir probe (shown in Sec. 7.1.2). The boundary condition is imposed by finding the local minimum between the outer boundary and the maximum point (at the null surface). The density profile is then linearly interpolated from the value at the minimum point to zero at the boundary. Figure 7.2 shows the density distribution with the imposed boundary condition during a stable portion of the discharge. As shown, the distribution is centered around $r \approx 20$ cm over the length of the plasma vessel. Integrating along the chord used by the second harmonic interferometer at $t = 60\ \mu$s (a stable portion of the discharge) results in a line integrated density of $1.1 \times 10^{17}\ cm^{-2}$. The interferometer measures $6.6 \times 10^{15}\ cm^{-2}$ during this time. This distribution is used in Sec. 7.4 for the calculation of the ion current.

7.1.2 Equilibrium Fitting

In Chapter 2, the rigid rotor distribution function,

$$f_j(r, z, \vec{v}) = \left(\frac{m_j}{2\pi T_j}\right)^{3/2} n_j(r, z) \exp\left\{-\frac{m_j}{2T_j}|\vec{v} - \vec{\omega_j} \times \vec{r}|^2\right\}, \tag{7.5}$$

was used to arrive at the equilibrium density and electromagnetic fields in an FRC by solving the Vlasov-Maxwell equations[7]. The physical interpretation of Eq. 7.5 is that the particles rotate uniformly with an angular frequency ω_j. The set of equations from the solution are

$$n_i(r) = \frac{n_{i0}}{\cosh^2\left(\frac{r-r_0}{r_0\Delta r}\right)}, \tag{7.6}$$

$$B_z(r) = -B_0\left[1 + \sqrt{\beta}\tanh\left(\frac{r^2 - r_0^2}{r_0\Delta r}\right)\right], \tag{7.7}$$

and

$$E_r(r) = -r\omega_e B_z(r) - \frac{T_e}{e}\frac{d\ln(n_e(r))}{dr} + \frac{m}{e}r\omega_e^2. \tag{7.8}$$

For a plasma described by the rigid rotor distribution in Eq. 7.5, the ion contribution to the total plasma current in the lab frame can be found provided that the ion density profile $n_i(r, z)$ and the rotation frequency ω_i are known. The calculations in this section assume that the ion density only depends on radius over a length Δz. Although Fig. 7.2 shows that the density profile has axial variation, the normalization (described below) is only possible at a single axial position (the midplane) due to limited data from the interferometer. Because of this, it is expected that this technique will result in an overestimation of the ion contribution to the total plasma current.

In equilibrium, the ion density's radial dependence for the 1-D case is given by Eq. 7.6. For the equilibrium model, B_0 refers to the applied magnetic field, which is not necessarily identical to the known initial background magnetic field from the limiter coil because some of the magnetic flux from this coil contributes to the trapped flux of the FRC. Not knowing exactly how much of this flux contributes is the motivation for treating B_0 as a free parameter. Since β is a function of B_0, it is also left as a free parameter. In this section, the density profile (Eq. 7.6) is calculated so that it can be used in Sec. 7.4 to determine the ion current. The fields resulting from the present calculation are used in Sec. 7.4 to calculate the electron drift orbits so that an estimate of the electron drift velocity can be obtained.

The key to specifying the functions in Eqs. 7.6-7.8 is to find the unknown quantities B_0, β, r_0, and Δr. This is accomplished by fitting the theoretical magnetic field profile (Eq. 7.7) to the $\hat{z}$ component of the radial magnetic probe array data and treating the unknowns as free parameters. Fitting is accomplished in IDL using MPFITFUN from the MPFIT library[51]. Performing a fit to the magnetic probe data in Fig. 6.2 at $t = 50$ μs, we find the parameter values to be $r_0 = 18$ cm and $\Delta r = 7$ cm. A fit at 40 μs is shown in Fig. 7.3.

Once r_0 and Δr are known, $n_i(r)$ can be radially integrated along the line of sight of the interferometer (from Fig. 6.1e). Setting the resulting integral equal to the line integrated data will provide the normalization constant n_0, which is the peak density at r_0. For the parameters above ($r_0 = 18$ cm and $\Delta r = 7$ cm) the unnormalized density profile is integrated and n_0 is calculated to be 1.4×10^{15} cm^{-3}. The resulting density profile is shown in Fig. 7.4 along with the density computed from pressure balance in Sec. 7.1.1. The data points are from a Langmuir probe;

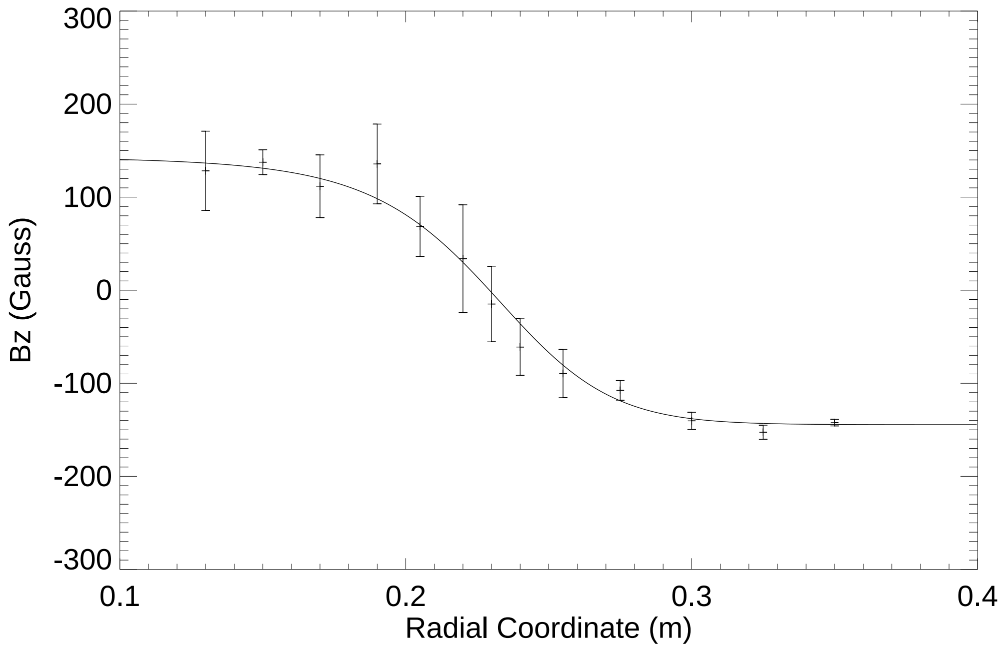

Figure 7.3: Equilibrium fit to data to obtain equilibrium parameters.

however, the peaks have been normalized to be between the two distributions for a comparison of the shapes of the distributions. As shown, the rigid rotor equilibrium profile is narrower than what is measured by the Langmuir probe as well as what is calculated from pressure balance. The peak is also larger in the rigid rotor profile. This is expected since the interferometer (which is used for normalizing the rigid rotor profile) sees the actual profile, which is broader. Accordingly, the peak must be larger to account for the same line integrated density. For the second harmonic interferometer (Chapter 6), the largest wavelength is 1064 nm which has a cutoff in a plasma with electron densities greater than 9.7×10^{20} cm^{-3}. Both computed density profiles are below this cutoff, indicating that the orders of magnitude are plausible.

The axial extent of the plasma Δz is estimated by finding the axial length of the last closed flux surface. This is accomplished by calculating where the separatrix is in r as a function of the axial coordinate z. To determine where the separatrix is,

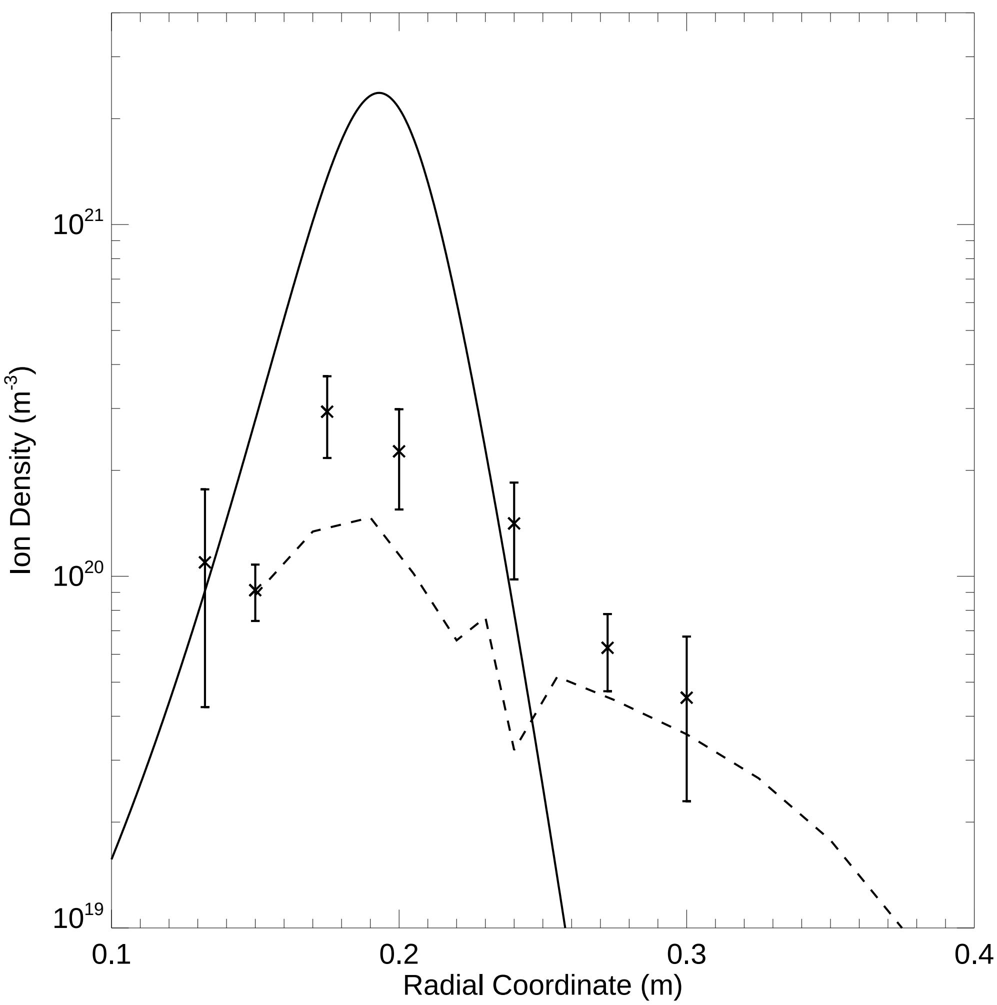

Figure 7.4: Equilibrium density profile using fitted parameters (solid) during a stable portion of the discharge ($t = 60\mu$s) along with profile calculated from pressure balance (dashed) and ion-saturation current ($\times$) scaled for reference.

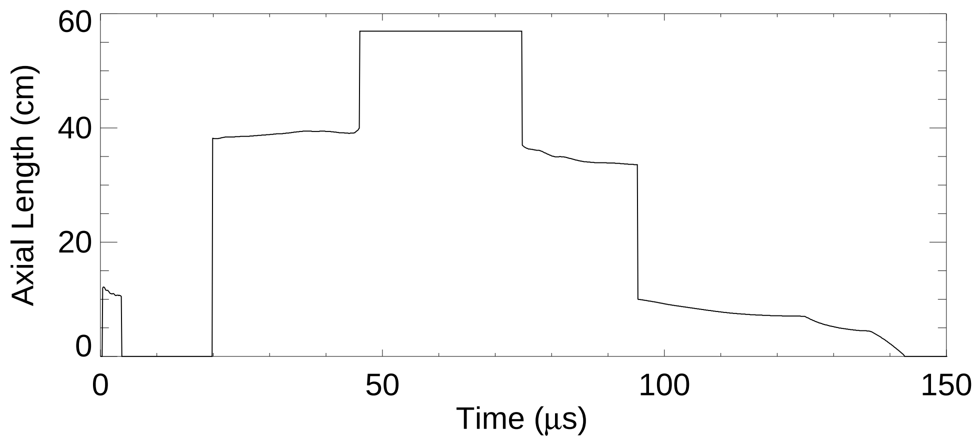

Figure 7.5: Axial length calculated from magnetic probe data.

the magnetic probe data from the radial array is integrated along r, and the net flux through a circle at radius r is calculated. Taking the flux along the outside of the flux coil to be zero, since the magnetic flux within the coil is not part of the trapped flux in the FRC, the separatrix is the radius at which the integral returns to zero. Numerically, this is accomplished by adding the successive integrals indexed by i

$$\Delta\Phi = \int \vec{B} \cdot d\vec{A} \approx \pi(r_i^2 - r_{i-1}^2)\frac{(B_i + B_{i-1})}{2} = \Delta\Phi_i. \tag{7.9}$$

For each interval between r_i and r_{i-1}, the average magnetic field is computed and multiplied by the area, giving a change in flux $\Delta\Phi$. The intervals are computed and each $\Delta\Phi_i$ is added to produce a total sum. When the sum returns to zero, the separatrix has been found. This process is repeated for all of the axial positions.

The separatrix radius equals the radius of the flux coil at two axial positions; we call the distance between these positions Δz. The time evolution of Δz is shown in Fig. 7.5. As shown, the axial extent is approximately 35 cm, except during the time interval between 45 and 75 μs. During this time interval the separatrix seems to extend past the confinement region between the two sets of plasma guns. The sharp rises and drops occur when the separatrix no longer returns to the flux coil at any point along the axis so 60 cm is used; 60 cm is the length of the confinement region, so it is used for the maximum allowable Δz. The "blocky" structure can be attributed to the fact that the data were taken over several shots, with shot to shot variation of the magnetic fields (up to 10%) as well as the fact that the radial integration is performed over a sparse grid with 3 cm spacing at the maximum radii, and 7 cm spacing at each end of the axis. It is not clear why this occurs, but using a different method by finding the axial position at which the magnetic field vector changes sign (when scanning radially) gives the same result.

7.2 Ion Flow

In Chapter 6, it was shown that there is an overall drift for the impurity ion species that peaks in the range of 5-7 km/s (Fig. 6.14). This is consistent with what is expected in a rigid rotor distribution- all species should rotate at the same velocity provided that the collisionality between them and the bulk plasma is sufficiently high compared to the lifetime of the plasma. When viewed from the opposite tangential direction, the resulting Doppler shift is in the opposite direction, as expected for a rotating plasma.

The Coulomb collisional relaxation time[65] for a stationary test particle to equilibrate with a rotating plasma has been calculated for the standard plasma condition in IFRC. For singly ionized carbon, the relaxation time is in the range of 2-8 μs for the plasma density between 100% and 25% of its peak value ($\sim 1.5 \times 10^{15}$ cm^{-3}, as determined in Sec. 7.1.2, and an ion temperature of 5 eV). Using the same plasma parameters, the relaxation time is in the range of 7-27 μs for singly ionized argon. For krypton, the relaxation time for the same parameters is 15-55 μs. The krypton estimate is consistent with the ~50 μs delay in acceleration relative to argon and carbon in Fig. 6.14. The same reasoning suggests that the argon acceleration should lag carbon; however, this is not observed. Possibly drag on the electron fluid also plays a role since the electron-ion collisionality is larger for smaller masses.

Neutral hydrogen spectroscopy, however, shows no Doppler shift. It is possible that this is due to a neutral density population that is sparse within the core of the plasma, and most dense on the edge. In this picture, the majority of light from hydrogen emission occurs at the edge (outside of the separatrix) where there is little or no rotation. Feasibility of this explanation is examined by considering the effective mean free path l_i for the ionization of hydrogen in a plasma. The average cross section $< \sigma v >$ for electron impact ionization of hydrogen as a function of electron temperature[18] can be used in conjunction with the electron density to estimate the mean free path, $\ell_i \simeq 1/n_e\sigma \simeq 3$ cm. Based on this analysis, the majority of neutrals will be ionized upon penetrating ~3 cm of the plasma and line radiation occurs primarily at the edge. Although neutral density measurements are not presently performed, if it is assumed to be 1% of the ion density ($n_i \sim 10^{14}$ cm^{-3}) then the mean free path is over 100 cm. This is consistent with the neutral particle analyzer since the few high energy ($>$ 20 eV) neutrals are able to make it to the detector. Meanwhile, the edge neutrals outside of the separatrix are not expected to rotate and bring the average velocity closer to zero. Similarly, ion-neutral collisions will not affect the flow for neutral densities in this range since an ion travelling at the measured drift velocity (~5 km/s) only travels ~50 cm over the lifetime of the discharge (<100 μs), which is less than the mean free path from above.

The helium neutrals appear to have an average drift in the same range of the impurities. The signal to noise ratio for the helium line, however, was at most ~2 during the stable portion of the discharge, resulting in poor Gaussian fitting and large error bars in determining the Doppler shift. In addition, the time response for the drift measured by helium appears to lag behind carbon and argon.

The data from the charge-exchange analyzer indicates that the peak neutral flux emitted from the plasma is below the 20 eV minimum measurable energy of the detector, resulting in the observed high energy tail. This is in agreement with the spectrometer since hydrogen, if rotating at 7 km/s like the impurities, has an energy of 0.25 eV. It is unclear whether the observed neutrals originate from the core or the edge. Previous experiments[62] show the electron temperature to be uniform across the radial extent of the plasma, and the ions are expected to have a similar profile due to high collisionality.

For the measured ion drift velocity v_i, the angular rotation frequency is $\omega_i = v_i/r$. Using this rotation frequency along with the computed density distribution function, the ion current in the lab frame is

$$I_i \simeq q\Delta z \omega_i \int n_i(r) r dr. \tag{7.10}$$

Integrating the density profiles obtained from Sec. 7.1.1&7.1.2 gives the dashed and solid traces in Fig. 7.6, respectively. The dotted trace is the total plasma current, shown for comparison. Although the peak density is higher for the fitted equilibrium density, the density profile from pressure balance integrates to a larger number since it is broader. From these current traces, it is observed that the ion contribution to the plasma current is at least an order of magnitude larger than the total current. In order for these numbers to be reasonable, the bulk electron motion must be in the same direction as the ions so that they subtract from the ion current. The electron drift is discussed in the following section.

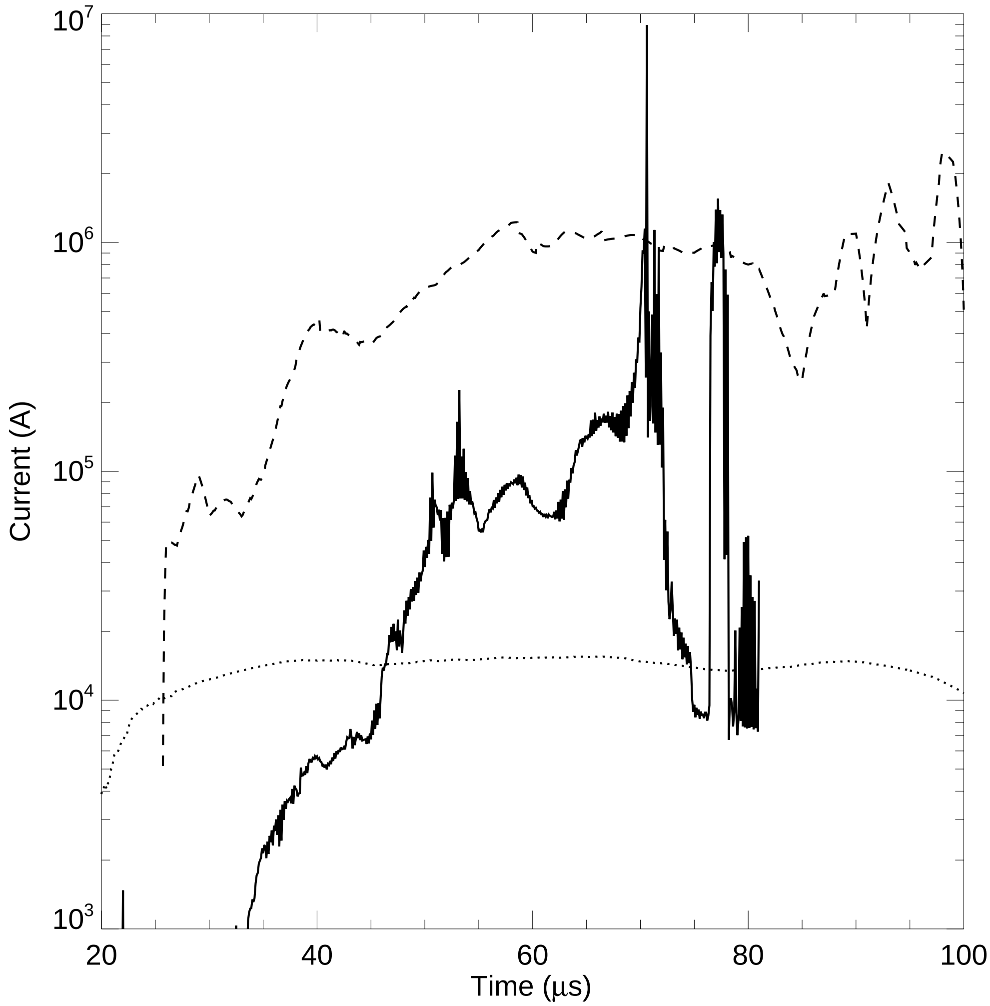

Figure 7.6: Ion currents using density profiles obtained from pressure balance (dashed) and fitting to the equilibrium model (solid). Total plasma current shown (dotted) for comparison.

7.3 Electron Flow

Although no direct electron flow measurements are made, it is possible to obtain a theoretical estimate. This is accomplished by considering the guiding center drifts for the orbits discussed in Chapter 2. The drifts are calculated using the theoretical equilibrium fields found in Chapter 6. The average electron rotation frequency ω_e is found by integrating radially over all possible electron drift velocities. It should be noted that in this analysis, no assumption has been made about whether ions or electrons are the main contributors to the current. The only assumption is that the equilibrium model is an accurate representation of the fields.

For a rigid rotor, the drift velocity v_e increases with radius r such that

$$\omega_e = \frac{v_e(r)}{r} = \text{constant}. \tag{7.11}$$

The drift velocity is just

$$v_e(r) = v_{E\times B}(r) + v_{\nabla B}(r) \tag{7.12}$$

where $v_{E\times B}(r)$ and $v_{\nabla B}(r)$ are from Eqs. 2.11&2.12. For $E_r(r)$ and $B_z(r)$ described in Sec. 7.1.2, both of these drifts are in the direction of the plasma current, which subtracts from the ion current. The average rotation frequency $<\omega_e>$ is found by integrating over all possible drift velocities and scaling by the normalized density

$$<\omega_e>= \frac{1}{\Delta r}\int_{r_{flux}}^{r_{lim}} \frac{n_e(r)}{n_0}\frac{v_d(r)}{r}dr. \tag{7.13}$$

In performing the integral in Eq. 7.13, there is a singularity where $r = r_0$ at the null surface. At this point, both of the guiding center drifts go to infinity as B_z approaches zero. These points are avoided in the integration by breaking the integral

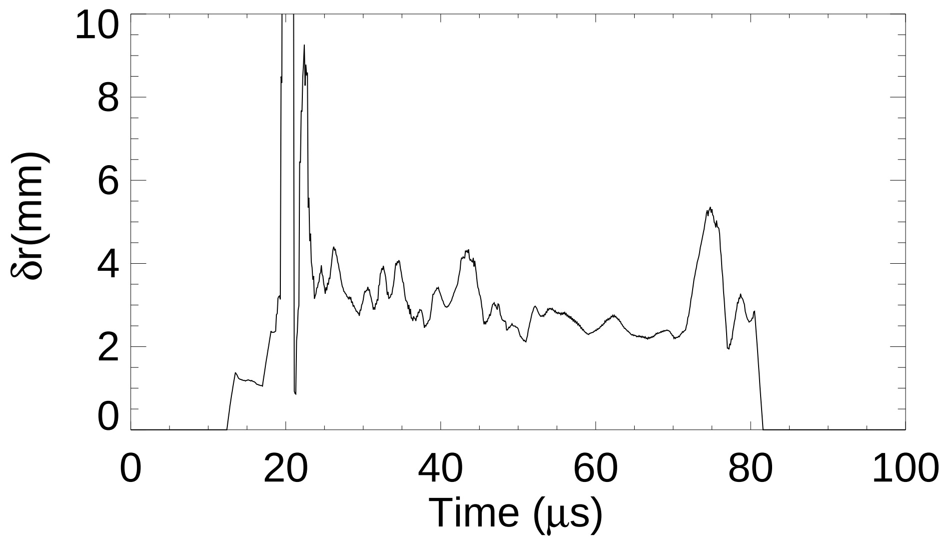

Figure 7.7: Electron betatron orbit boundary width.

up into two pieces:

$$\int_{r_{flux}}^{r_{lim}} \frac{n_e(r)}{n_0}\frac{v_d(r)}{r}dr \rightarrow \int_{r_{flux}}^{r_0-\delta r} \frac{n_e(r)}{n_0}\frac{v_d(r)}{r}dr + \int_{r_0+\delta r}^{r_{lim}} \frac{n_e(r)}{n_0}\frac{v_d(r)}{r}dr. \tag{7.14}$$

Here, δr is calculated such that the gyroradius evaluated at $r = r_0 \pm \delta r$ is less than δr. This requirement ensures that electrons at this radius do not cross the singularity in the integral. In addition, this is necessary because electrons within $\pm\delta r$ of the null surface will either be in betatron orbits, or the small sub-class of drift orbits called figure eight orbits. The time evolution of δr calculated from the equilibrium fields is shown in Fig. 7.7. Integrating the density distribution function over the same range

$$\int_{r_{flux}}^{r_{lim}} \frac{n_e(r)}{n_0}dr \rightarrow \int_{r_{flux}}^{r_0-\delta r} \frac{n_e(r)}{n_0}dr + \int_{r_0+\delta r}^{r_{lim}} \frac{n_e(r)}{n_0}dr. \tag{7.15}$$

indicates that $\sim$93% of the total number of electrons are included in the integral.

The above procedure describes the calculations used to estimate the electron drift,

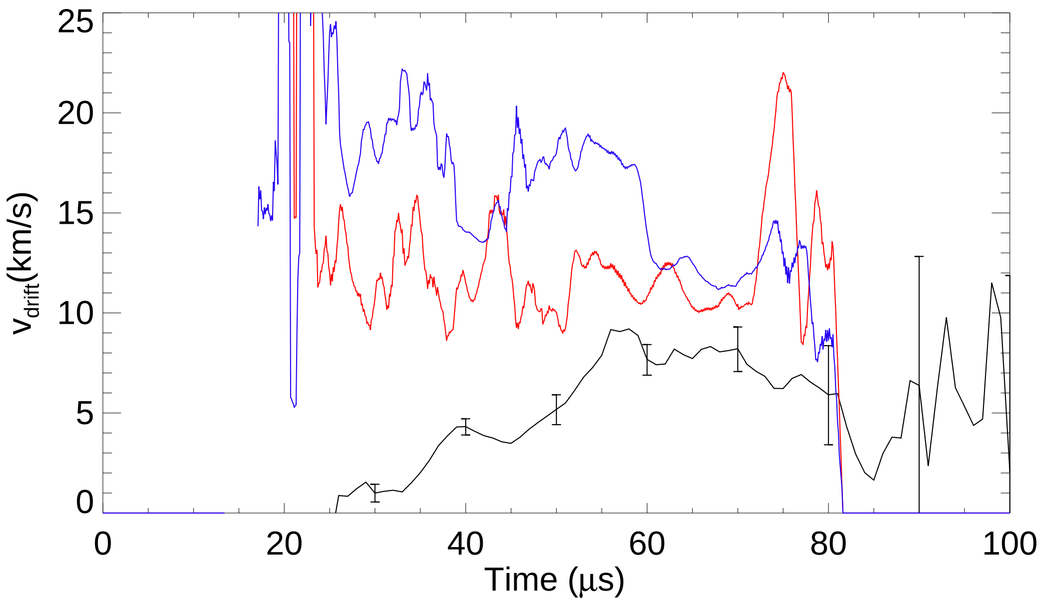

Figure 7.8: Electron drift velocity using density profiles calculated from pressure balance (blue) and from the theoretical equilibrium (red). The ion drift velocity is shown for comparison (black).

using the same density distribution for the electrons as for the ions. Figure 7.8 shows the electron drift velocities calculated by this method using the pressure balance density profile (blue) and the fitted equilibrium density profile (red). The ion drift velocity is shown for comparison (black). Taking the average of the two electron drift velocity calculations, the electron drift is less than twice the ion drift during 60-70 μs. This would indicate an electron dominant current in the opposite direction than what is measured.

A factor that was not taken into account in this analysis is the presence of electron betatron orbits. As mentioned in Chapter 2, betatron orbits are in the opposite direction of the drift orbits. Unfortunately, without knowing the velocities of these orbits it is difficult to accurately correct for this. An estimate can be made by assuming the average betatron velocity to be of the same order as the drift orbits

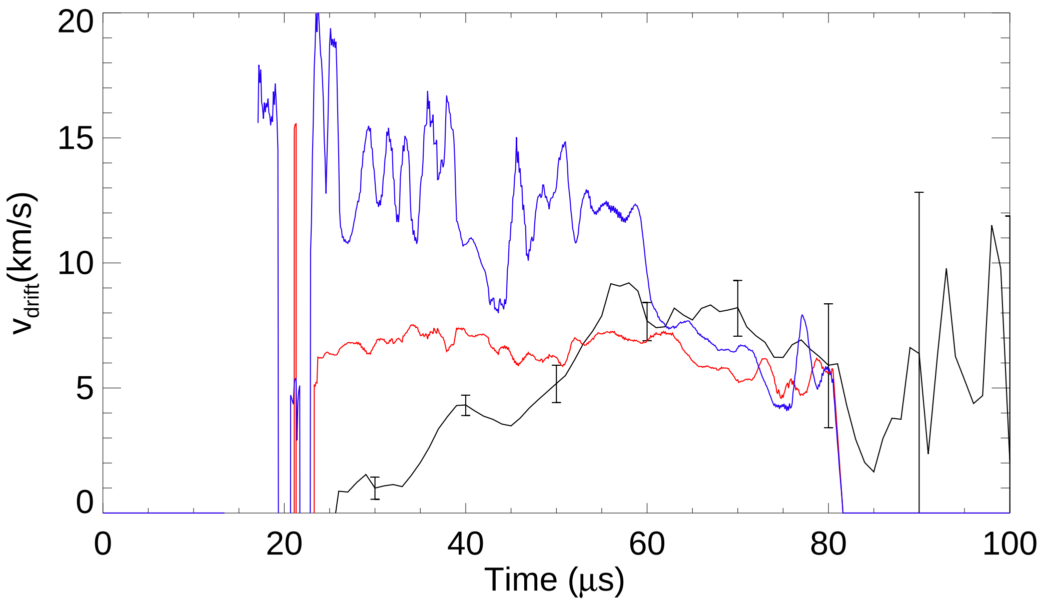

Figure 7.9: Electron drift velocity using density profiles calculated from pressure balance (blue) and from the theoretical equilibrium (red) including an estimate of the betatron orbit velocity to be 20 times larger than the average drift orbit velocity. The ion drift velocity is shown for comparison (black).

(which should be an underestimation). For this, the integral in Eq. 7.14 is modified to include the range (which was previously omitted) $[r_0 - \delta r, r_0 + \delta r]$. Performing the integral, however, results in average electron drift velocities that are virtually unchanged. The two reasons for this are that the fraction of the total population is small (∼7%) compared to the drift orbits, and that the drift velocity used is an underestimate. Modifying the betatron orbit velocity shows that these orbits must be ∼20 times faster than the drift orbits in order to lower the total electron drift velocity below the ion's (Fig.7.9). These calculations show that it is feasible that the average electron drift velocity is sufficiently high to reduce the ion current to the measured plasma current, without being so high as to reverse the direction of the current.

7.4 Plasma Current

The total current due to electrons and ions is

$$I_\theta = q(\omega_i - \omega_e) \int_{-\Delta z}^{\Delta z} \int_{r_{flux}}^{r_{lim}} n(r,z) r dr dz. \tag{7.16}$$

As shown in the previous section, the average electron drift velocity is comparable to the average ion drift velocity and depending on the actual betatron orbit velocity, results in either a positive or negative calculated current. For comparisons, it is useful to express the electron and ion current components in terms of their rotation frequencies, as in Eq. 7.16. Using the measured total current from the Rogowski coil and ω_i from the Doppler shift measurements, the different density profiles can be integrated to obtain an expected ω_e. These along with $< \omega_e >$ calculated from particle drifts are shown in Fig. 7.10. The plotted range is restricted to the time in the discharge during which the FRC is the most stable (axial magnetic probes and plasma current are flat). As shown, the rotation frequencies required to provide the measured plasma current are within an order of magnitude of the average rotation frequency calculated from the electron drift orbits.

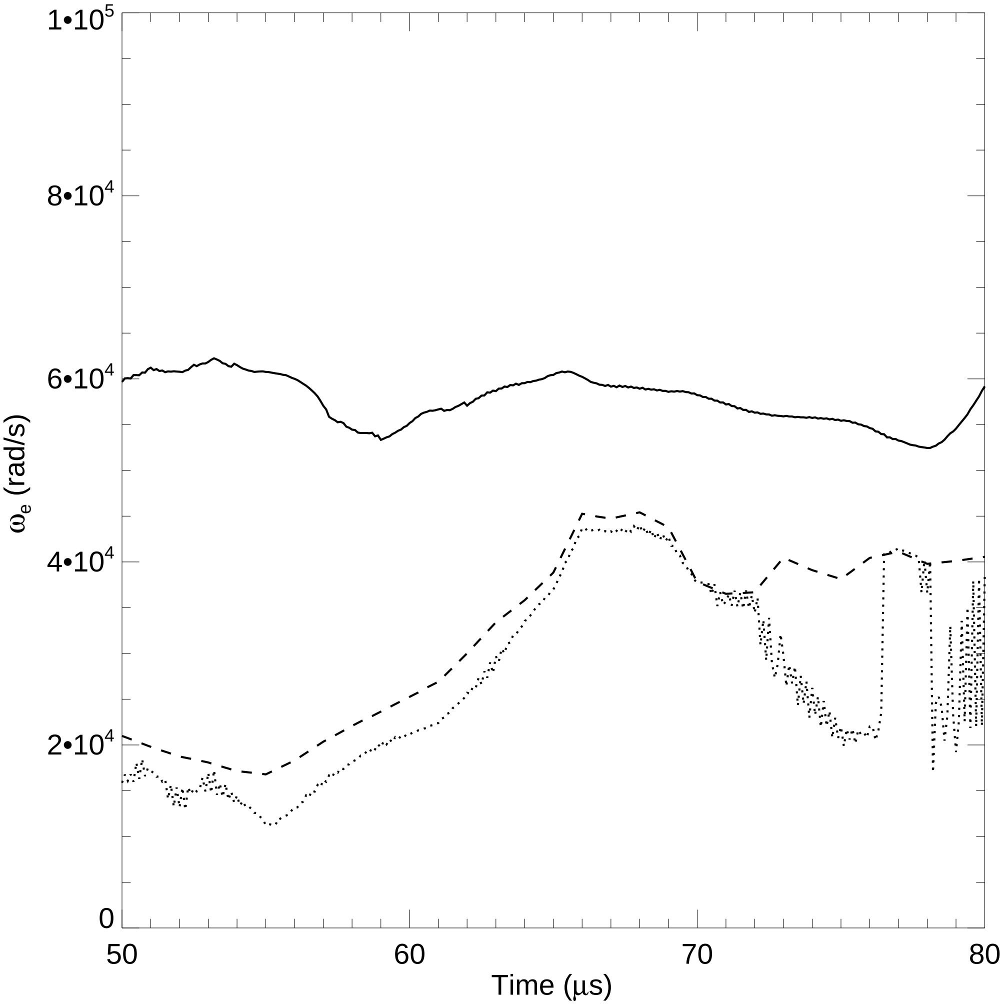

Figure 7.10: Electron rotation frequencies calculated from particle drifts (solid) and using the integrated density distributions obtained from the equilibrium model fit (dotted) and pressure balance (dashed).

Chapter 8

Conclusions

8.1 Summary

Many diagnostic tools have been developed for use on IFRC. Magnetic probe arrays are used for mapping the magnetic field structure. A Rogowski coil is used for measuring the total plasma current. A charge-exchange neutral particle analyzer measures the emission from the plasma. Visible emission from the plasma is used to measure Doppler broadening and shifts using a spectrometer.

For a typical discharge, the magnetic fields peak around ±200 Gauss and reversal lasts for about 80 μs. Peak plasma currents are typically 15 kA and stay relatively flat for about 60 μs. CII, ArII, and KrII show a Doppler shift resulting in a 5-7 km/s flow in the ion diamagnetic direction. Collisionality between the observed ions and the hydrogen plasma is high enough to assert that the hydrogen ions are rotating in the same direction. The flow of hydrogen is not observed through spectroscopy because the neutral emission occurs at the edge of the plasma, where there is little or no rotation. The neutral particle analyzer did not detect flow because the minimum detectable energy of the diagnostic is higher than the average drift. The electron temperature is calculated to be around 3 eV using the line ratio technique. Neutral hydrogen and helium temperature measurements give 10 eV, while the observed ion lines result in a 50-100 eV energy spread.

Fitting a theoretical equilibrium to experimental data has allowed unknown parameters in the model to be estimated. The ion density from this model is then used to calculate the ion contribution to the total current. An alternative ion density calculation is made using the pressure balance condition, and the ion current calculation is repeated. For these two methods, the ion current in the lab frame is between one and two orders of magnitude higher than the measured total plasma current. Based on these findings, it must follow that the electrons are drifting in the same direction as the ions in order to subtract from the net current.

Using the equilibrium fields from the theoretical model, the electron drift orbits have been used to calculate the average electron drift velocity. This drift velocity is high enough to reduce the ion component of the total current to a level below what is actually measured. Calculating the electron rotation frequency necessary to reduce the ion current to the level of the measured total current gives a result that is within a factor of three of the rotation frequency calculated from the drift orbits estimated from the equilibrium fields.

8.2 Future Work

Although IFRC has come a long way over the past few years, there is still a lot more that needs to be done in order to fully characterize the plasma. At this point, the equilibrium magnetic fields are well understood; for what is not understood (magnetic fluctuations), the data is present at least. Temperature measurements for ions and electrons can be obtained using the spectrometer. For the overall characterization of IFRC, further density measurements need to be performed. Although the density can be inferred from the magnetic field profile using pressure balance as in Chapter 7, this technique assumes the plasma is in equilibrium (force balance) and an uncertainty is introduced from the integration constant as well as the stray magnetic fields near the coils. The Langmuir probe used for the density profile comparisons gives reasonable data, however it does not seem to work 100% of the time.

The analysis performed in this paper is heavily dependent on the plasma being a rigid rotor distribution and knowing the plasma density profile. Further verification of the findings require more measurements of the density profile both radially, and along the axis of the FRC. Additionally, local measurements of the plasma flow can test the validity of the rigid rotor model for IFRC. A gridded energy analyzer is presently in development for this purpose. Spectral measurements at different axial positions can also be used to check the validity of the assumption that the drift velocity is uniform along the axis.

Presently, the electron drifts have been calculated using the theoretical radial electric field. Measurements of the radial electric field will provide a useful comparison between the theoretical drifts and what they actually are. Additionally, the ion energy analyzer that is in development might be useful for measuring the electron energy distribution. This data could be compared with the expected flows based on the calculated average drift orbit velocity.

With either a reliable density diagnostic or a method of measuring the electron flow, the following experiment can be performed. By accurately characterizing the ion (and/or electron) current density in addition to knowing the total plasma current, the effect of forming the FRC with lower initial magnetic field can be studied in more detail. With a lower initial magnetic field, the ions are not magnetized and should be easier to accelerate by the toroidal electric field induced by the flux coil. Data for testing this was briefly discussed in Chapter 6, which demonstrated an increase in neutral particle emission for an alternative formation scheme.

Bibliography

[1] G.P. Thomson and M. Blackman. Improvements in or relating to gas discharge apparatus for producing thermonuclear reactions. *British Patent, 817,681*, 1946.

[2] A.C. Kolb, C.B. Dobbie, and H.R. Griem. Field mixing and associated neutron production in a plasma. *Physical Review Letters*, 3(1):5, 1959.

[3] M. Tuszewski. Field reversed configurations. *Nuclear Fusion*, 28(11):2033, 1988.

[4] M.W. Binderbauer and N. Rostoker. Turbulent transport in magnetic confinement: how to avoid it. *Journal of Plasma Physics*, 56(03):451, 1996.

[5] A. Necas. *Electrostatic Current Drive for a Field Reversed Configuration*. PhD thesis, University of California, Irvine, 2007.

[6] A. Qerushi. *Particle and Energy Transport in a Field Reversed Configuration*. PhD thesis, University of Florida, 2000.

[7] N. Rostoker and A. Qerushi. Equilibrium of field reversed configurations with rotation. I. One space dimension and one type of ion. *Physics of Plasmas*, 9(7):3057, 2002.

[8] M. Tuszewski, D.P. Taggart, R.E. Chrien, D.J. Rej, R.E. Siemon, and B.L. Wright. Axial dynamics in field-reversed theta pinches. II: Stability. *Physics of Fluids B, Plasma Physics*, 3(10):2856, 1991.

[9] N.A. Rosenbluth and M.N. Bussac. MHD stability of spheromak. *Nuclear Fusion*, 19(4):489, 1979.

[10] H.A.B. Bodin and A.A. Newton. Rotational instability in the theta pinch. *The Physics of Fluids*, 6(9):1338, 1963.

[11] S. Ohi, Y. Kawakami, M. Tanjyo, S. Okada, Y. Ito, M. Kako, S. Gotô, T. Ishimura, and H. Itô. Quadrupole stabilization of the $n = 2$ rotational instability of a field-reversed theta-pinch plasma. *Physical Review Letters*, 51(12):1042, 1983.

[12] T.P. Intrator, J.Y. Park, J.H. Degnan, I. Furno, C. Grabowski, S.C. Hsu, E.L. Rudin, P.G. Sanchez, J.M. Taccetti, M. Tuszewski, W.J. Waganaar, G.A. Wurden, and S.Y. Zhang. A high density field reversed configuration plasma for magnetized target fusion. In *Invited Talks from ICOPS 2003*, 2003.

[13] W.N. Hugrass, I.R. Jones, K.F. McKenna, M.G.R. Phillips, R.G. Storer, and H. Tuczek. Compact torus configuration generated by a rotating magnetic field: The rotamak. *Physical Review Letters*, 44(25):1676, 1980.

[14] J.T. Slough and K.E. Miller. Enhanced confinement and stability of a field-reversed configuration with rotating magnetic field current drive. *Physical Review Letters*, 85(7):1444, 2000.

[15] Y. Ono, A. Morita, M. Katsurai, and M. Yamada. Experimental investigation of three-dimensional magnetic reconnection by use of two colliding spheromaks. *Nuclear Fusion*, 43:649, 1993.

[16] Y. Ono, T. Matsuyama, K. Umeda, and E. Kawamori. Spontaneous and artificial generation of sheared-flow in oblate FRCs in TS-3 and 4 FRC experiments. *Nuclear Fusion*, 43:649, 2003.

[17] W.F. Pierce, R.J. Maqueda, R.D. Brooks, and R. Farengo. Initial results from parallel coil operation of the coaxial slow source field reversed configuration device. *Nuclear Fusion*, 33(1):117, 1993.

[18] R.J. Goldston and P.H. Rutherford. *Introduction to Plasma Physics*. Institute of Physics Publishing, 1995.

[19] Y. Zhang, H. Boehmer, W.W. Heidbrink, R. McWilliams, D. Leneman, and S. Vincena. Lithium ion sources for investigations of fast ion transport in magnetized plasmas. *Review of Scientific Instruments*, 78:013302, 2007.

[20] G. Fiksel, D.J. Den Hartog, and P.W. Fontana. An optical probe for local measurements of fast plasma ion dynamics. *Review of Scientific Instruments*, 69(5):2024, 1998.

[21] M. Hudis and L.M. Lidsky. Directional langmuir probe. *Journal of Applied Physics*, 41(12):5011, 1970.

[22] P.C. Strangeby. Measuring plasma drift velocities in tokamak edge plasmas using probes. *Physics of Fluids*, 27(11):2699, 1984.

[23] I.H. Hutchinson. A fluid theory of ion collection by probes in strong magnetic fields with plasma flow. *Physics of Fluids*, 30(12):3777, 1987.

[24] I.H. Hutchinson. The invalidity of a mach probe model. *Physics of Plasmas*, 9(5):1832, 2002.

[25] I.H. Hutchinson. *Principles of Plasma Diagnostics*. Cambridge University Press, 1987.

[26] P. Beiersdorfer, A.L. Roquemore, and R. Kaita. Characteristics of compact solid-target charge exchange analyzers for energetic ion diagnostics on tokamaks. *Review of Scientific Instruments*, 11:2092, 1987.

[27] H.P. Eubank and T.D. Wilkerson. Ion energy analyzer for plasma measurements. *Review of Scientific Instruments*, 34(1):12, 1963.

[28] S.S. Medley, A.J.H. Donné, R. Kaita, A.I. Kislyakov, and A.L. Roquemore. Contemporary instrumentation and application of charge exchange paricle diagnostics in magnetic fusion experiments. *Review of Scientific Instruments*, 79:011101, 2008.

[29] R.E. Siemon, W.T. Armstrong, D.C. Barnes, R.R. Bartsch, R.E. Chrien, J.C. Cochrane, W.N. Hugrass, R.W. Kewish, Jr., P.L. Klinger, H.R. Lewis, R.K. Linford, McKenna K.F., R.D. Milroy, D.J. Rej, J.L. Schwarzmeier, C.E. Seyler, E.G. Sherwood, R.L. Spencer, and M. Tuszewski. Review of the los alamos FRX-C experiment. *Fusion Technology*, 9:13, 1986.

[30] C.D. Cothran, J. Fung, M.R. Brown, M.J. Schaffer, and E. Belova. Spectroscopic flow and ion temperature studies of a large s FRC. *Journal of Fusion Energy*, 26(1/2):37, 2007.

[31] Z.A. Pietrzyk, G.C. Vlases, R.D. Brooks, K.D. Hahn, and R. Raman. The coaxial slow source FRC device. *Nuclear Fusion*, 27(9):1478, 1987.

[32] http://www.bitscope.com.

[33] A. Van Drie. Lab 2000.

[34] F. Brandi and F. Giammanco. Harmonic interferometry in the visible and UV, based on second- and third-harmonic generation of a 25 ps mode-locked Nd:YAG laser. *Optics Letters*, 33(18):2071, 2008.

[35] L. Oksuz and N. Hershkowitz. Understanding mach probes and langmuir probes in a drifting, unmagnetized, non-uniform plasma. *Plasma Sources Science and Technology*, 13:263, 2004.

[36] D.E. Voss and S.A. Cohen. Low-energy neutral atom spectrometer. *Review of Scientific Instruments*, 53(11):1696, 1982.

[37] H. Verbeek. A low-energy neutral particle analyzer for plasma experiments. *Journal of Physics E: Scientific Instruments*, 19:964, 1986.

[38] R.L. Boivin, M. Koltonyuk, C.P. Munson, and R.M. Mayo. Time-of-flight neutral particle analyzer for Alcator C-Mod. *Review of Scientific Instruments*, 68(1):982, 1997.

[39] N.R. Ray. A time-of-flight low-energy analyzer (TOFLEA) of neutral atoms. *Journal of Physics D: Applied Physics*, 31:1071, 1998.

[40] B.L. Peko and T.M. Stephen. Absolute detection efficiencies of low energy H, H^-, H^+, H_2^+, and H_3^+ incident on a multichannel plate detector. *Nucl. Instr. and Meth. in Phys. Res. B*, 171:597–604, 2000.

[41] D.E. Voss and S.A. Cohen. UHV compatible chopper system. *Journal of Vacuum Science Technology*, 17(1):303, 1980.

[42] H. Suno and T. Kato. Cross section database for carbon atoms and ions: Electron-impact ionization, excitation, and charge exchange in collisions with hydrogen atoms. *Atomic Data and Nuclear Data Tables*, 92:407–455, 2006.

[43] W.L. Fite, A.C.H. Smith, and R.F. Stebbings. Charge transfer in collisions involving symmetric and asymmetric resonance. *Proc. Roy. Soc. London Ser. A*, 268(1335):527, 1962.

[44] T. van Roon. Servo pulser. http://www.uoguelph.ca/antoon/gadgets/servo3.htm.

[45] Channeltron electron multiplier handbook for mass spectrometry applications. Galileo Electro-Optics, Sturbridge, MA, 1991.

[46] R.A. Capobianco. Xenon: The full spectrum vs. deuterium plus tungsten. PerkinElmer, Inc. Application Notes.

[47] http://www.edmundoptics.com/onlinecatalog/displayproduct.cfm?productid=1904.

[48] J.A. Alcalay and E.L. Knuth. Molecular-beam time-of-flight spectroscopy. *Review of Scientific Instruments*, 40(3):438, 1969.

[49] http://en.wikipedia.org/wiki/monochromator.

[50] J.M. Lerner and A. Thevenon. The optics of spectroscopy - a tutorial.

[51] http://cow.physics.wisc.edu/ craigm/idl/idl.html.

[52] R.E. Vermillion. Doppler broadening due to cyclotron motion in a uniform magnetic field. *American Journal of Physics*, 51(3):237, 1983.

[53] T. Fujimoto. *Plasma Spectroscopy*. Oxford Science Publications, 2004.

[54] H.R. Griem. *Spectral Line Broadening By Plasmas*. Academic Press, 1974.

[55] G. Baym. *Lectures on Quantum Mechanics*. The Benjamin/Cummings Publishing Company, 1973.

[56] H. Ehrich and D.E. Kelleher. Experimental investigation of plasma-broadened hydrogen balmer lines at low electron densities. *Physical Review A*, 21(1):319, 1980.

[57] H.R. Griem, M. Baranger, A.C. Kolb, and Oertel G. Stark broadening of neutral helium lines in a plasma. *Physical Review*, 125(1):177, 1962.

[58] A. Srećković, V. Drinčić, S. Bukvić, and S. Djeniže. Stark broadening parameters in CII, CIII and CIV spectra. *Journal of Physics B: Atomic, Molecular and Optical Physics*, 33:4873, 2000.

[59] N. Konjević, J. Labat, Lj. Ćirković, and J. Purić. Measurement of the stark broadening parameters of some singly ionized argon lines. *Zeitschrift fur Physik*, 235:35, 1970.

[60] J. Purić, S. Djeniže, J. Labat, A. Srećković, and M. Platiša. Stark broadening regularities within successive ionization stages in krypton and xenon. *Contributions to Plasma Physics*, 31(1):63, 1991.

[61] A.S. Alhasi and J.A. Elliot. Determination of electron temperature from the emissivity ratio in the UMIST quadrupole GOLUX. *Plasma Physics and Controlled Fusion*, 34:947, 1992.

[62] D.J. Rej and W.T. Armstrong. Electron temperature measurements in the field-reversed configuration experiment FRX-C. *Nuclear Fusion*, 24:177, 1984.

[63] W. Lotz. An empirical formula for the electron-impact ionization cross-section. *Zeitschrift fur Physik*, 206:205, 1967.

[64] J.B. Boffard, B. Chiaro, T. Weber, and C.C. Lin. Electron-impact excitation of argon: Optical emission cross sections in the range of 300-2500 nm. *Atomic Data and Nuclear Data Tables*, 93:831, 2007.

[65] J.D. Huba. *NRL Plasma Formulary.* Naval Research Laboratory, Washington, DC, 2007.

Appendices

A IFRC Plasma Parameters

Source	Flux Coil	Limiter Coil	Plasma Guns
Inductance (μH)	19	3.1	-
Capacitance (μF)	258	2200	50
Voltage (kV)	5.4	1.3	16
Current (kA)	14	17	1.3

Table A.1: IFRC machine characteristics.

n_e	$10^{15} cm^{-3}$	ω_{ce}	$3.5 \times 10^9 rad/s$
n_i	$10^{15} cm^{-3}$	ω_{ci}	$1.9 \times 10^6 rad/s$
T_e	3eV	v_{te}	$7.3 \times 10^5 m/s$
T_i	10eV	v_{ti}	$3.0 \times 10^4 m/s$
B_z	200 Gauss	r_{Le}	$0.2 mm$
β	0.1	r_{Li}	$1.6 cm$
ω_{pe}	$1.8 \times 10^{11} rad/s$	ω_{pi}	$4.2 \times 10^9 rad/s$

Table A.2: Nominal plasma parameters using the maximum values for B_z and $n_{e,i}$ (neglecting the radial dependence).

B Data and IDL Programs

The following table summarizes the figures containing data from IFRC. The IDL program and the data files used are also listed.

Figure	Figure Filename	IDL Program	Data Used
2.2	TypEquil.ps	plots.pro	FRCequilibrium_1.1.dat
5.7	gaussfit_bw.ps	GaussFitShot.pro	ProcessedSpectraHI1.2.1.dat
5.8	hlampfit.ps	Hlamp.pro	30um_ARRAY_10.csv, R5900Uuniformity.csv, tempwavelengths.csv, background.csv
6.1	Case1bw2.ps	frc_plots.pro	NEW_rogowski.dat, Currents0.dat, Axials0.dat, density.dat
6.2	RadialCase1bw.ps	frc_plots.pro	newbz.dat
6.3	timescaleData.eps	uvplots.nb	neutralpulses.csv
6.4	C1distcor_col.ps	TOF_DATA.pro	scan_corrected21.dat, scan21.dat
6.5	C1R17a.ps	TOF_DATA.pro	scan21.dat
6.6	C1R17ca.ps	TOF_DATA.pro	scan_corrected21.dat
6.7	C1radial.ps	TOF_DATA.pro	scan24.dat, scan20.dat, scan23.dat, scan22.dat, scan21.dat
6.8	TOFgaussbw.ps	TOF_DATA.pro	scan_corrected23.dat, scan_corrected26.dat
6.9	lineratiotempbw.ps	LineRatio.pro	LineRatioTemp.dat
6.10	intensity.ps	frc_spectra.pro	ProcessedSpectraKrII1.2.1.dat, ProcessedSpectraArII1.2.1.dat, ProcessedSpectraCII1.2.1.dat, ProcessedSpectraHeI1.2.1.dat, ProcessedSpectraHI1.2.1.dat
6.11	HEmiss.ps	emissivity.pro	density.dat, ProcessedSpectraHI1.2.1.dat
6.12	ArEmiss.ps	emissivity.pro	FRCequilibrium_1.dat, LineRatioTemp.dat, ProcessedSpectraArII1.2.1.dat

Table B.3: Figures and associated filenames and IDL programs

Figure	Figure Filename	IDL Program	Data Used
6.13	argonsides2.eps	ArDriftFig.pro	ProcessedSpectraArII1.2.1.dat
6.14	driftbw2.ps	AllDrifts.pro	ProcessedSpectraKrII1.2.1.dat, ProcessedSpectraArII1.2.1.dat, ProcessedSpectraCII1.2.1.dat, ProcessedSpectraHeI1.2.1.dat, ProcessedSpectraHI1.2.1.dat
6.15	temperaturebw2.ps	AllTemps.pro	ProcessedSpectraKrII1.2.1.dat, ProcessedSpectraArII1.2.1.dat, ProcessedSpectraCII1.2.1.dat, ProcessedSpectraHeI1.2.1.dat, ProcessedSpectraHI1.2.1.dat
6.17	TempFluxTime.ps	ArFluxScan.pro	ProcessedSpectraArII1.2.1.dat, ProcessedSpectraArII3.2.1.dat, ProcessedSpectraArII5.2.1.dat, ProcessedSpectraArII6.2.1.dat, ProcessedSpectraArII7.2.1.dat
6.18	TempFlux.ps	ArFluxScan.pro	ProcessedSpectraArII1.2.1.dat, ProcessedSpectraArII3.2.1.dat, ProcessedSpectraArII5.2.1.dat, ProcessedSpectraArII6.2.1.dat, ProcessedSpectraArII7.2.1.dat
6.19	TempPlasmaTime.ps	ArPlasScan.pro	ProcessedSpectraArII4.dat, ProcessedSpectraArII3.dat, ProcessedSpectraArII8.dat
6.20	TempPlasma.ps	ArPlasScan.pro	ProcessedSpectraArII4.dat, ProcessedSpectraArII3.dat, ProcessedSpectraArII8.dat
6.21	case2.eps	frc_plots.pro	NEW_rogowski.dat, Currents0.dat, Axials0.dat, Currents2.dat, Axials2.dat
6.22	RadialCase2a.ps	frc_plots.pro	Radials2.dat
6.23	casesamp1a.ps	TOF_DATA.pro	scan21.dat, scan17.dat

Table B.4: Figures and associated filenames and IDL programs (continued)

Figure	Figure Filename	IDL Program	Data Used
7.1	DensCntUNBD.eps	plots.pro	Pressure_Balance_Current.dat
7.2	DensityContour2.eps	plots.pro	Pressure_Balance_Current.dat
7.3	bradfit_new_er.ps	BequilFit.pro	FRCequilibrium_1.1.dat, newbz.dat
7.4	AllDensities.ps	plots.pro	Pressure_Balance_Current.dat, FRCequilibrium_1.1.dat, isat_data.dat
7.5	deltaZ.ps	plots.pro	separatrix_deltaz.dat
7.6	AllCurrents.ps	plots.pro	Pressure_Balance_Current.dat, IonCurrent_Artan_Equil.dat, NEW_rogowski.dat
7.7	edeltar.eps	DriftAnalysis.pro	Ar_Currents_Case1.dat, FRCequilibrium_1.1.dat, ArTempDrifts.dat, LineRatioTemp.dat
7.8	eidrifts.eps	DriftAnalysis.pro	Ar_Currents_Case1.dat, FRCequilibrium_1.2.dat, ArTempDrifts2.dat, LineRatioTemp.dat, ArVdriftErr.dat, Pressure_Balance_Current.dat
7.9	eidrifts2.eps	DriftAnalysis.pro	Ar_Currents_Case1.dat, FRCequilibrium_1.2.dat, ArTempDrifts2.dat, LineRatioTemp.dat, ArVdriftErr.dat, Pressure_Balance_Current.dat
7.10	omegae.ps	plots.pro	Case1_with_drifts_2.dat, Pressure_Balance_Current.dat, IonCurrent_Artan_Equil.dat, NEW_rogowski.dat

Table B.5: Figures and associated filenames and IDL programs (continued)

C Schematics

This appendix contains miscellaneous schematics that are not already included in the thesis.

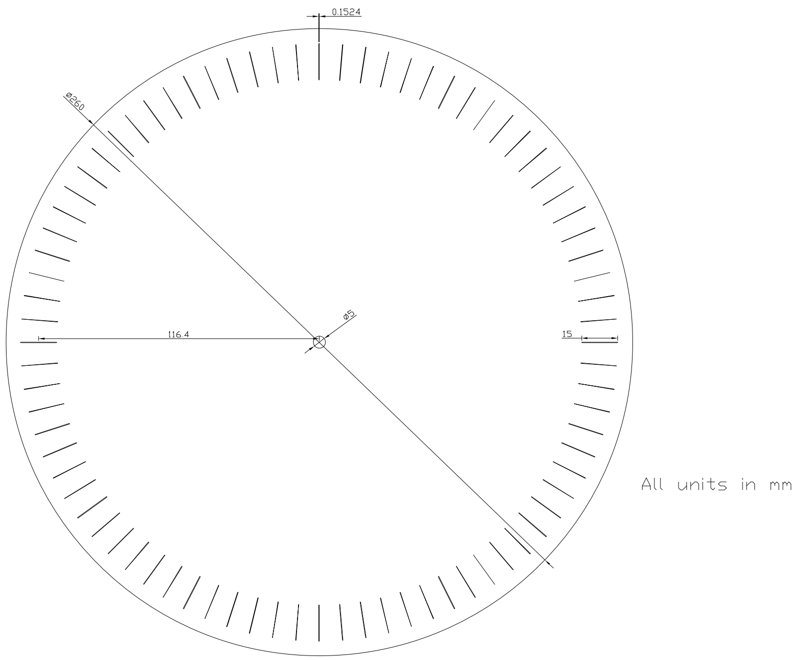

Figure C.1: Chopper wheel

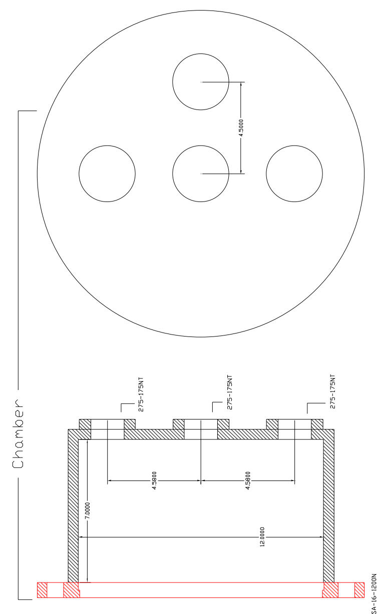

Figure C.2: Vacuum vessel for the charge-exchange neutral particle analyzer.

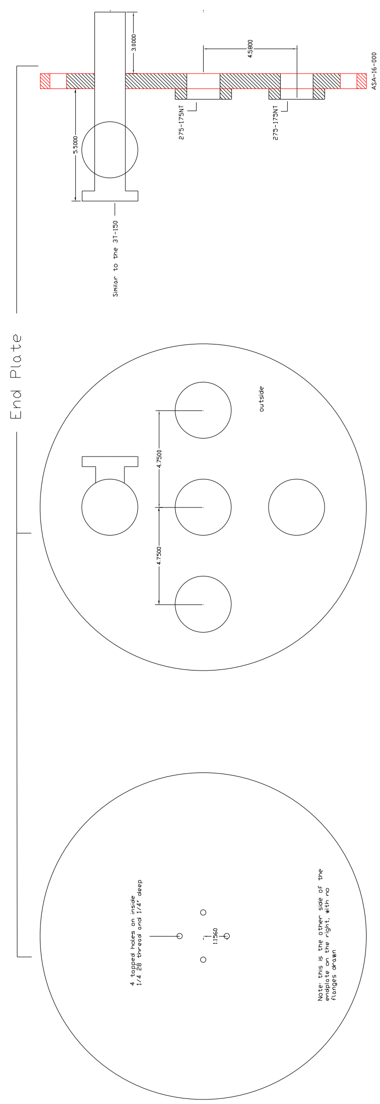

Figure C.3: Flange for the charge-exchange neutral particle analyzer.

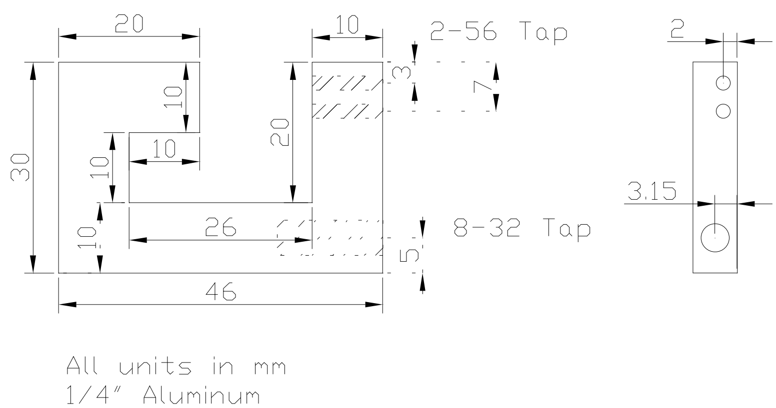

Figure C.4: Custom cylindrical lens holder for spectrometer